Millimeter-Scale Encapsulation of Wireless Resonators for Environmental and Biomedical Sensing Applications

by

Jiqing Jiang

A dissertation submitted in partial fulfillment
of the requirements for the degree of
Doctor of Philosophy
(Electrical and Computer Engineering)
in the University of Michigan
2018

Doctoral Committee:
  Professor Yogesh B. Gianchandani, Co-Chair
  Dr. Scott R. Green, Co-Chair
  Dr. Grace Elta, M.D.
  Professor Duxin Sun
  Professor Kensall D. Wise

Jiqing Jiang

jqjiang@umich.edu

ORCID ID: 0000-0002-8162-4557

ACKNOWLEDGEMENTS

The research described by this dissertation was funded in part by the National Institutes of Health (NIH, R01DK102663) and by the University of Michigan (UM). The content is solely the responsibility of the author and does not represent the official views of the National Institutes of Health. Some fabrication processes were completed at the Lurie Nanofabrication Facility (LNF) operated by the Solid-State Electronics Laboratory (SSEL) at the University of Michigan. Funding was provided in part by the University of Michigan.

I want to express my deepest gratefulness to my advisor Prof. Yogesh Gianchandani for giving me the opportunity to study under his direction and work with talented people in his group. His enthusiasm, extensive experience, and advanced vision on research have kept guiding me through my PhD research. I am especially grateful to Dr. Scott Green. His deep understanding in the area of magnetoelastic resonators and great patience in helping me solve problems established a solid academic foundation and provided valuable experience on research methodology for me. I would also like to thank my other committee members, Prof. Kensall Wise, Prof. Duxin Sun, and Prof. Grace Elta for their guidance and suggestions on improving this work. Dr. Richard Kwon collaborated on the animal experiments and also gave me his professional opinions to help me have a better understanding of the problem and I truly appreciate his contributions.

I would like to thank the staff members at the University of Michigan Medical School, including Amber Yanovich, Gail Rising, Dr. Bob Sigler, Luaren Krueger, Jiajie Xu, Rafael Ramirez, Dr. Patrick Lester, Scot Pittman, and all the ULAM husbandry and veterinary technician staff, who assisted us in the surgical operations, animal care, and necropsy.

I would like to thank my group members and friends in the 2001 office, including Tao, Xin, Yutao, Venkatram, Yushu, Yu, Shiyang, Andy, Alex, Qisen, Ryan, Neeharika, Ramprasad, Jonathan, Chandler, Weilin, Daniel, Tsenguun, Leo, Partha, Sungmee, Eric, Tal, Stacey, Amin, Ali, Yi, Christopher, Farzad, Sajal, Donguk, and Behnoush.

Finally, I would like to thank my parents for their unconditional support and love to me.

TABLE OF CONTENTS

LIST OF FIGURES

Figure

LIST OF TABLES

Table

LIST OF APPENDICES

Appendix

LIST OF SYMBOLS

ε	strain tensor
σ	stress tensor
H	magnetic field intensity
B	magnetic flux density
d	magnetostrictivity
s^H	elastic compliances at constant magnetic field intensity
μ^σ	magnetic permeabilities at constant stress
ΔP	pressure loss
D	uniform diameter of a cylindrical tube
L	length of a cylindrical tube
μ_f	fluid dynamic viscosity
Q_r	volumetric flow rate
R_f	flow resistance
k_{F_total}	total bending stiffness
$k_{11.5}$	bending stiffness of an 11.5 Fr stent
k_F	bending stiffness of the Type F package

k	bending stiffness
E	Young’s modulus
I	second moment of area
r_o	outer radius
r_i	inner radius
b	beam width
h	beam thickness
k_{10}	bending stiffness of a 10 Fr stent
k_S	bending stiffness of the Type S package
f	resonant frequency (Hz)
L_s	length of the ribbon
ρ_s	density of the sensor
α_m	equivalent mass loading
ω_r	resonant frequency (rad/s)
Q	quality factor
I_{in}	input current
ω	frequency (rad/s)
E_s	signal energy
Δt	time delay

${A_n}^2$	noise level
τ	time constant
A	signal amplitude
A_n	noise amplitude
ω_0	fundamental frequency of longitudinal vibrations for a free-free beam
L_0	beam length
M	load mass
S	cross-sectional area
P	force

ABSTRACT

Wireless magnetoelastic resonators are useful for remote mapping and sensing in environments that are harsh or otherwise difficult to access. Compared to other wireless resonators, magnetoelastic devices are attractive because of their inherently wireless nature, and their ability to operate passively without a power source, integrated circuitry, or antenna.

An open challenge for using miniaturized magnetoelastic resonators is application-tailored encapsulation and packaging. General packaging considerations for magnetoelastic resonators include not only the mechanical design but also electromagnetic transparency, adaptability of form factor with appropriate feature size, and chemical inertness and/or biocompatibility.

In this thesis, the packaging of magnetoelastic resonators is investigated in two contexts: environmental sensing and biomedical sensing. The first context is for tagging and mapping applications in a high temperature ($\geq 150°C$), high pressure (≥ 10 MPa), corrosive environment, such as a hydraulic fracture branching from a wellbore. This work utilizes for the first time a micro molding process to thermoform liquid crystal polymer (LCP) packages for protecting magnetoelastic resonators. The package is < 10 mm^3 and includes micron-scale features to support the resonator and allow it to vibrate with low loss. It has an average shear strength of 60 N, and can endure pressure up to 2000 psi ($\approx$13.8 MPa).

The second context is for implantable magnetoelastic resonators, which are used for sensing biological parameters. These packages must: protect the sensors during deployment through an endoscope, be biocompatible and chemically inert, be able to pass through a complex delivery path, and fit within a limited size. Protecting the resonator during delivery while still allowing interaction with biological fluids is achieved with polymeric packages incorporating features such as a perforated housing and tapered and smoothed edges. This approach also includes features to aid in assembling with plastic stents via polyethylene tethers. The packaged resonator must pass through a complex delivery path without damage due to bending, so the compromise between two architectures – one mechanically flexible (Type F) and one mechanically stiff (Type S) – is evaluated. The primary advantage of the Type F package is the flexibility of the package during the delivery process while that of the Type S package is to maintain a strong signal even when the stent is in a curved bile duct. The length, width, and maximum thickness of the Type F package are 26.40 mm, 2.30 mm and 0.53 mm, respectively. The Type S package has an outer diameter of 2.54 mm, a length of 15 mm, and a maximum thickness of 0.74 mm. The two package types are tested in benchtop flexibility tests, and *in vivo* and *in situ* in porcine specimens. The animal tests demonstrate partial functionality of both types of packages, while also indicating that smaller and more elastic package designs are needed.

Remaining in the implantable sensor context, an improved and miniaturized resonator design is explored. Miniaturizing the resonator accordingly allows miniaturization of the packaging, reducing the impact on the overall functionality of the medical device. The fabricated sensor is

8.25 mm long, 1 mm wide with the largest thickness of 218 μm. The resonant frequency of the resonator is around 173 kHz which is similar to that of a 12.5 mm long ribbon sensor. This resonator design is self-biased, simplifying the packaging and assembly compared to previous designs.

CHAPTER

Chapter 1: Introduction

Wireless microsystems have been an area of extensive research over the past few decades, owing to their potential for use in distributed networks (e.g. the “Internet of Things”), as the information gathering part of informatics, and as the enabler of next generation medical implant technologies. One critical portion of wireless microsystems is the wireless micro sensor, which takes the role of acquiring the information and data from the physical environment. As the extension of human perception, wireless micro sensors are often deployed in the environments that are small, harsh, and difficult to access. One type of wireless micro sensor takes the form of a resonator, with the measurand of interest affecting the frequency response of the resonator. The resonant characteristics of this type of device can often be leveraged for better signal strength, sensitivity, and/or noise rejection.

One subset of wireless micro resonators, and the main subject of this work, is the magnetoelastic resonator. Inherent material properties allow magnetoelastic resonators to passively transfer the environmental information through the coupling of mechanical vibration to magnetism. This can result in a wireless transducer with an extremely small form factor, and thus the resonators are attractively applied for tagging or sensing in environments that are difficult to access. However, in order to utilize the magnetoelastic resonators in a practical application, proper encapsulation is particularly important. Therefore, this work focuses on the packaging techniques for magnetoelastic resonators and evaluating packaging approaches for two different applications: first, tags for harsh environments and second, biomedical viscosity and mass sensing; additionally, the general mechanism of magnetostriction and the working principle of the magnetoelastic resonators are included and further considered as related to miniaturization and integrated devices, both of which will enable improvements to packaging.

1.1. Motivation and Previous Efforts in Wireless Micro Resonators

Wireless microsystems connect objects remotely through sensors and controllers, allowing the devices in the network to be used to quantify the surrounding physical world. A typical wireless microsystem uses a miniaturized RF antenna (or inductive link) for far field (or near field) communication and/or power transfer. Any sensing or actuating modality of the system is typically derived from an additional component. One example of a wireless microsystem is radio frequency identification (RFID) tags, which uses an antenna typically along with circuitry for use in vehicle access control and item tracking [Wei05, Mon88]. Another example are wireless pressure sensors, which take one of two forms: passive devices, which utilize an inductor connected to a capacitive pressure sensor to enable wireless interrogation [Tak03, Tak06, Joy07, Yu14, Hua16], and active devices, which utilize an RF antenna for power transfer to a charge storage device (battery/capacitor), which drives integrated circuitry for onboard processing, memory, and re-transmission [Gha13, Shi16].

Wireless micro resonators are a subset of wireless microsystems, and refer to mechanical rather than electromagnetic oscillations mentioned above. A key advantage of wireless resonators compared to general wireless systems is the mechanical resonant behavior, which allows mechanical coupling to the environment and thus the potential for direct measurement of the mechanical parameters of the environment. Additionally, the mechanical resonance of the device is typically at a much lower frequency (10 kHz – 10 MHz) than purely electromagnetic resonant frequencies (typically 112 MHz [Shi16]) for comparably sized antennas, which can result in less signal attenuation through conductive media. Due to these advantages, wireless micro resonators have broad potential applications in sensing systems, e.g., locating positions, detecting inventories, and profiling blockage or leakage.

Wireless micro resonators are capable of sensing parameters remotely in a small, sealed, or harsh environment where the sensors are difficult to access. These parameters include temperature, pressure, humidity, liquid viscosity, fluid flow rate, strain, and chemical/biological agents.

Wireless surface acoustic wave (SAW) devices are one type of wireless micro resonator [Bao87, Chi10]. These devices receive the transmitted signal via a connected antenna and convert it into a surface acoustic wave with a piezoelectric transducer. The acoustic wave propagates along the surface and is echoed by reflectors to transmit back to the antenna. The change in the amplitude, phase shift, frequency shift or time delay can be monitored to sense the measurand of interest.

Magnetoelastic devices are another type of passive wireless resonator, and the focus of this work. A magnetoelastic device uses material that couples a magnetic field to mechanical strain in order to launch resonant vibrations. These devices are very attractive for applications of remote position detection and sensing parameters in difficult-to-access environments. One critical advantage magnetoelastic devices have compared to other wireless resonators (such as SAW devices) is that they have no need for integrated circuit components or antennas, as the devices are inherently passive wireless resonators. While this critical advantage has been leveraged in previous miniaturized magnetoelastic devices [Gre07, Gre13, Tang14a, Pep14, Pep15], an open challenge for utilization of the miniaturized magnetoelastic resonators is appropriate packaging for the application. General considerations for packaging of magnetoelastic resonators include sufficient electromagnetic transparency of the package material, and the ability to incorporate features for providing mechanical protection to the resonator while also allowing mechanical coupling to the environment where appropriate. In this introductory chapter of this report, the physical phenomenon of magnetoelasticity is first described. Then, two applications for encapsulation and packaging of magnetoelastic resonators are briefly presented.

1.2. Magnetoelastic Resonators

Magnetoelasticity describes the coupling between stress, strain, and magnetism [Eng00]. When exposed to a time-varying magnetic field, the magnetic domains in a magnetoelastic material tend to rotate and align with the changing field, affecting the strain of the material and causing mechanical vibrations in a macroscopic view. As a response, the vibrations in the material generate another oscillating magnetic flux, which can be detected by wireless methods [Gri02, Gri11, Tan13, Qu15]. Changes in the mass loading and the density/viscosity of the medium surrounding a magnetoelastic sensor change the damping effect on the sensor that can be measured by as a shift resonant frequency and smaller quality factor.

Fig. 1.1 describes a typical magnetoelastic wireless sensing system [Gri11]. The sensor is actuated by an external time-varying magnetic field which is provided by the excitation coil. The mechanical vibration of the sensor in turn generates another oscillating magnetic field. Therefore, the frequency response of the sensor can be detected magnetically (by the sensing coil), optically (by the laser emitter and phototransistor), and acoustically (by the microphone).

Although the magnetoelastic phenomenon is non-linear, the behavior of a magnetoelastic material can be represented by the following small signal response [IEE91, Pep15]:

$$[\varepsilon] = [s^H][\sigma] + [d][H] \tag{1.2.1}$$

$$[B] = [d]^T[\sigma] + [\mu^\sigma][H] \tag{1.2.2}$$

where $[\varepsilon]$ is the strain tensor, $[\sigma]$ is the stress tensor, $[H]$ is the magnetic field intensity, $[B]$ is the magnetic flux density, $[d]$ is the magnetostrictivity matrix, $[s^H]$ is the elastic compliances at constant magnetic field intensity, and $[\mu^\sigma]$ is the magnetic permeabilities at constant stress. The operating point of the sensor is set by the direction and magnitude of a bias magnetic field. This biasing field is targeted at maximizing the magnetostrictivity d, and thus maximizing the signal amplitude. Additionally, because of the coupling between the magnetism and strain, the bias magnetic field also affects the Young's modulus of the material, a phenomenon which is referred to as the ΔE effect. Our previous test results [Gre09a, Gre09b] showed that changing the DC bias field or orientation could have a large effect on the resonant frequency (a doubled bias field could shift the resonant frequency by 3%).

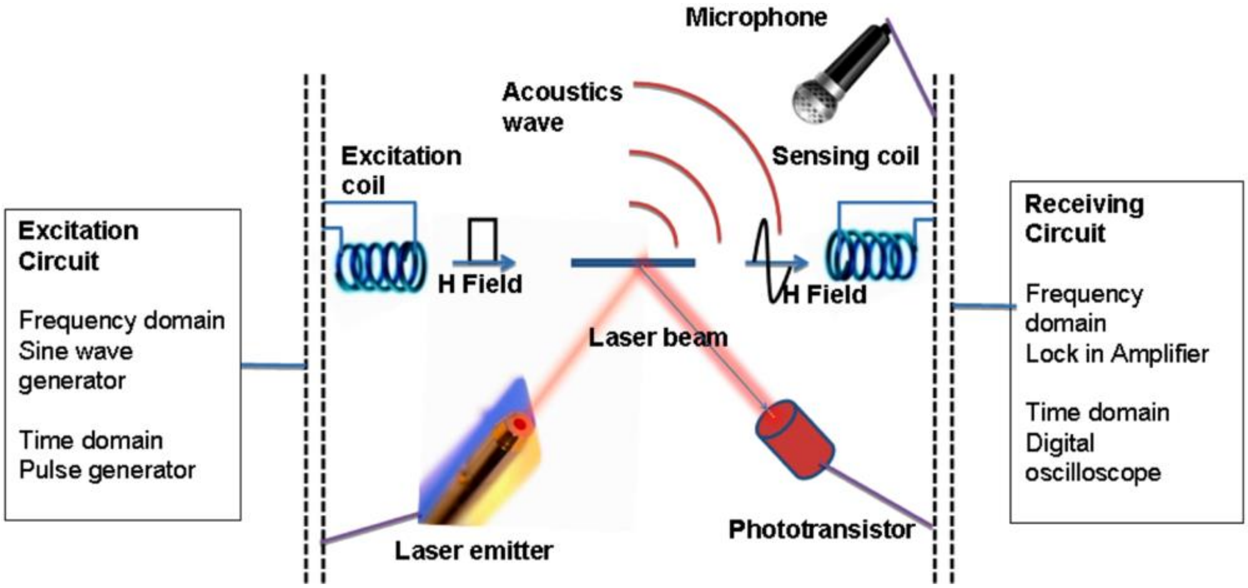

Fig. 1.1: A typical magnetoelastic wireless sensing system. The sensor strip in the center of the figure is actuated by a magnetic field which is provided by the excitation coil. Its resonant frequency changes due to Young's modulus, mass loading, and other environmental changes, which can be picked up magnetically (by the sensing coil), optically (by the laser emitter and phototransistor), and acoustically (by the microphone) [Gri11].

1.3. Encapsulation of Magnetoelastic Resonators

1.3.1. Encapsulation for Tagging Applications in Harsh Environments

One potential tagging application in the harsh environment is the fracture illumination system proposed for detecting hydraulic fractures which are initiated by pumping a fracturing fluid after drilling a wellbore [Gia15, Tan14a]. This application involves dispersing the magnetoelastic resonators – along with the fracturing fluid – into the fractures, and subsequently using an antenna array – with beam forming capabilities – to triangulate the fracture locations as indicated by strong magnetoelastic response from a cluster of resonators within the fractures.

In this and other tagging applications, it is generally desirable to protect the resonator from the surrounding environment, including viscous and corrosive liquids. For certain applications in the energy industry, the packaging must provide this protection while also enduring high temperatures (≥ 150°C) and pressures (≥ 100 atm). Additionally, providing proper support to the miniaturized resonators requires the inclusion of features with dimensions as small as a few tens of microns. Finally, the package should be electromagnetically transparent to avoid reducing the signal transfer to and from the resonator.

This last requirement rules out the use of metals, leaving ceramics and some high temperature polymers as candidates. Though ceramics like low-temperature co-fired ceramic (LTCC) have some desirable qualities including extremely high temperature resistance, mechanical strength, and chemical inertness, they are relatively expensive, brittle, and difficult to micro-machine [Zou02, Tho14]. Polymers sacrifice some strength and temperature resistance but offer greater ductility and machinability. This work demonstrates the thermoforming of a package from a polymeric material that offers high temperature resistance, chemical inertness, and suitable strength for a tagging application.

1.3.2. Packaging for Biliary Stent Monitoring Sensors

Biliary stents are tubular implanted devices meant to maintain a constricted bile duct. While stents relieve patients from suffering the constriction of the bile duct, which occurs due to benign or malignant biliary diseases, they are not a perfect long-term solution [Lib96, Don07]. The stents need to be removed and replaced frequently because the accumulation of luminal contents block the stent after an unpredictable period of time. Not only is the occlusion rate unpredictable, it is also difficult to monitor with current techniques [Jud07, Tse06]. Current practices for monitoring stent blockage are either indirect, invasive, or expensive. One of the most common tests of biliary or stent blockage is to examine the bilirubin level, alkaline phosphatase level, and liver enzymes from a blood test result. However, these indicators may not be apparent before a severe obstruction, leading to a delayed diagnosis. Alternatively, transabdominal ultrasonography evaluates the upstream dilation of the duct as indirect evidence of the obstruction. However, observation of normal ducts cannot completely exclude the possibility and, in some cases, the dilation of the ducts is a response to other factors. Another frequently used method, endoscopic retrograde cholangiopancreatography, involves both an endoscope and fluoroscopic X-ray to generate diagnostic images of the biliary ducts. The drawbacks of the method include the invasiveness of the endoscope, the high risk of complications, the equipment cost, and the usage of conscious sedation; therefore, it is mainly used for therapeutic purposes.

The specific stent design used has been shown to have some effect on the duration of patency, but eventual occlusion has been an unavoidable outcome. Plastic biliary stents, compared to self-expandable metal stents, are cheaper and easier to manipulate but they also tend to be occluded more readily by biofilm, biliary sludge, and debris. This higher occlusion rate is due to the limited inner diameter, stent design, and the interaction of the stent material with biological components [Kwo16, Rai03]. Larger diameter plastic biliary stents are normally considered to have longer patency but the maximum size is limited by the inner diameter of the endoscope. Additionally, according to several comparative studies, no extended patency duration is observed when the stent size is larger than 10 Fr [Kad92, Wag13]. Side holes are standard features of commercially available biliary stents, which are designed for maintaining biliary flow if the ends of the stents are blocked. Elimination of the side holes in the stent design is believed to delay the obstruction, because biofilm formations were initially seen around the side holes of the stents retrieved from patients and some *in vitro* experiments showed the stents without side holes had less sludge formation than those with side holes. However, studies on patients found that the stents without side holes did not have a significant advantage regarding stent patency. Using low friction materials, hydrophilic coatings, or antimicrobial agents for the stents also has not improved the duration of stent patency [Fai00, Don07].

Previous work has reported an integrated system for non-invasive, wireless measurement of sludge accumulation in a plastic biliary stent [Gre13]. The system is comprised of four main components: a network analyzer, a power amplifier, transmit coils and receive coils. The interrogative signal generated from the network analyzer is amplified by the power amplifier and emanated by the transmit coils as a form of electromagnetic wave. The magnetic signal generated by the magnetoelastic sensor is sensed by the receive coils and fed back to the network analyzer. The transmit coils and receive coils are configured to minimize the coupling between each other but both of them can couple to the sensor. The measuring range of the system is 7.5 cm.

While this system has shown some promising *in vitro* and *in situ* results, it failed when subjected to the requirements of the endoscopic delivery. Specifically, because the sensors were completely exposed in the stent, it was highly possible for them to be snagged and damaged by inserting the introducer through the stent, which is a requirement during the implantation. Another shortcoming of the system as previously reported is the lack of a stent-integrated DC biasing field [Gre09a, Gre09b]. An integrated DC biasing field will provide a near-constant biasing field to the resonator, thus minimizing changes in the operating point of the sensor due to the ΔE effect and preventing misdiagnosis due to the falsely shifted resonant frequency.

For this application, the package material should be biocompatible and be chemically inert at body temperature. Additionally, due to the limited size of the biliary stent, the package material and fabrication process must facilitate features with high resolution. Finally, the package material should be electromagnetically transparent to prevent blocking the signal transfer either to or from the resonator, as mentioned before. Of critical importance, the package – once assembled to the stent – must be capable of passing through the endoscope during delivery without impeding the capability of the endoscopic surgeon to place the stent as desired. This work presents two types of packages, fabricated by using 3D printing technology. The mechanically flexible (Type F) package is flexible during the delivery process while the mechanically stiff (Type S) package maintains a strong signal even when the stent is in a curved bile duct.

1.4. Organization of this Dissertation

The goal of this thesis is to evaluate encapsulation approaches for a type of wireless micro resonator – magnetoelastic resonators. The encapsulation is used to protect the resonator while also allowing the resonator to sense its environment as necessary. The designs of the package for the magnetoelastic resonators need to be customized for different applications and also require considering the electromagnetic and mechanical material properties, sensor functionality, form factor, and other constraints. Therefore, this thesis includes the general design criteria for sensing physical parameters using magnetoelastic resonators, and describes the methodologies for designing and fabricating packages and resonators for two practical applications.

The remainder of this dissertation is organized as follows. First, the encapsulation of the magnetoelastic resonators for tagging applications in the harsh environment is described in Chapter 2. A second example of encapsulation of magnetoelastic resonators, with application in sensing of parameters in an implanted medical device, is shown in Chapter 3. Chapter 4 describes animal tests using devices protected by the encapsulation approaches of Chapter 3. A miniaturized resonator design, which can aid in reducing package size, is presented in Chapter 5. Finally, the contributions and potential future efforts are summarized in Chapter 6.

The second chapter evaluates thermoformed liquid crystal polymer (LCP) packages (with an outer diameter 2.45 mm) for miniaturized magnetoelastic resonators that are intended for tagging applications. The packages are composed of thermoformed hemispherical LCP shells, utilizing a newly-applied micro molding process. The packages include micron-sized features to properly support and suspend the resonators within, allowing the resonators to vibrate with no measurable loss due to the packaging.

The third chapter illustrates another packaging technique which is used in an implantable medical device. Two types of 3D printed packages integrate the magnetoelastic sensor and magnetic biasing material into commercial plastic biliary stents (11.5 Fr and 10 Fr) for wirelessly monitoring biliary sludge accumulation. The basic approach behind the design of these packages is to include a surface that will shield the resonator from being damaged by the standard introducer tool, maintain a smooth and tapered profile to facilitate passage of the introducer, and include small perforations in that surface to allow the biological materials to interact with the sensor. Tradeoffs in the flexibility of the encapsulation approach are examined.

The fourth chapter presents the animal test results for the packaged devices described in Chapter 3. The signal interrogation session was scheduled once a week. The position of the stent was confirmed by X-ray in each interrogation session. No signal was measured from the implanted sensors. The cause of the failure to obtain a signal from the sensor was examined and identified.

The fifth chapter describes an improved resonator design, specifically targeting miniaturization while maintaining a low resonant frequency. The scaling effects for simple ribbon resonators are examined with finite element analysis and experimentally and show that length reduction has substantial impact on the received signal. Therefore, a new concept for miniaturizing the sensor while maintaining the resonant frequency is presented, followed by analytical and numerical design of the new concept. The fabrication and experimental performance of the new concept is then demonstrated. The miniaturization of the resonator can further allow a package of decreased size, thus providing an opportunity to reduce the impact on the overall functionality of the medical device.

The last chapter presents the summary of the specific outcomes of this work. General contributions to the field of knowledge are also described. Future work is proposed that would improve the packaging and devices for the applications described theretofore.

Chapter 2: Thermoformed Liquid Crystal Polymer Package for Magnetoelastic Frame-Suspended Hexagonal Resonators

2.1. Introduction

This chapter describes the design, fabrication, and experimental characterization of liquid crystal polymer (LCP) packages for miniaturized magnetoelastic resonators. The package offers high temperature resistance, chemical inertness, and suitable strength. While LCP has been studied previously for packaging purposes [Wan01, Wan03, Tho14], the ability to package magnetoelastic resonators for tagging applications is shown here for the first time.

2.2. Package Design

2.2.1. Material Selection

Liquid crystal polymer (LCP) and other polymers with similar thermal and mechanical properties are candidates for the package. Polyether ether ketone (PEEK) is mechanically strong, chemically resistant, and is thermally stable. However, a durable bonding technology is an open challenge for long term applications of this material [Awa10a, Awa10b, Com96, Hal12]. Polybenzimidazole (PBI) is another commercially available polymer that has exceptional thermal and chemical stability, but it is difficult to process due to high processing temperature (425°C) [Iqb14]. Similar to PBI, polyimide (PI) has good thermal and chemical resistance but it is relatively affected by moisture and humidity and vulnerable to strong acids and bases [Wan03, Dok99].

The favorable electromagnetic transmission characteristics, excellent mechanical stabilities, and barrier properties for harsh environmental conditions make LCP well-suited for the application, especially compared to other polymers. The thermoplastic material LCP, based on its unique physical character that the linked rigid monomers in the material can align along and maintain the direction of shear flow in liquid crystal state and after cooling, is receiving growing attention in the packaging of electronics components [Wan03]. The high frequency characteristics of LCP have been widely studied and validated for use of the material in RF packaging due to a very low dielectric constant of 3.0 and loss tangent of 0.002 at high frequencies [Wan01, Tho14]. In addition, it provides high Young's modulus (1.8 GPa to 40 GPa), good dimensional stability (~0.1%), and low moisture absorption (~0.02%) [Zou02, Wan01, Wan03, Tho14, Dok99, Jay98, Ten04]. LCP can be reinforced with glass fibers to increase heat resistance and mechanical strength while reducing the degree of anisotropy [Vec01, Vec11]. In this work, the LCP resin used is VECTRA® E150i (50% glass reinforced), in the form of a black pellet (cylindrical, with ~3 mm diameter and ~5 mm length).

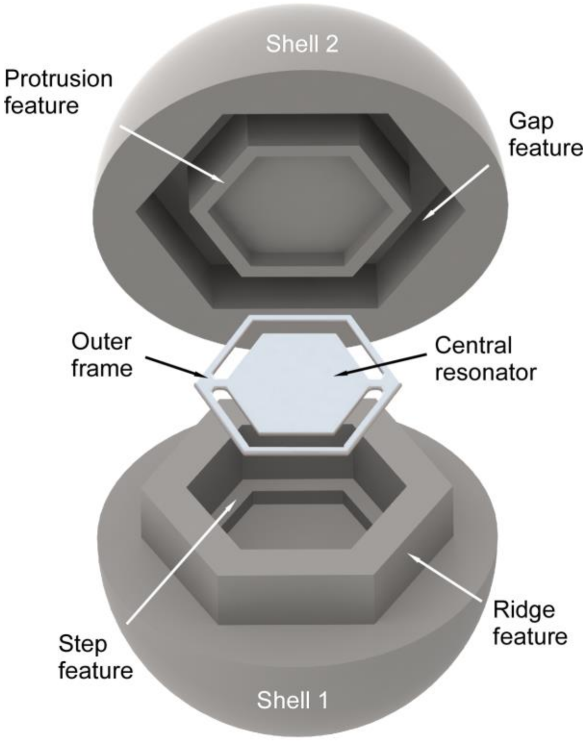

Fig. 2.1: LCP package configuration for magnetoelastic frame-suspended hexagonal resonators.

2.2.2. Package Concept and Structure

The package structure is comprised of two hemispherical LCP shells (Shell 1 and Shell 2) with internal features that support a magnetoelastic frame-suspended hexagonal resonator with the size of ø1.31 mm x 27 μm, as shown in Fig. 2.1. The resonator inside is the previously reported miniaturized high-performance magnetoelastic frame-suspended hexagonal resonator [Tan14a]. About 1000 resonators are batch fabricated with photochemical machining (PCM) from Metglas^{TM} 2826MB. The size of the resonators is ≈ 100x smaller than commercially available tags. The integrated frame-suspension reduces interaction between the resonator and the substrate, allowing a stronger signal response. The fabrication efficiency is increased by the hexagonal shape. The experimental results show a 0.44% standard deviation in resonant frequency and a linear signal superposition with clusters of up to 500 resonators.

Fig. 2.2 (a) and (b) illustrate the 3D structures of the bottom shell (Shell 1) and the top shell (Shell 2) as well as their cross-sectional views labeled with detailed dimensions. Both shells are used in conjunction to package the frame-suspended hexagonal resonator shown in Fig. 2.2 (c). The package has an outer diameter of 2.45 mm. Shell 1 has a 0.40 mm ridge feature in height and a 0.11 mm step feature in depth. The widths of these features are 0.24 mm and 0.11 mm, respectively. Correspondingly, Shell 2 has a 0.36 mm gap feature in depth and a 0.06 mm protrusion feature in height. The widths of these features are 0.31 mm and 0.14 mm, respectively. The step features in Shell 1 and the protrusion features in Shell 2 support the outer frame of the resonator and suspend the central resonator, allowing it to freely resonate at the desired frequency around 2.12 MHz. Once the two shells are assembled together, the step features will have a nominal separation of 80 μm to prevent clamping the frame of the resonator. The widths of the step and protrusion features are designed to maintain a margin of at least 20 μm around the resonator, which is large enough to accommodate variation in resonator and package dimensions, but small enough to ensure that the resonator cannot become misoriented and that the active portion of the resonator does not contact the package features. The gap and ridge features are sized to mate with each other for assembly, and the resulting mechanical interlocking is intended to provide a larger shear strength.

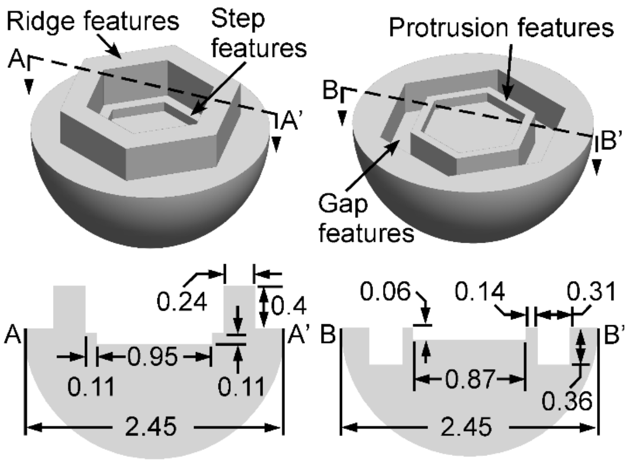

(a) Shell 1

(b) Shell 2

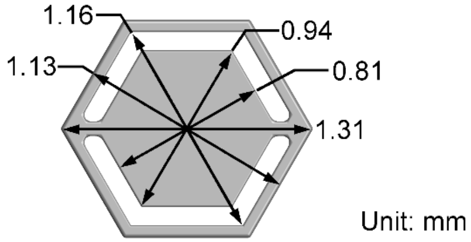

(c) Resonator

Fig. 2.2: (a) 3D structure of the bottom shell (Shell 1) and its sectional view. (b) 3D structure of the top shell (Shell 2) and its sectional view. (c) Top view of the frame-suspended hexagonal resonator.

2.2.3. Metal Molds and Auxiliary Tools Concept and Structure

The LCP shells are thermoformed with corresponding metal molds. The two shells are bonded together with epoxy and the outer flash is cut away by a flash removal tool. Stainless steel (type 304) is selected as the metal for molding the LCP shells due to the advantages of low cost, excellent toughness, and resistance to oxidation and corrosion. Metal molds with three different geometries are needed for molding the two LCP shells. Mold 1 has a hemispherical cavity with a diameter of 2.45 mm and four channels and reservoirs to accommodate excess LCP material, as shown in Fig. 2.3 (a). The hemispherical cavity is used to mold the external features of both Shell 1 and Shell 2. Each reservoir has the dimension of 1 mm x 0.3 mm x 0.3 mm and is able to handle up to ~0.09 mm3 excess material. Mold 2 and Mold 3, as shown in Fig. 2.3 (b) and (c), are used to mold the internal features of Shell 1 and Shell 2, respectively. The structures of both molds are counterparts of Shell 1 and Shell 2 and have the same sizes. The flash removal tool is a 1 mm long hollow cylinder tip with an inner diameter of 2.45 mm and a wall thickness at the cutting edge of 0.23 mm. To align Mold 1 and Mold 2 or Mold 3 during thermoforming of the shells, an alignment fixture is used. This fixture is a single piece of 304 stainless steel with a square through hole sized to closely fit to the outer surfaces of the molds.

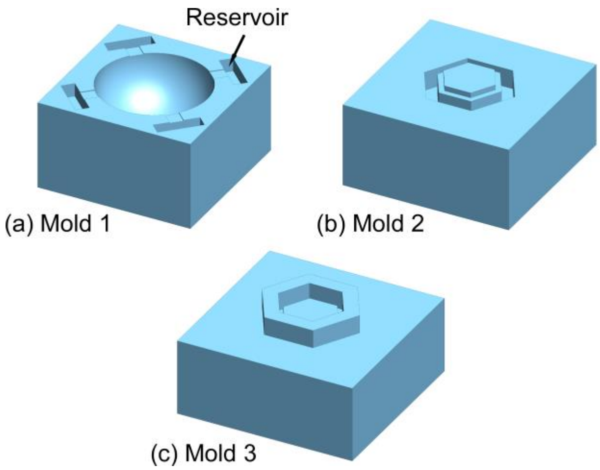

(a) Mold 1

(b) Mold 2

(c) Mold 3

Fig. 2.3: (a) Mold 1 has a hemispherical cavity which is used to mold the backside features of Shell 1 and Shell 2. The reservoirs are used to displace excess LCP materials to form flash. (b) Features of Mold 2 are the counterparts of that in Shell 1. Mold 2 is used along with Mold 1 to form Shell 1. (c) Features of Mold 3 are the counterparts of that in Shell 2. Mold 3 is used along with Mold 1 to form Shell 2.

2.3. Package Fabrication

The package is fabricated using four processes: thermoforming, metallization, bonding, and deflashing. The LCP shells are first thermoformed at 340°C with the stainless steel molds. Then, the inner surfaces of the shells are metallized to promote adhesion. After metallization the shells are bonded together and the outer flash is removed by the flash removal tool. The process flow is shown in Fig. 2.5, and described in detail in the following subsections.

2.3.1. Fabrication of Molds and Tools

Micro electro-discharge machining (μEDM) (SmalTec EM203) is used for patterning the three molds and the flash removal tool [Tak02, Ric10]. μEDM has a high machining precision and is applicable to any conductor. For this work, serial mode μEDM is utilized, with a tungsten electrode wire (300 μm or 125 μm diameter, as necessary) used as the cutting tool to discharge sparks to the workpiece (stainless steel sample), eroding the sample surface while both electrode and sample are immersed in a dielectric fluid (oil). The minimum feature size of the μEDM technique is approximately 5 μm [Asa07]. Fig. 2.4 (a) to (c) illustrate the three finalized μEDMed molds. A rib is added at the bottom of the cavity of Mold 1 in order to provide an external visual alignment feature on the shells to denote the direction of the embedded resonator to assist in the electromagnetic testing described later.

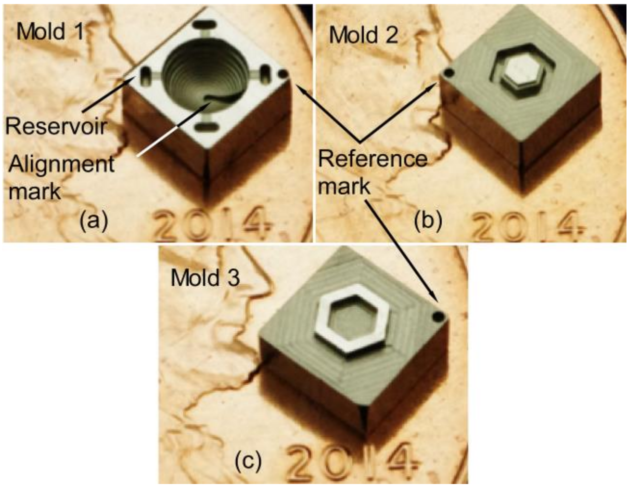

Fig. 2.4: Inside features of µEDMed stainless steel molds (a) Mold 1, (b) Mold 2, and (c) Mold 3.

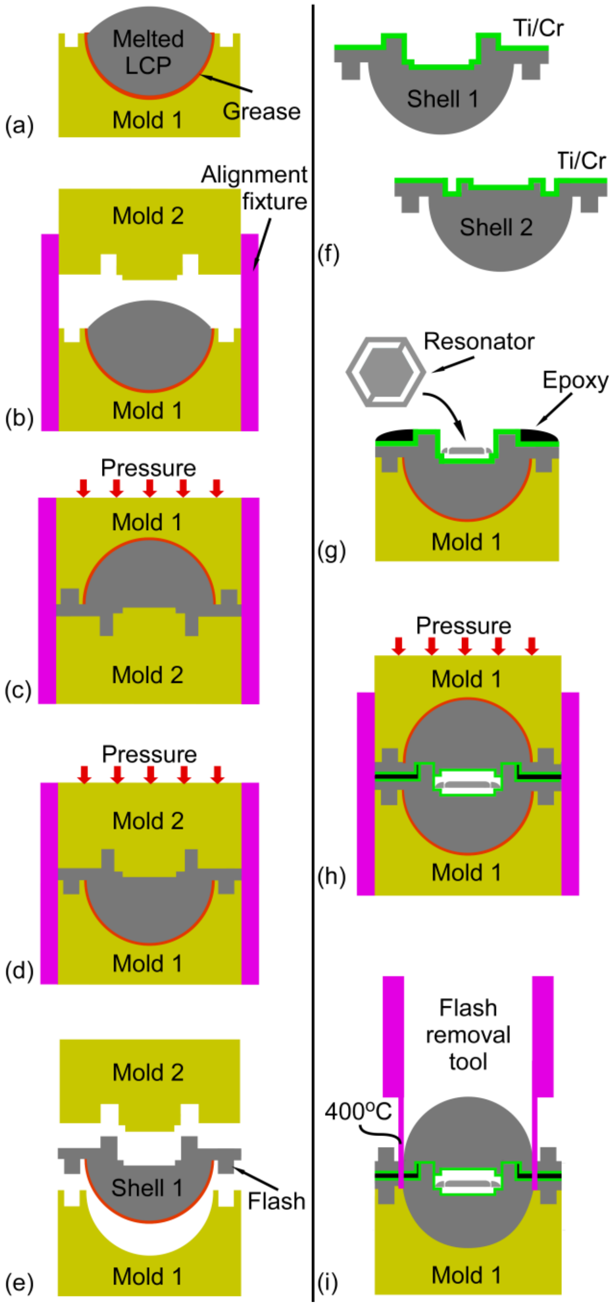

Fig. 2.5: Process flow: (a) Thermoforming of LCP at 340°C in Mold 1, with grease as a release agent. (b) Alignment of Mold 2 with Mold 1 to form Shell 1. (c), (d) Application of pressure and heat to each side of the mold assembly to allow LCP to flow into mold features. (e) Demolding of Shell 1 after molds are cool. The process flow for Shell 2 is similar to steps (a)-(e) except Mold 3 is used instead of Mold 2. (f) Metallization with sputtered Ti/Cr (200Å/1000Å) on Shell 1 and Shell 2, following a brief O_2 plasma etch. (g) Assembly of hexagonal resonator in Shell 1 and application of epoxy. (h) Alignment of Shell 2 to Shell 1, followed by curing of the epoxy at 75°C for 2 hours. (i) Deflashing via the use of a heated (400°C) flash removal tool.

2.3.2. Fabrication of Packages

The first step is thermoforming. The processes for Shell 1 and Shell 2 are similar: first a thin layer of Apiezon M grease is applied in Mold 1, and the mold is heated at 340°C on a hot plate for 30 seconds. The grease acts as a lubricant and when heated it will liquefy to form a uniform layer on the surface of Mold 1, promoting the release of the shells from Mold 1 after thermoforming. Then, a pre-dried LCP pellet is cut in roughly 3 equal parts (9.4 mg each), one of which is placed in Mold 1. Mold 1 and the LCP are heated at 340°C on the hot plate until the LCP is completely melted. Using the alignment fixture, Mold 2 is aligned with Mold 1, and the assembly is placed on the 340°C hot plate with Mold 2 against the hot plate. After 1-2 minutes at the temperature to allow LCP to flow into the features of Mold 2, pressure (≈0.8 MPa) is applied on Mold 1 for 5 seconds, using a weighted block (10 kg). Applying higher pressure results in thinner flash. The mold assembly is then flipped so that Mold 1 is against the hot plate. After 20 to 30 seconds, pressure is applied for 5 seconds to Mold 2. Finally, the molds are removed from the hot plate and, upon cooling, the resulting Shell 1 is removed from the molds. Thermoforming more shells from the same molds is aided by mechanical cleaning of the molds to remove residues of grease and LCP. For fabricating Shell 2, Mold 3 is used rather than Mold 2 in the previous process flow. The internal and external features of Shell 1 and Shell 2 after thermoforming are illustrated in Fig. 2.6 (a), (b) and (c) while Fig. 2.6 (d) shows a resonator placed in the cavity of Shell 1.

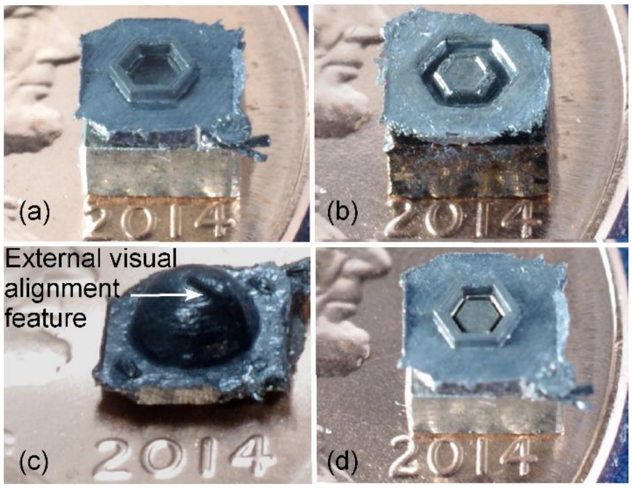

Fig. 2.6: Internal features of (a) Shell 1 and (b) Shell 2. (c) External features of Shell 1 and Shell 2. The rib is the alignment mark to denote the orientation of the packaged hexagonal resonator. (d) A hexagonal resonator placed in Shell 1.

The second step is metallization. After the molding process, thin metal layers are sputtered onto the internal surfaces of the shells to enhance interphase adhesion strength between the shells and bonding material. First, the LCP shells are ultrasonically agitated while immersed in acetone, isopropyl alcohol (IPA) and de-ionized (DI) water for 3 minutes in each solvent. After a brief, low power (~100 W for ~20 seconds) oxygen plasma etch, thin metal layers of Ti/Cr (200Å/1000Å) are sputtered on the shells to enhance interphase adhesion strength between the shells and bonding material. Finally, the metallized shells are cleaned with the same ultrasonic agitation process described previously. The SEM images of metallized Shell 1 and Shell 2 are shown in Fig. 2.7 (a) to (d).

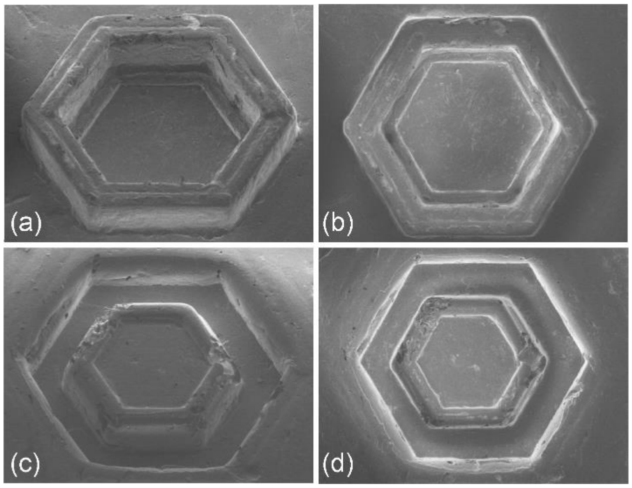

Fig. 2.7: (a), (b) SEM images of Shell 1. (c), (d) SEM images of Shell 2.

The third step is bonding. The shells are bonded with Stycast 2850FT [Sty14] (catalyzed by Catalyst 9, mixed in a 100:3.5 ratio by mass). To aide in handling and alignment of the shells, each is placed in its own Mold 1 after application of a thin layer of Apiezon M grease to the molds. A resonator is placed in the cavity of Shell 1. The Stycast epoxy is applied to the outer rim of Shell 1, then Shell 2 (in its own Mold 1) is placed on top of Shell 1, using the alignment fixture to align the molds and shells. Pressure is applied to interlock the features of the shells and to ensure epoxy contacts the mating surfaces of both shells. Finally, the epoxy is cured at 75°C for 2 hours followed by the standard solvent ultrasonic cleaning process.

The last step is deflashing. The process for the package is relatively simple and straightforward. The package is placed in Mold 1 to aide handling. The flash removal tool is heated to 400°C using a hot plate. Then, the tool is quickly used to cut through the outside flash. If the flash is not removed completely, the process is repeated until all the flash is removed.

Figure 2.8 shows the package after the bonding and flash removal processes.

The average measured mass of five packages is 17.74 mg while the calculated volume of one package, based on the mold dimensions and measured dimensions, is 10.74 mm^3. Therefore, the approximate average density of a package is 1.65 g/cm^3. The average density, and the resulting buoyancy, can be tailored by changing the size of the cavity or increasing the thermoforming pressure.

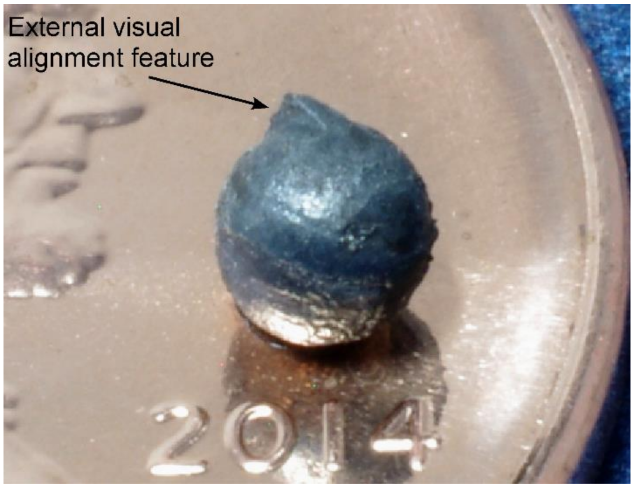

Fig. 2.8: Final package after bonding and flash removal process. The outer diameter of the package is 2.45 mm.

2.4. Experimental Methods and Results

In this section, three experimental methods and results are described. The signal response test compares the resonant amplitudes and frequencies of resonators before and after packaging and verifies whether the package or packaging processes affects the signal. The shear stress test measures the shear forces that result in the failure of the packages, estimates the shear strengths according to the area of the observed fracture surfaces, and compares the results with published material properties for LCP or Stycast. The pressure test is designed to apply high pressure to the packages and subsequently test the resonant signals of the packaged resonators, thus determining the highest hydrostatic pressure that the packages can endure before leakage, fracture, or permanent deformation.

2.4.1. Signal Response Test

In this work, the same configuration was used as that described in [Tan14] to provide a strong AC magnetic field for interrogating small quantities of packaged resonators. The interrogation system included a transmit coil, a receive coil, and two DC Helmholtz coils. The transmit coil and receive coil were 3.6 cm in diameter, 0.5 cm in length, and were oriented orthogonally with minimum separation. Both transmit and receive coils had four turns of 60-strand 22 AWG Litz wire. The two DC Helmholtz coils (100 turns each, 3B Scientific U21901) were used to provide a DC bias field, and were 12.5 cm in diameter, 3.3 cm in length, and separated by 12 cm. The setup also included a network analyzer (Agilent 4395A), an RF amplifier (Amplifier Research 75A250A) and a DC power supply (Keysight E3631A). The network analyzer provided an output signal, which is swept in frequency. The output signal was amplified by the RF amplifier and sent to the transmit coil. The receive coil was connected to a measurement channel of the network analyzer to measure the response of the resonator. The DC power supply provided the Helmholtz coils with 1.840 A of current so that a DC bias field of 31.5 Oe was applied to the resonator, allowing the resonator to reach a maximum signal amplitude [Tan14]. The strongest signal response could be measured by orienting the transmit coil and receive coil orthogonally while the DC bias field was offset by 45° from the applied AC field, as shown in Fig. 2.9.

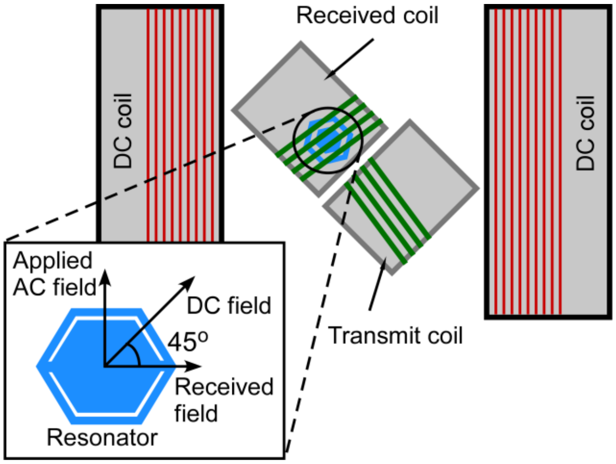

Fig. 2.9: The experimental setup for signal response test. The transmit coil and receive coil are set orthogonally while the DC bias field has an offset of 45° to the applied AC field to achieve the maximum signal amplitude.

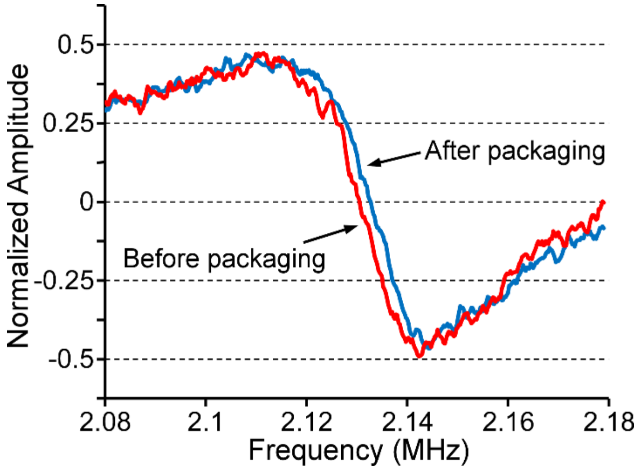

Fig. 2.10: Resonant responses of a typical frame-suspended resonator before and after packaging. The responses have similar signal amplitudes and share the same resonant frequency (2.118 MHz). The baseline signals are subtracted, a moving average of every five data points is used and the signal amplitudes are normalized.

Figure 2.10 illustrates the performances of a typical frame-suspended hexagonal resonator before and after packaging. The frequency response of the prepackaged resonator was measured when it was placed in Shell 1 before the bonding process. The traces in Fig. 2.10 were obtained by subtracting the transmit-to-receive signal feedthrough and then taking a five point moving average, and normalizing the signal amplitude to that of the typical resonator before packaging (200 μV in the case shown in Fig. 2.10, under the experimental methods mentioned previously). After packaging, the typical resonant response was similar in signal amplitude (190 μV) and possessed the same resonant frequency (2.118 MHz). The test results of five packaged resonators listed in Table 2.1 showed a sample standard deviation of 13.22 μV (7.47%) in amplitude from before to after packaging, and no measureable change in resonant frequency. This demonstrated that the package did not block the electromagnetic signal or cause a frequency shift. The signal amplitudes measured in this work (155-200 μV), both before and after packaging, were similar to those reported in [Tan14] for the resonators alone.

Table 2.1: Test results of the signal from five packaged frame-suspended hexagonal resonators. The package neither blocks the electromagnetic signal nor causes a frequency shift.

# of Resonator	Resonant Frequency f_0 (MHz)		Normalized Signal Amplitude	
	Before	After	Before	After
1	2.118	2.118	1	0.95
2	2.124	2.124	1	1.06
3	2.118	2.120	1	0.97
4	2.120	2.120	1	0.87
5	2.118	2.120	1	0.97
Average	2.120	2.120	1	0.96

2.4.2. Shear Stress Test

The shear stress test for the package was designed to use two Mold 1s to support the package. The bottom Mold 1 was to remain fixed while applying a horizontal force to the top mold (Fig. 2.11 (a)). The maximum force required to split the two shells was recorded. The working plate for the shear stress test (Fig. 2.11 (b)) had three main parts: the top clamp, the fixture and the bottom plate. The top clamp had a cover layer and a 3.66 mm wide slot to constrain the top mold and shell from any vertical movement, twisting, or flipping while allowing full movement in the direction of the applied force. The fixture part, bonded with the bottom plate, had two side barriers and one back barrier to fix the bottom mold and shell. A metal bar connected to a force gauge was used to apply horizontal force to the top mold. Lubricant was applied between the top mold and the top clamp to reduce friction against the fixture, ensuring that any shear loads would be carried by the packages only. It was thus assumed that the applied force was perfectly transferred from molds to shells. The three parts of the working plate were assembled with bolts, shims, and nuts, and attached to a stainless steel board, as shown in Fig. 2.11 (c). The material of the working plate was polymethyl methacrylate (PMMA), a kind of thermoplastic, because it is transparent and easy to machine. Acrylic cement was used as the bonding material, between layers of the PMMA.

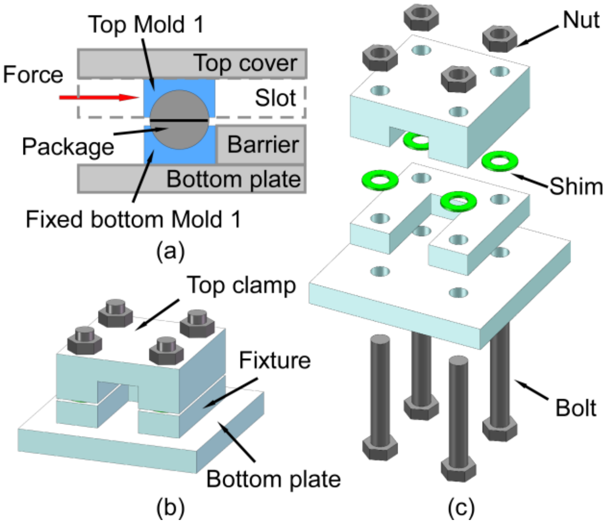

Fig. 2.11: (a) 2D conceptual diagram of the working plate for shear stress test. (b) Three main parts of the working plate: top clamp, fixture and bottom plate. (c) The exploded view of the working plate, the main structures are assembled by bolts, shims, and nuts. These illustrations are conceptual and not to scale.

Five packages were tested for ultimate shear strength. The measured shear force at failure ranged from 44.7 N to 72.3 N and had an average of 61.1 N, as described in Table 2.2. Three kinds of fracture surfaces were observed: cracks appeared at the outer boundary of Shell 2 for two samples, at the bonding surface for one sample, and at the ridge features of Shell 1 for two samples. From the varied locations of the fractured features, no singular weak point was obvious, indicating a consistent shear strength across the design. The corresponding force-resisting areas of the failures, $S_a = 1.837\ \text{mm}^2$, $S_b = 2.242\ \text{mm}^2$, and $S_c = 1.186\ \text{mm}^2$ were estimated for use in calculating the shear stress carried by the failure locations, as shown in Fig. 2.12. The calculated shear strengths of each package were also listed in Table 2.2. Since the shear strengths of the material LCP Vectra E150i and the epoxy (Stycast 2850FT with Catalyst 9) were unavailable from manufacturer data, they were estimated to be 0.577 x the manufacturer provided tensile strength, according to the von Mises yield criterion, and to be 75.01 MPa and 53.08 MPa, respectively [Vec11, Sty14]. Compared to the approximated material properties, the shear strength values from this testing were lower by 50%.

Table 2.2: Experimental results from shear stress testing of five packaged samples. The average shear force is 61.1 N and the estimated average shear strength is 32.7 MPa.

# of package	Shear Force (N)	Fracture Surface	Shear Strength (MPa)
1	44.7	Ridge	37.7
2	71.0	Boundary	38.6
3	60.1	Bonding Surface	24.8
4	72.3	Ridge	38.9
5	57.4	Bonding Surface	23.7
Average	61.1		32.7

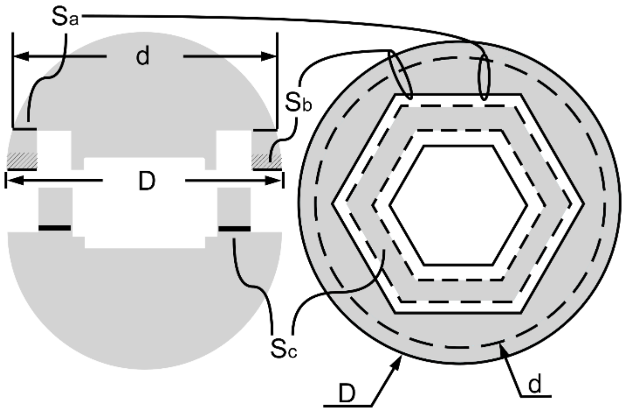

Fig. 2.12: Schematic of three force-resisting areas S_a, S_b, and S_c.

2.4.3. Pressure Test

In the pressure test, the package (with resonator enclosed) was placed inside a cylindrical steel test chamber. An Enerpac hydraulic pump (Model P142) was used to inject hydraulic oil into the test chamber and apply a pressure to the package. The pressure was then relieved, the package removed from the test chamber, and the signal from the resonator measured (as described in Section 2.4.1). The signal amplitude of the resonator would reduce dramatically with any oil leakage into the package. Thus, a visual assessment of the package as well as measurement of the resonant signal after the application of pressure can be used to determine how much pressure the package could endure before leakage, structural fracture, or permanent deformation of the package.

Two packaged resonators were tested with this procedure. Both packaged resonators provided a response similar to their pre-packaged responses upto a pressure of 2000 psi (≈13.8 MPa) was applied (Fig. 2.13). However, once the applied pressure exceeded 2000 psi, the signal response was indistinguishable from noise (20 μV). For both cases, the packages did not have a structural failure after the pressure test, indicating that lack of hermeticity in the bond was the failure mode.

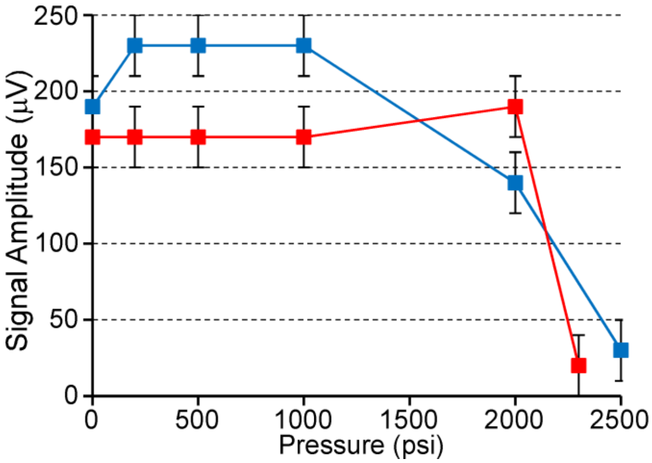

Fig. 2.13: Pressure tests for two packaged samples. Both appear unaffected by pressures up to 2000 psi.

2.5. Conclusion

Thermoformed LCP packages with an outer diameter of 2.45 mm were successfully fabricated. The test results indicate that the packaging does not hinder the magnetoelastic signal while providing protection against useful shear and pressure loads. This enables applications that require distribution of the resonators into small tubes and piping systems which may have viscous liquids at high pressures, and subsequent long distance resonator interrogation. For this work, the DC bias field is provided by an external electromagnet, which would need to be replaced by a permanent magnet material embedded in the package for long distance interrogation.

This work shows that LCP is promising for thermoformed packaging because of its excellent electrical, mechanical, thermal, and chemical properties. It can be thermoformed with good dimensional stability and feature size down to 20 μm. The cost of LCP processing costs for thermoforming are much lower than those for other materials and for microinjection molding. In the future, molds can be machined by batch-mode μEDM, resulting in a thermoforming process that, with some adjustments, could produce packages in batches.

Chapter 3: 3D-Printed Package for Magnetoelastic Sensors in an Integrated Plastic Biliary Stent Wireless Monitoring System

3.1. Introduction

This chapter describes approaches for addressing the practical challenges facing the delivery of a previously reported integrated system [Gre13] for non-invasive, wireless measurement of sludge accumulation in a plastic biliary stent. Specifically, previously performed animal tests with this system demonstrated that the magnetoelastic sensors – which were completely exposed inside the biliary stent – could easily be damaged by the inserted introducer during the implantation process. Figure 3.1 (a) highlights a monitoring system that can provide a direct and wireless measurement of biomass accumulation in a plastic biliary stent with an instrumented magnetoelastic sensor. To improve this system, new magnetoelastic resonators and complementary packages are designed. The compromise between two polymer-based packaging approaches – one mechanically flexible (Type F) and one mechanically stiff (Type S), as shown in Fig. 3.1 (b) and (c), – is evaluated here. The packages protect the sensor from being damaged by the introducer, establish a more integrated sensing module with built-in DC bias, and allow the bile and biliary sludge to access the resonator surfaces. The designs of the two types of the packages, the resonators, and the bias magnets are presented in the first section. The fabrications and the assembly approaches are then shown in detail. Finally, the benchtop mechanical and signal performances are evaluated.

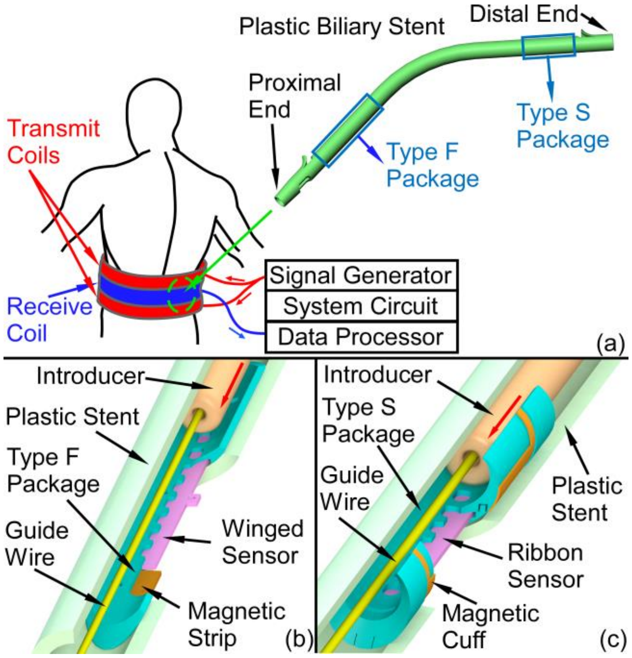

Fig. 3.1: (a) Conceptual diagram of the magnetoelastic monitoring system and the plastic biliary stent. (b) Cross-sectional views of Type F and (c) Type S 3D printed packages, which integrate magnetoelastic sensors and magnets. The Type F package can be assembled near the proximal end of a plastic stent while the Type S package can be assembled near the distal end. Both package designs do not impede the stent as it is loaded on the guide wire and introducer.

3.2. Design

3.2.1. Package Design

For the proposed application, the package material should be biocompatible, chemically inert at body temperature, and electromagnetically transparent. The fabrication technique should facilitate the integration of features with high resolution (a few hundreds of microns) and, if possible, be inexpensive. Of critical importance, the package – once assembled to the stent – must be capable of passing through the endoscope during delivery without impeding the capability of the endoscopist to place the stent as desired. The stents used in this work are Cotton-Leung Biliary Stents (G22056 and G21847). They have outer diameters of 0.33 cm (10 Fr) and 0.38 cm (11.5 Fr), respectively. The lengths are 7 cm and 9 cm, respectively. The standard endoscopic procedure requires the aid of a side-viewing endoscope, which has a camera to locate the position of the biliary orifice and an elevator to adjust the direction of the stent, as shown in Fig. 3.2. Fig. 3.2 (a) and (b) show the elevator of the endoscope is lowered and raised, respectively, while Fig. 3.2 (c) illustrating the schematic of the endoscope profile with the lowered or raised elevator. When the elevator is lowered, the stent (and packaged sensor) must pass through a radius of curvature of approximately 7.2 cm. When the elevator is raised, the stent (and packaged sensor) must survive a radius of curvature of approximately 2 cm. Once the proximal end of the stent is aimed at the biliary orifice, the elevator can be lowered for a smoother delivery and the stent is then pushed into the bile duct by the introducer assembly. Therefore, the front (proximal) part of the stent needs to maintain flexibility, whereas the flexibility of the latter (distal) part of the stent is not critical. Correspondingly, the flexible Type F package can be placed near the proximal end of the stent while the stiff Type S package is appropriately placed near the distal end of the stent (i.e., the end that is located in the duodenum).

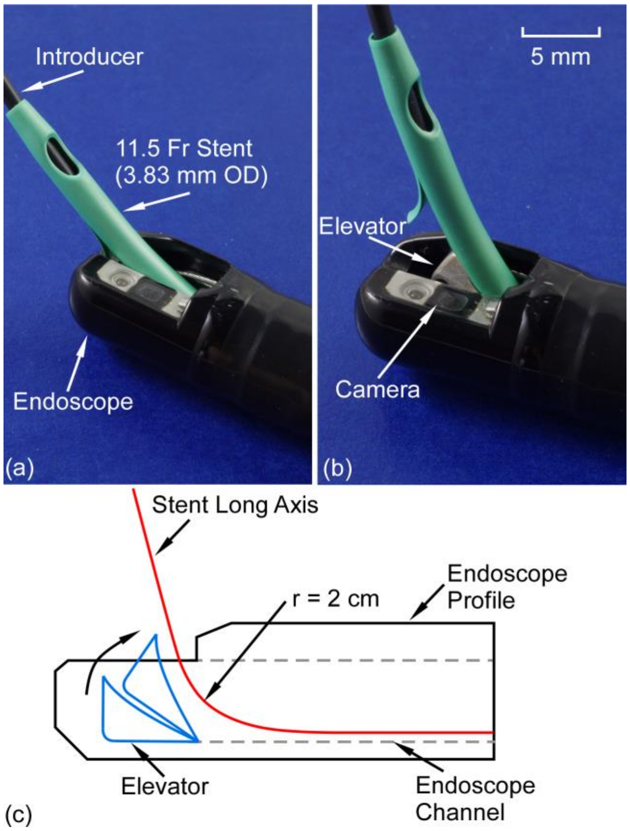

Fig. 3.2: The elevator of the endoscope is (a) lowered and (b) raised at maximum angle. The largest radius of curvature is approximately 7.2 cm (elevator lowered) while the smallest is 2 cm (elevator raised). (c) Schematic of the endoscope profile and the estimated minimum radius of curvature of the stent.

Fig. 3.3 and Fig. 3.4 show the 3D drawings of the polymeric Type F and Type S packages, respectively. The two package types differ mainly in their bending flexibility, with the Type F package intended to be flexible and the Type S package intended to be rigid. Common features in both types include the perforated cavity in which to place the sensor while allowing the bile and sludge to interact with the sensor, tapered ends and curved surfaces to guide the introducer over the package smoothly, and tether holes that facilitate stitching with polyethylene thread the components and the package into the stent.

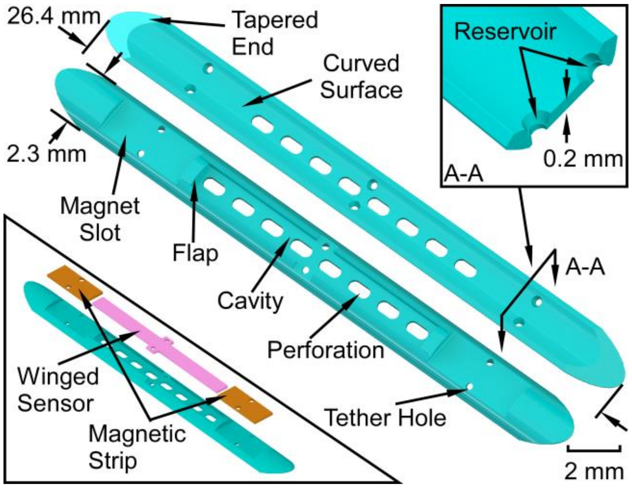

Fig. 3.3: Schematic of the top and bottom views of the Type F package. The bottom left inset shows the assembly of the magnetic strips and winged sensors. The top right inset indicates a cross section view of the reservoir feature.

The Type F package in Fig. 3.3 is 26.4 mm long, 2.3 mm wide and only 0.53 mm thick. The sensor and the magnetic strips are assembled in the package, as shown in the bottom left inset. The sensor cavity is 13 mm long, 1.2 mm wide, and 0.25 mm deep. The flaps at the two ends of the sensor cavity are to prevent the sensor from sliding out of the cavity. The two flaps are both 0.45 mm long, 1 mm wide, and only 0.13 mm thick. The two magnet slots are both 4 mm long and 1.7 mm wide for placing the magnetic strips. There are six tether holes and the reservoir on each tether hole (shown in the top right inset) can accommodate reflowed PE material, which forms a recessed head to anchor the tether to the package as well as to provide a smooth profile on the top surface of the package.

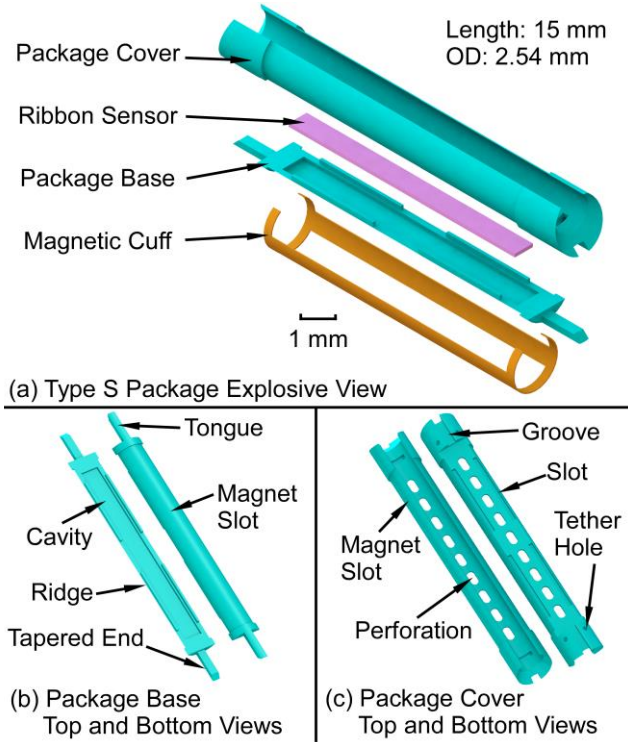

Fig. 3.4: (a) The exploded view of the Type S package. (b) The top and bottom views of the package base. (c) The top and bottom views of the package cover.

Fig. 3.4 (a) shows the exploded view of the Type S package. The ribbon sensor is encapsulated by the package base and cover and a magnetic cuff is clamped on the package. The overall length is 15 mm and the outer diameter is 2.54 mm. The top and bottom views of the package base and cover are shown in Fig. 3.4 (b) and (c). The package base has a 13 mm long, 1.2 mm wide, and 0.18 mm deep cavity in which to place a ribbon sensor (12.5 mm x 1 mm x 60 μm) that is otherwise unconstrained. This is in contrast to the approach in the Type F package, which utilizes a single-piece package with the sensor anchored to the package by a PE tether. Four 4.5 mm long, 0.15 mm wide, and 0.2 mm thick ridge features and two 1.77 mm long, 0.52

mm wide, and 0.31 mm thick tongue features in the package base are designed to match and interlock with the package cover, which has complementary features (slots and grooves). The hollowed area in the package cover is designed to be large enough to let the introducer (Φ1.7 mm) pass through. Both package base and cover are reduced in diameter by 100 μm in selected areas to form magnet slots.

The package approach should minimize increases to the flow resistance of the stent. According to Darcy–Weisbach equation, the pressure loss ΔP in a cylindrical tube of uniform diameter *D* is proportional to length *L*:

$$\frac{\Delta P}{L} = \frac{128}{\pi} \cdot \frac{\mu_f Q_r}{D^4} \tag{3.2.1.1}$$

where μ_f is the dynamic viscosity of the fluid, and Q_r is the volumetric flow rate. The flow resistance R_f can be represented as

$$R_f = \frac{\Delta P}{Q_r} = \frac{128}{\pi} \cdot \frac{\mu_f L}{D^4} \tag{3.2.1.2}$$

For a 90 mm long 11.5 Fr stent, the flow resistance change for the entire stent with the Type F package is approximately +13% assuming the equivalent diameter of the channel which contains the package is 2.4 mm, while that of the stent is 2.63 mm. After calculating in a similar manner, the total flow resistance change for a 70 mm long 10 Fr stent with the Type S package is approximately +83% when the diameter of the hollowed area is 1.8 mm and the diameter of the stent is 2.53 mm.

The two packaging approaches here have significantly different effects on the bending stiffness of the stent. The bending stiffness of a portion of an 11.5 Fr stent (3.83 mm OD and

2.63 mm ID) containing the Type F package can be calculated as the sum of the bending stiffness of each component:

$$k_{F\_total} = k_{11.5} + k_F \tag{3.2.1.3}$$

where

$$k = \frac{48EI}{L^3} \tag{3.2.1.4}$$

E is the Young's modulus of the object, I is the second moment of area, and L is the length [19]. For a cylindrical tube, $I = 0.78(r_o^4 - r_i^4)$, while for a rectangular beam offset from the bending axis of the stent by a distance $\left(r_i - \frac{h}{2}\right)$ – which the Type F package is approximated as here – $I = \frac{bh^3}{12} + (bh) \cdot \left(r_i - \frac{h}{2}\right)^2$. The parameters r_o and r_i are the outer and inner radii of the tube while b and h are the width and thickness of the beam (2 mm and 530 µm, respectively). The Young's moduli of the stent and the package materials are 700 MPa and 1463 MPa, respectively. For the Type F package (L = 26.4 mm), $k_{F\_total} = k_{11.5} + k_F = 14.9\ \mathrm{N/mm} + 4.6\mathrm{N/mm} = 19.5\ \mathrm{N/mm}$.

Similarly, the total bending stiffness of a 10 Fr stent (3.33 mm OD and 2.53 mm ID) containing a 20 mm long Type S package (approximated as a cylinder with 2.53 mm OD and 1.8 mm ID) is $k_{S\_total} = k_{10} + k_S = 16.8\ \mathrm{N/mm} + 13.0\ \mathrm{N/mm} = 29.8\ \mathrm{N/mm}$. The change in the bending stiffness of the stent due to the Type F package is 31% while the change due to the Type S package is 78%. The calculated bending stiffness of the Type S package does not include the additional magnetic cuff, which, due to the large Young's modulus of the Arnokrome™ 5 material and the geometry of the cuff, adds further stiffness to the Type S package overall.

The changes to the stent bending stiffness due to the Type F and Type S Packages are also simulated with finite element analysis (FEA, COMSOL Multiphysics) to verify the simplified analytical calculation described above. The material properties of the stent (polyethylene, E = 0.7 GPa, ρ = 0.95 g/cm^3, ν = 0.42) and the package (M3 crystal resin, E = 1.46 GPa, ρ = 1.02 g/cm^3, ν = 0.42) are the same as that used in the analytical calculation. Figure 3.5 (a) presents the cross sectional view of the 11.5 Fr stent with the Type F Package, and the boundary conditions used in the FEA model. The stent is 26.4 mm long and the package is affixed to the inner side wall of the stent. Some features of the package like the flaps are removed because they will not significantly affect the result while substantially increasing simulation time. The loads and conditions are defined to approximate the classical "three-point bending test". Points a and b have zero displacement along the y axis to prevent rolling, point c is fixed in all directions, and point d has zero displacements in y and z directions but can move along x axis. An external force which increases from 0 to 10 N is applied on the middle of the stent in the negative z direction. The length of the stent loaded by the force is 2 mm. Figure 3.5 (b) shows the deformation of the Type F Package when the applied force is 10 N. (The deformed stent is hidden in this view.) The maximum displacement of the stent, which is at the middle of the stent, is less than 0.90 mm. The bending stiffness of the stent with and without the Type F package are illustrated by the slopes of the load vs. displacement lines (Fig. 3.6). The bending stiffness of the stent only increases from 10.61 N/mm to 11.34 N/mm (+7%). Similarly, the 10 Fr stents with and without the Type S Package are also simulated in COMSOL. In this simulation, the bending stiffness of the stent increases from 8.41 N/mm to 19.48 N/mm (+132%). Although the absolute values of the bending stiffness are not same as the analytical calculation (an effect mainly of the radial compression of the stent in the simulation), the changes in the bending stiffness due to each package are similar in both analytical and FEA estimates. For the Type S Package, the additional magnetic cuff will further increase the total stiffness in that section of the stent.

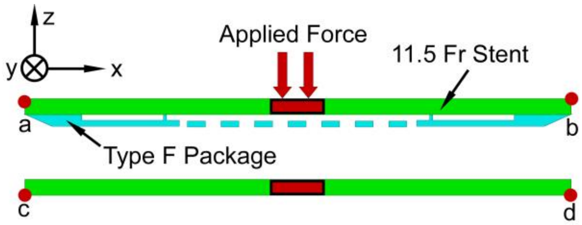

(a) Cross sectional view of the simulation geometry

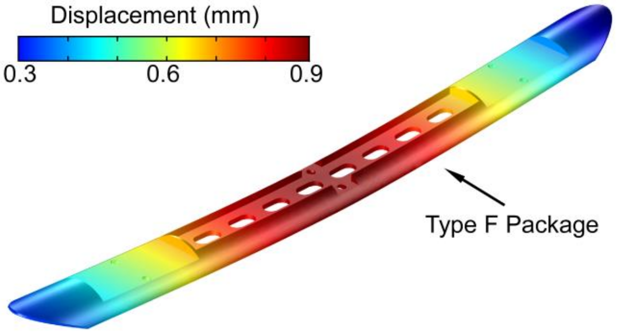

(a) Deformation of the Type F Package

Fig. 3.5: (a) Cross sectional view of the 11.5 Fr stent with the Type F Package. The stent length is 26.4 mm. The external force is applied on the red surface of the stent, which is 2 mm in length. (b) FEA simulation result of deformation of the Type F package when under 10 N applied force.

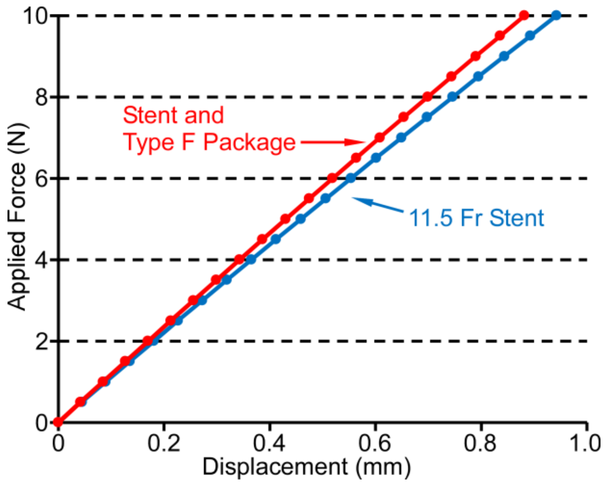

Fig. 3.6: Displacement of the stent with and without the Type F Package due to the external applied force.

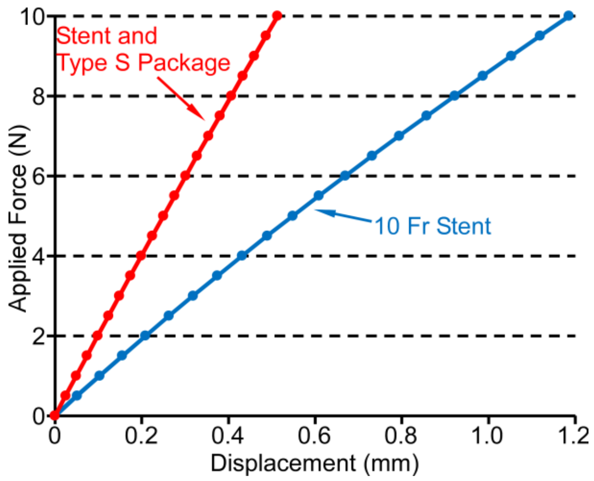

Fig. 3.7: Displacement of the stent with and without the Type S Package due to the external applied force.

3.2.2. Magnetoelastic Sensor Design

Magnetoelasticity describes the coupling between stress, strain, and magnetism [Eng00]. When exposed to a time-varying magnetic field, the magnetic domains in a magnetoelastic material tend to rotate and align with the changing field, affecting the strain of the material and causing mechanical vibrations. As a response, the vibrations in the material generate another oscillating magnetic flux, which can be detected by wireless methods [Gri02, Gri11]. Changes in the mass loading and the density/viscosity of the medium surrounding a magnetoelastic sensor can be measured by the shifted resonant frequency and quality factor of the resonance. These resonance characteristics can reflect the bile sludge accumulation and the stent blockage as the pathology progresses.

A two-layer bonded magnetoelastic ribbon-shaped sensor is chosen for this application. This approach has high signal-level-to-footprint efficiency, which is critical for accommodating the size constraints imposed by the biliary stent. The resonant frequency f of the vibration along the longitudinal axis of the unloaded sensor is determined by:

$$f_n = \frac{n}{2L_s}\sqrt{\frac{E}{\rho_s}} \qquad n = 1, 2, 3 \tag{3.2.1.5}$$

where L_s is the length of the ribbon, E is the Young's modulus, and ρ_s is the density of the sensor. In this application, the fundamental resonant frequency is considered ($n = 1$) due to the benefits of larger signal strength and lower frequency (which results in less attenuation through electrically conductive tissue).

For a 12.5 mm long and 1 mm wide ribbon sensor fabricated from Metglas^{TM} 2826MB (E_s = 100 GPa, ρ_s = 7.90 g/cm^3), the expected resonant frequency is 168.7 kHz, which is also estimated by the finite element analysis (FEA) result (COMSOL Multiphysics) [Gre09b]. For the sensor used in the Type F package, two additional 0.8 mm x 0.4 mm wing features with two ϕ0.3 mm tether holes are in the middle of the sensor for anchoring it in the package with minimum impact on the normal vibration. The maximum displacement of the winged sensor is 30 nm according to the FEA simulations (with a simulated 22.3 A/m interrogation field, Fig. 3.8), while that of the ribbon sensor shows a similar result of 32 nm at 166 kHz.

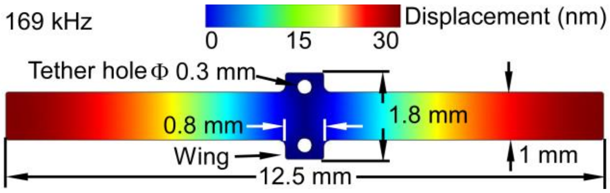

Fig. 3.8: FEA simulation result of the winged sensor – used with the Type F packages – with the wings anchored. The sensor resonates at 169 kHz in a longitudinal mode shape with a maximum displacement of 30 nm.

3.2.3. Bias Magnet Design

Although magnetoelastic transduction is generally non-linear, it can be treated as linear when small exciting fields are used. In this approach, the operating point of the sensor is set by the bias (steady) magnetic field. An appropriate choice of this point can optimize the small-signal magnetostrictivity, and thus maximize the sensor vibration and signal amplitude. Additionally, due to the coupling between the magnetism and strain, the bias magnetic field also affects the apparent Young’s modulus of the material, the phenomenon which is called the ΔE effect. Our previous test results [Gre09a] showed that changing the DC bias field or orientation could have a large effect on the resonant frequency. In this application, the shift of the resonant frequency caused by the change of the bias field may result in misdiagnosis and thus should be avoided by specific means.

One promising method for avoiding a change in bias field is to integrate the permanent magnet(s) into the package and alongside the sensor, thus providing a constant bias to the sensor regardless of external equipment orientation. The process for sizing and locating the magnets in this work is empirical in nature, and consists of manually cutting prototype magnets of various sizes, magnetizing them using an impulse magnetizer (American Scientific High Strength Magnetizer), and experimentally varying the arrangement between the magnets and the sensor while measuring the sensor response. For the Type F package, the magnets need to be close to the inner sidewall of the stent and as short as possible to maintain the overall flexibility of the assembly. Therefore, two 4 mm x 1.5 mm x 60 μm Arnokrome^{TM} 5 magnetic strips are designed and placed close to the two ends of the winged sensor for biasing, as shown in Fig. 3. An appropriate distance between the magnets and the sensor is experimentally determined to be 100 μm. Two 0.3 mm tether holes in the middle of both magnets are designed for fixing the magnetic strips in the package. For the Type S package, the DC magnetic bias is provided by two 14 mm x 1 mm Arnokrome^{TM} 5 magnetic strips, which are oriented along the length of the package and held in place on the package with two cuffs that are monolithically formed at the ends of the strips, as shown in Fig. 4 (a). In this case, the magnetic strips can also increase the bending stiffness of the assembly.

3.3. Fabrication and Assembly

3.3.1. Fabrication of Package

The need for flexibility, electromagnetic transparency, and cost exclude most ceramics and metals as the packaging materials and point toward the use of polymers, as described in Chapter 2. A commercial 3D printing technique for fabricating polymer packages, compared to conventional injection molding of plastics, has benefits including more rapid iteration (without large capital costs for building injection molding tools) and the ability to build in undercuts and other features that are extremely challenging for injection molding. "M3 crystal" resin is a USP Class VI biocompatible rated plastic 3D printing material [Pro17a, Pro17]; other common 3D-printing materials like polylactic acid (PLA) and acrylonitrile butadiene styrene (ABS) fail to meet the biocompatibility requirement [Wah16]. The multiJet (MJP) printing technology utilized has a layer resolution of 16 μm and a minimum (lateral) feature resolution of 200 μm [Soc16, Bha16].

The Type F packages were printed by the ProJet 3500HD Max from 3D Systems, as shown in Fig. 3.9. A Type F package with integrated winged sensor and magnetic strips is also shown in the figure. The top and back views of the package bases and covers of the Type S package are shown in Fig. 3.10 (a) and (b), respectively. The front and side views of a Type S package with integrated ribbon sensor and rolled magnetic cuff are shown in Fig. 3.11 (a) and (b), respectively.

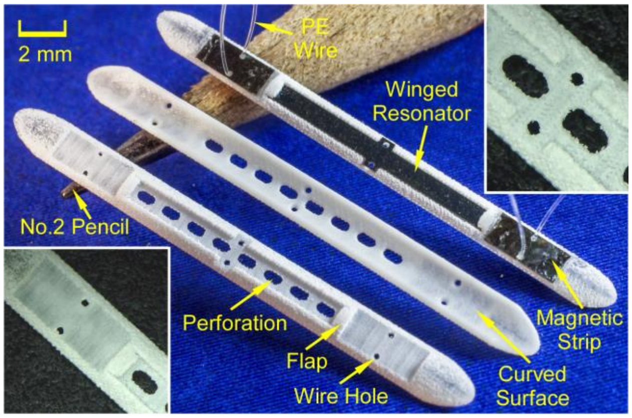

Fig. 3.9: Top and back views of the 3D printed Type F package. A resonator and magnets integrated with the package is also shown. The insets show details near the flap (bottom left) and the center perforations (top right).

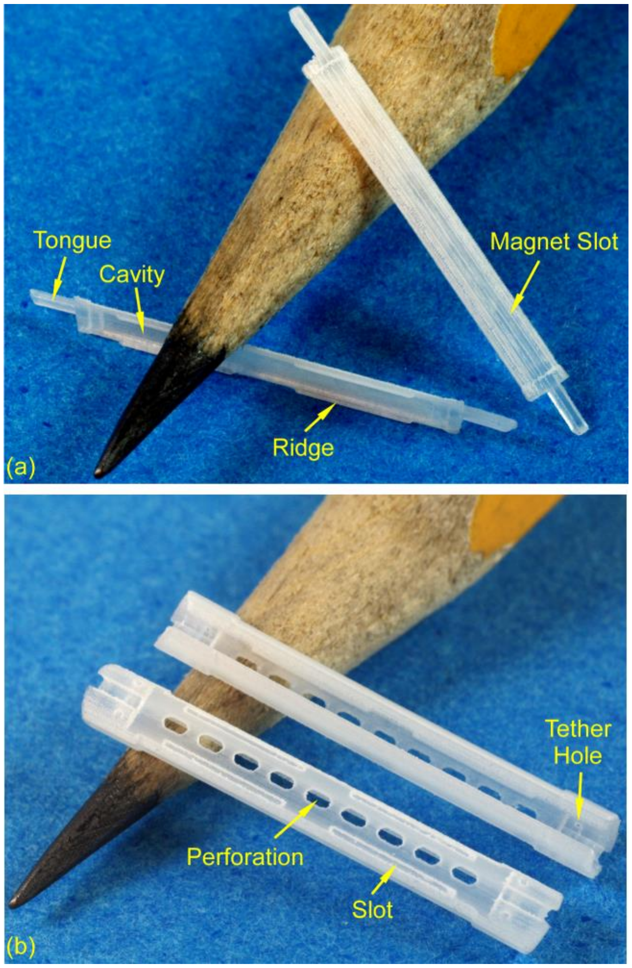

Fig. 3.10: (a) Top and back views of the 3D printed Type S package base. (b) Top and back views of the 3D printed Type S package cover.

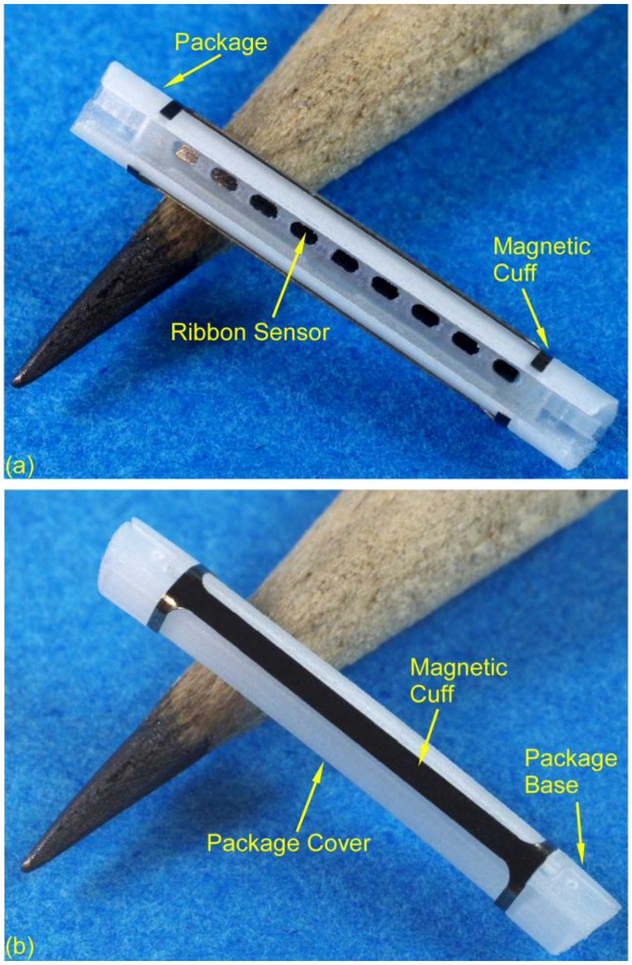

Fig. 3.11: (a) Front and (b) side views of the Type S package with the magnetic cuff.

3.3.2. Fabrication of Sensors and Magnets

The magnetoelastic sensor material was the iron-rich amorphous ferromagnetic alloy Metglas^{TM} 2826MB foil (28 μm thick). Two layers of the foil were bonded together by using the gold-indium (Au-In) eutectic bonding process [Vis13, Akt13, Tan13] in order to enable resonators with larger signal without affecting the footprint of the resonators. The bonded Metglas^{TM} foils were then machined to form winged sensors and ribbon sensors by using micro electro-discharge machining (μEDM) [Tak02, Ric10]. In addition, the Metglas^{TM} material has been confirmed to need coating for purposes of biocompatibility and signal stability in liquid environments [Gre13]. Therefore, the sensors were coated by 100 nm thick Al_2O_3 using the atomic layer deposition (ALD) [An14] technique to prevent corrosion and for purposes of biocompatibility, as shown in Fig. 3.12. The μEDM and ALD approaches were also used to machine and coat the Arnokrome^{TM} 5 magnetic alloy foils [Arn11], as shown in Fig. 3.13.

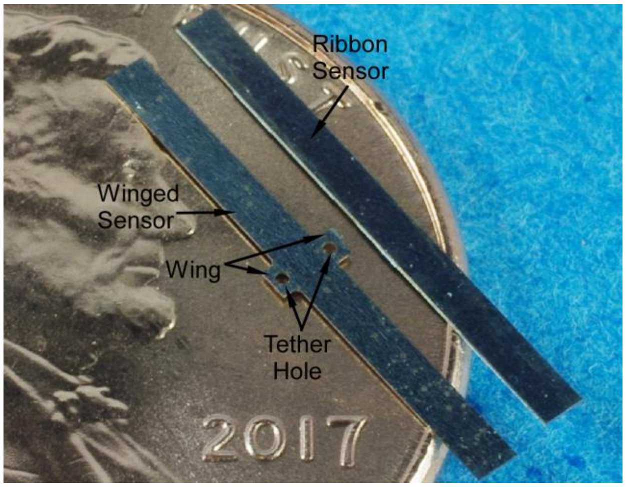

Fig. 3.12: Au-In bonded (a) winged sensor and (b) ribbon sensor coated with 1000 Å Al_2O_3.

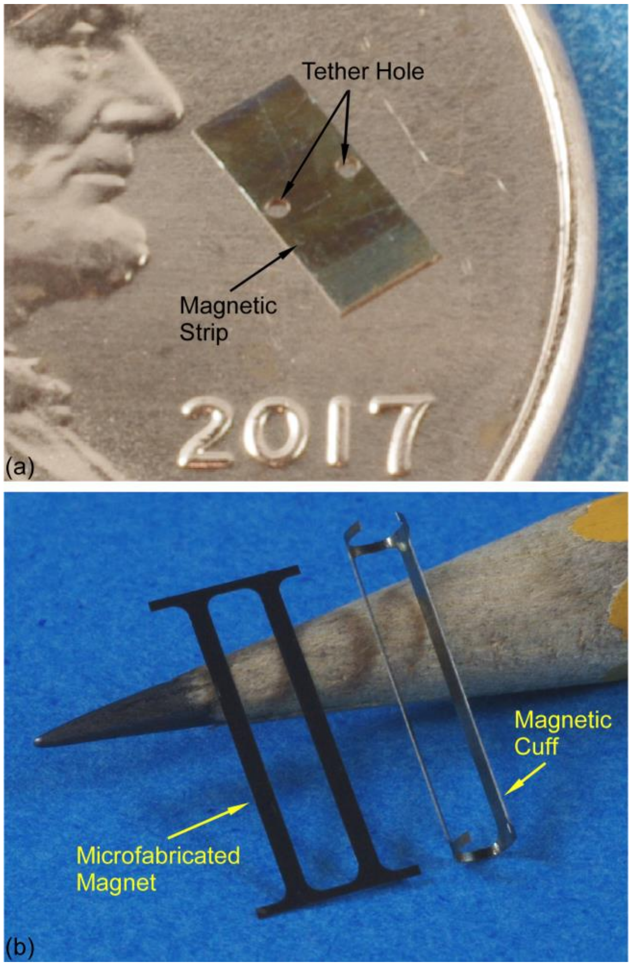

Fig. 3.13: (a) Microfabricated magnetic strip coated with 1000 Å Al_2O_3 for the Type F package. (b) Microfabricated magnetic strip (left) and the magnetic cuff (right) after rolling for the Type S package.

3.3.3. Assembly to the Stents

The assembly process flow for the Type F package was as follows. First, the winged sensor and the two magnets were placed in the proper position of the package (as shown in Fig. 3.3). Then, six 150 μm diameter PE tethers were threaded through the holes on the package and those on the magnetic strips and winged sensor. The top end of each PE tether was tied to form a square knot and then melted by a heated soldering iron to reflow into the reservoir. Next, bilateral 20 mm long slices were cut from the proximal flap hole by a razor blade, and the resulting flap was peeled open to facilitate access to the internal stent lumen. Subsequently, the PE tethers on the package were threaded through the holes on the stent, which were aligned to the positions of the holes on the package, and were pulled taut to make the package sit close to the inner sidewall of the stent. These tethers were then used to tie three square knots on the outside of the stent. The slices in the stent were closed and sealed by a heated soldering iron. The soldering iron was also used to melt the knots on the outside of the stent into the material of the stent and to smooth the resulting bumps. A schematic of the assembly is shown in Fig. 3.14. The assembled 11.5 Fr stent is shown in Fig. 3.15 (a).

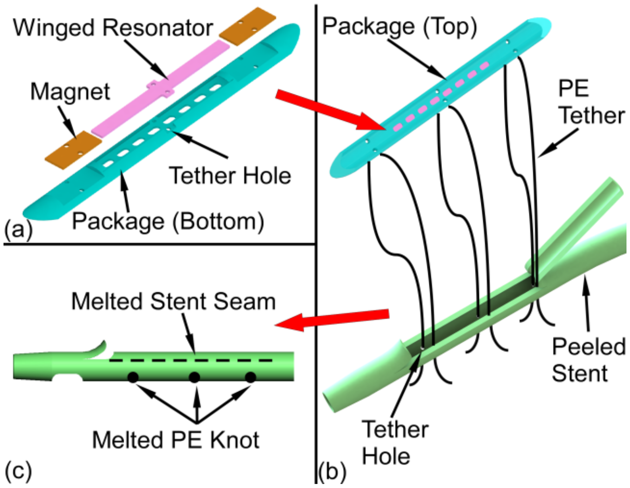

Fig 3.14: Process flow of assembling a packaged magnetoelastic sensor into a 11.5 Fr plastic biliary stent.

For the Type S package, there were only four PE tethers that needed to be threaded through the holes on the stent, which were close to the distal end of the stent. Thus, the Type S package was assembled to the stent without slicing the stent. A 10 Fr stent (Φ 2.53 mm) was used, while other processes were similar to that for the Type F package, as shown in Fig. 3.15 (b).

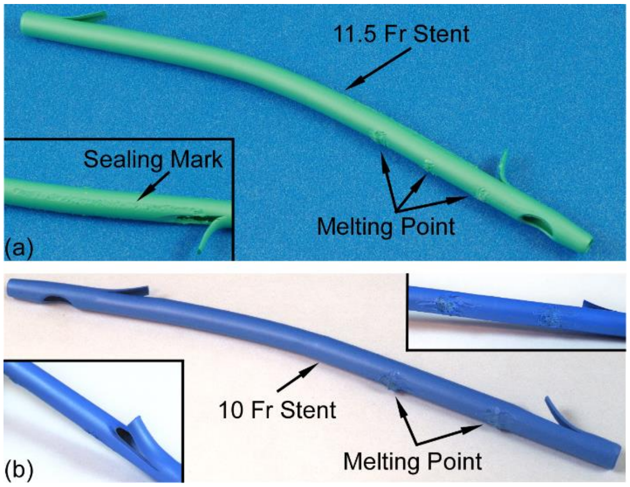

Fig. 3.15: (a) Side view of an assembled 11.5 Fr stent with Type F package integrated. The melting points and the sealing mark can be observed. (b) Side view of an assembled 10 Fr stent with Type S package integrated. The melting points can be observed in the top-right inset. The stent does not need to be cut for assembly.

3.4. Experimental Methods and Results

3.4.1. Mechanical Evaluation

The purpose of the mechanical evaluation was to examine the robustness of the package during implantation. The first test was to verify the ability for an introducer to pass through the stent with the package assembled inside, without damaging the packaged sensor. A 2 mm and a 1.7 mm diameter introducer (G25381 and G25377, Cook Endoscopy) were used to insert into and remove from the biliary stents with the assembled Type F and Type S packages, respectively, for 20 times each. The overall insertion and removal processes were smooth as determined manually. The stents were opened after each trial for observation and sealed for the next trial. Neither the packages nor the PE tethers broke during these tests, and no snagging or wear was observed for any component.

The second mechanical test evaluated the elasticity and bending stiffness of the two types of package during the delivery through the endoscope. A test set-up for this test consisted of a soft polymer tube with inner diameter of 3.5 mm, fixed at one end on a rigid cardboard sheet by a zip tie while the other end was free. The stent was inserted in the soft tube and the tube was bent to have radius of curvature of 10 cm to 1 cm and 3 cm for the Type F and Type S package embedded stents with 1 cm interval, respectively. The stent and package was bent in three directions during separate trials of this test: concave and convex along the longitudinal axis of the package, and along the lateral axis of the package. For the Type F package, when bending the stent along the width axis of the package, the stent would partially rotate within the soft tube in order to align the more flexible bending axis of the package with the applied bending direction and thus reduce the applied stress. For the Type S package, the area of the stent where the package was located remained straight even as the rest of the stent was curved in the soft tube. In each test case, the tube was maintained in a bent condition for 1 minute and then pulled out from the soft tube for examining. The packages did not have cracks and the PE tethers did not break in all test cases.

3.4.2. Signal Evaluation

In this work, the interrogation system, as shown in Fig. 3.16, included two 30-turn parallel connected transmit coils and a 28-turn receive coil to generate AC magnetic field and receive the response signal from the resonator, respectively. The AC magnetic field was excited by a sine wave generator (PXI 5412, NI) controlled by a switch. In this approach, a sine wave burst at one frequency is transmitted to excite the sensor, then the sensor "ring down" response is measured between bursts. After low noise preamplification (LNA, Stanford Research Systems SR 570), the sensor response signal was recovered by a series of digital signal processing (DSP) techniques after acquisition with a PXI 1082 module. The DSP, implemented by LabVIEW, used averaging, moving bandpass filtering, quadrature mixing, and low pass filtering to minimize the noise. The total energy of the recovered "ring down" signal at each frequency was calculated via integration and compared to the total energy of the noise to get a signal-to-noise ratio (SNR) plot along the swept frequency range[1].

The buffer (BUF634P, TI) could provide a high output current of ±250 mA to drive the transmit coils. The over-voltage protection was implemented by a metal-oxide varistor (MOV,

---

[1] The interrogation module and signal processing approach was contributed by fellow student Ramprasad Nambisan.

V18ZA1P Littelfuse), which could be conductive when the voltage was above 18 V so that the flyback voltage of the transmit coils – generated when switching off the transmitted burst – would not destroy the buffer or the signal generator. The logic signal switch (DG419L, Maxim) was controlled by the PXI 1082 to prevent feedthrough from the transmit coil and avoid overloading the LNA. The over-current protection module limited the maximum input current of the LNA if the switch failed in a shorted condition.

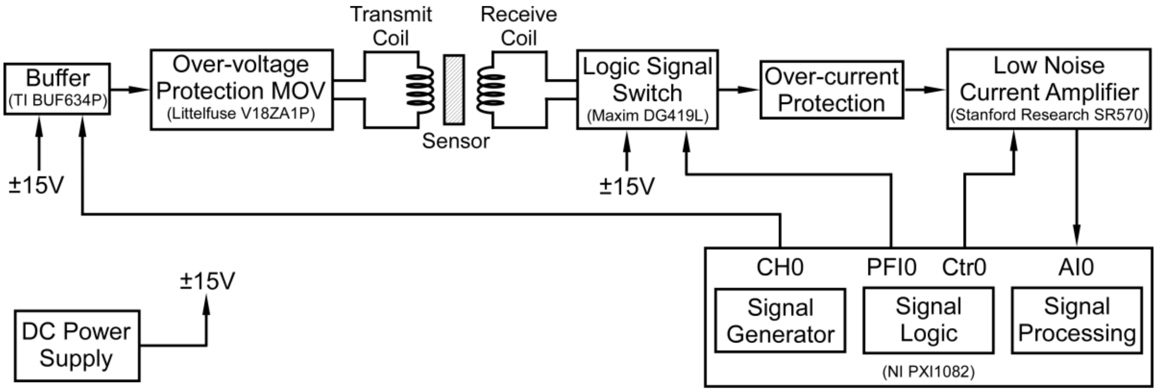

Fig. 3.16: Block diagram of the interrogation system.

The sensor signal was measured after each bending test case mentioned above, after allowing the stent to revert to its undeformed shape. The test results demonstrated that none of the bending cases affected the signal or resonant frequency. Typical frequency responses of the Type F package after being exposed to convex bending conditions with radii of curvature from 4 cm to 1 cm, and then allowed to return to the undeformed state, are shown in Fig. 3.17.

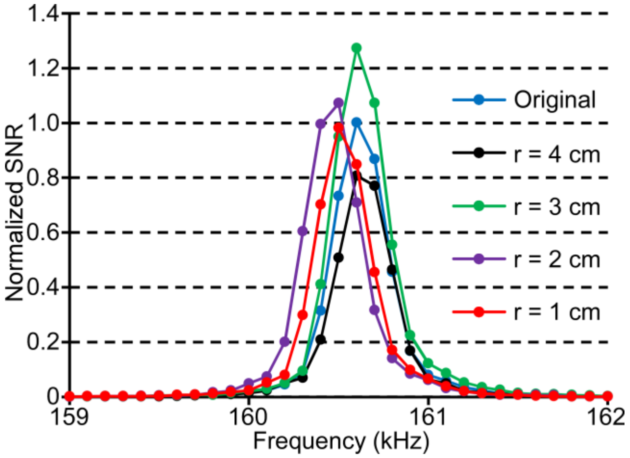

Fig. 3.17: Frequency response of a typical sensor in the stent-assembled Type F package after the convex bending test with radius of curvature from 4 cm to 1 cm. In this case, the stent was allowed to return to its resting state while measuring the response.

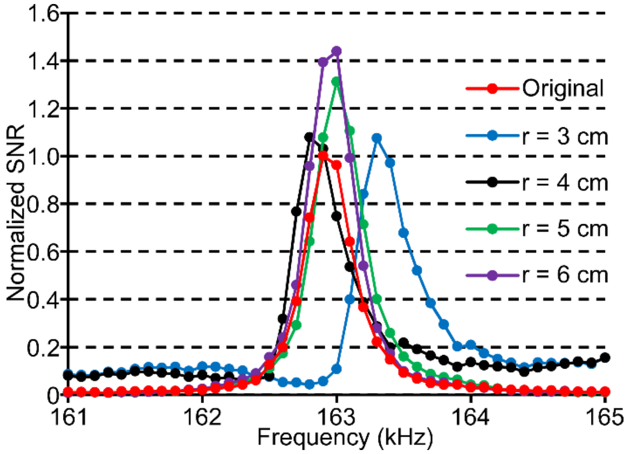

Fig. 3.18: Frequency response of a typical sensor in the stent-assembled Type S package under the convex bending condition with radius of curvature from 6 cm to 3 cm. In this case, the measurement was taken while the stent was in the curved state.

Although the above tests showed the sensor in the Type F package survived when the stent was relieved from the bending state, the signal of the sensor measured while the stent was still under bending condition decreased dramatically when the radius of curvature was smaller than 10 cm, as shown in Table 3.1. The comparable bending test result from the Type S package is also shown in Table 3.1. The signal amplitude remained high for the Type S package even as the global radius of curvature of the tube was reduced to 3 cm, showing that the Type S package could keep the ribbon sensor straight while the remainder of the stent accommodated the bending of the tube. Typical frequency responses of the Type S package and resonator under the convex bending condition with global radii of curvature from 6 cm to 3 cm are shown in Fig. 3.18.

Table 3.1: Bending test result of the biliary stent with the Type F or Type S package in a curved soft tube.

Radius of Curvature (cm)	Normalized Signal	Resonant Frequency (kHz)
Type F Package		
Straight	1.00	160.5
10	0.57	160.6
9	0.09	160.6
8	0.06	160.5
7	0.07	160.6
6	0.04	160.5
Type S Package		
Straight	1.00	163.1
6	0.91	163.3
5	0.96	162.8
4	0.83	163.0
3	0.90	163.0

3.5. Conclusion

Two types of 3D-printed polymeric packages for magnetoelastic sensors and bias magnets were fabricated, assembled in plastic biliary stents, and evaluated for performance. The Type F package showed the advantage of flexibility during the delivery process while the Type S package maintained sensor signal even when the stent was under a bending condition. The packaging and assembling processes did not affect the signal or the resonant frequency of the sensors. The benchtop experimental work described here also demonstrated that the packages could protect the sensor from being damaged by the introducer and during the tortuous endoscopic delivery of the stent.

Chapter 4: Animal Test Results

4.1. Introduction

The benchtop tests of the two types of packages indicated that the packages provided protection to the sensor from the introducer, that the packaged resonators could be delivered endoscopically, and that the packages did not impede the sensor signal. However, one of the main differences between the benchtop tests and the real implantation process are that the biliary stents need to be deployed by a doctor, who should not be required to have extra knowledge on the device or be expected to accommodate the instrumented stent in a way that compromises a safe delivery. The other difference is that the subjects of the animal tests (swine in this case) are not identical; thus, factors like body size, the location and dimension of the bile duct, and the response to the implantation may vary. These variations may materially affect the performance of the package, which must survive and protect the resonator in all conditions. Therefore, animal tests are necessary to evaluate the designs and identify the need for further improvements.

The expected outcomes from the animal tests are: (a) ability for the instrumented biliary stent to be delivered with a normal procedure and without significant concern from the endoscopist, (b) evidence that the implantation procedure and the implanted device do not affect the health of the animal, (c) ability to measure the initial sensor signal (baseline) once the stent has been implanted, (d) the reduction of the resonant frequency and quality factor of the sensor with time if there is any accumulation of biliary sludge, (e) comparison of the output of the sensor to transabdominal ultrasound imaging, and (f) evidence that the interrogation system for detecting the signal has clinical utility and is robust.

In this chapter, the protocol of the animal test procedures – including preparation of the animal, the procedure for implanting the biliary stent, and post-operative methods – is described. The results of a previous animal test with a magnetoelastic-sensor-integrated biliary stent are reviewed [Gre13]. Results of two animal tests of the magnetoelastic sensors protected by the two types of encapsulation approaches (Type F and Type S packages) described in Chapter 3 are then presented.

4.2. Animal Test Protocol

In each animal test, a female domestic swine is the subject of the implantation procedures described here. The swine is sedated first and then pre-operative analgesia is administered through an intravenous catheter, which is placed into an accessible vein on ear. After that, the swine is intubated and placed on isoflurane anesthesia, monitoring equipment (including temperature monitor, pulse oximetry, and electrocardiogram), and a heat source (electrically-heated table or water-circulated heating pad). The biliary stent is implanted in the bile duct by a standard endoscopic procedure. The endoscope (Olympus TJF Type Q180V side-viewing duodenoscope), which is shown in Fig. 3.2, is guided through the mouth and esophagus of the swine, to the stomach, and finally to the duodenum. The camera at the end of the endoscope helps to locate the position of the biliary orifice. Saline is injected through the endoscope to clear the camera view as necessary. Once the biliary orifice is located, a guidewire is placed through the orifice, and a radiographic dye is injected through a catheter into the bile duct. The dye allows the internal structures to be observed with an X-ray (fluoroscope) to confirm the cannulation of the bile duct and estimate its length. The introducer assembly, along with the loaded stent, is then loaded onto the back end of the guidewire and fed through the endoscope. Once the proximal end of the stent is aimed at the biliary orifice, the introducer assembly is used to push the stent into the bile duct. The flaps on the stent are intended to hold the stent in the desired position in the bile duct.

After proper stent position has been confirmed and while the animal is still sedated, transabdominal ultrasound is performed to visualize the biliary tree and confirm the position of the stent. This imaging uses a convex transducer in brightness mode and ultrasound gel as an acoustic coupling medium. Images from the ultrasound system are recorded, and used when possible to estimate the position of the stent. Blood is sampled from the ear vein, then used in full blood chemistry tests. These tests can provide evidence of liver malfunction and systemic toxicity effects as a result of the implanted device. About 10-20 cc of blood is collected at each sampling cycle, once per week.

After the stent implantation, the swine is fed twice a day and monitored daily by the veterinary technicians and co-investigators. Four sensor interrogation sessions are held – one per week – in the 28 days following stent implantation. For these sessions, the swine is sedated and anesthetized. Ultrasound and/or radiographic imaging is performed to confirm the position of the stent. At the end of the study, the animal is euthanized and the stent retrieved for further examination. The main equipment used in the animal tests is listed in Table 4.1. As the author gratefully acknowledges, the faculty and staff assisting with the animal tests are listed in Table 4.2.

Table 4.1: List of equipment used in an animal test.

#	Equipment Name
1	Temperature Monitor
2	Pulse Oximeter
3	Electrocardiogram
4	Heated Surgical Table
5	Intravenous Catheter
6	Olympus Camera Processor and Monitor
7	Endotracheal Tube
8	X-Ray System (Fluoroscopic “C-arm”)
9	Ultrasound System (Phillips Medical Systems Pediatric)
10	Side-Viewing Endoscope (Olympus TJF Type Q180V)
11	Standard Guidewires and Introducers (Cook Medical)
12	Isoflurane Control and Delivery System

Table 4.2: List of faculty and staff involved in the animal tests and their roles.

Name	Responsibility
Dr. Richard Kwon	Deliver stent endoscopically; provide collaborative guidance and animal test expertise.
Dr. Grace Elta	Provide collaborative guidance and animal test expertise.
Amber Yanovich	Handle the animal, anesthesia, fluoroscopy, and recovery.
Gail Rising	
Dr. Bob Sigler	Manage post-operative care and assist with necropsy.
Luaren Krueger	
Jiajie Xu	
Rafael Ramirez	Operate the fluoroscope system.
Dr. Patrick Lester	Manage the veterinary technician staff.
Scot Pittman	Manage the animal husbandry staff.
ULAM Husbandry and Veterinary Technician Staff	Feed, clean, and monitor the animal every day.

4.3. Previous Animal Test Results

A previous animal test, which utilized an otherwise unprotected magnetoelastic resonator array integrated with a 10 Fr biliary stent, informed the package design and animal testing approach for this work and thus is reviewed here. Fig. 4.1 [Gre13] shows the fluoroscopic image of an implanted 10 Fr plastic biliary stent in a female domestic swine. After a housing period of 4 weeks, the animal showed no ill effects and its weight increased from 29 kg to 42 kg. No signal was detected in the period. Finally, the animal was euthanized and the stent was retrieved and evaluated, as shown in Fig. 4.2. The stent was filled with bile but no sludge buildup was observed. After cutting the stent apart, the resonators were inspected and found to be damaged. It is believed that passing the introducer through the stent during the implantation preparation stage resulted in this damage.

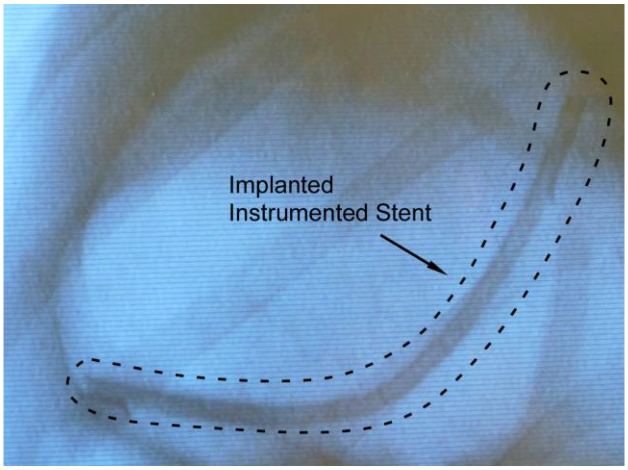

Fig. 4.1: Fluoroscopic image of an implanted 10 Fr plastic biliary stent [Gre13].

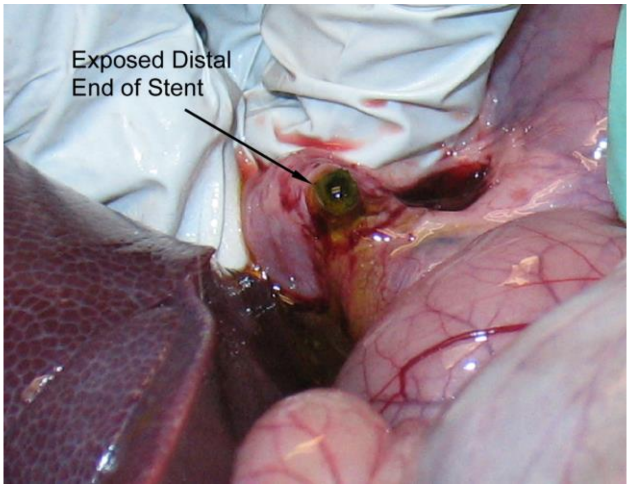

Fig. 4.2: Post-necropsy image of distal end of the stent [Gre13].

4.4. *In Vivo* Evaluation of the Type F Package

The animal test initiated on Day 1 used an 11.5 Fr x 7 cm Cotton-Leung plastic biliary stent (Cook Group, IN, USA) instrumented with the resonator, magnets, and the Type F package described in Chapter 3. This stent was implanted endoscopically in the bile duct of a 20.2 kg female domestic swine. The fluoroscopic picture after the implantation is shown in Fig. 4.3. After implantation, the biliary stent was found to be held in a convex curvature with a radius of 5 cm via the natural anatomy of the bile duct. This was a much tighter curvature than expected. No signal was detected in that situation.

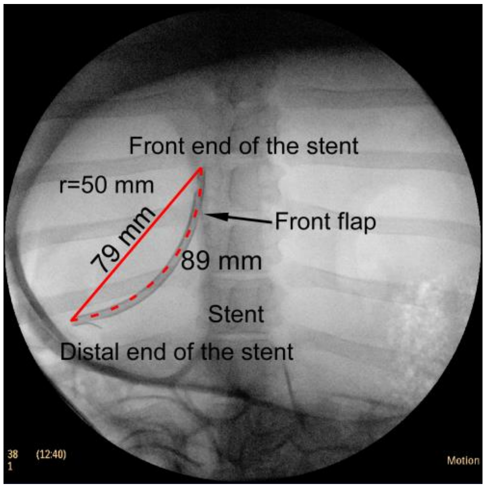

Fig. 4.3: Ventral-dorsal fluoroscopic picture after endoscopic implantation (Day 1). The radius of curvature of the stent in the bile duct is approximately 5 cm.

In the following two testing sessions (Day 7 and Day 14), the animal was 22 kg in weight. No signal could be obtained from the sensor. Transabdominal ultrasound imaging was performed to try to confirm the position of the stent. The ultrasound equipment was from Phillips Medical Systems Pediatric and the technique used a convex transducer (3.3 MHz) in brightness mode and ultrasound gel as an acoustic coupling medium, while the animal was sedated. Figure 4.4 shows the image of the transabdominal ultrasound results. According to the ultrasound technician, the dark triangular-shaped "blob" at the bottom of the ultrasound image could be the shadow due to the presence of the stent, but the actual position of the stent could not be ascertained using this imaging technique. To confirm the location of the stent, radiography was used. The orientation and the position of the stent changed greatly over the course of the survival period, as shown in the radiographs of Fig. 4.5 and Fig. 4.6. This phenomenon implied that the biliary stent had migrated outside the bile duct and might be in the colon and surrounded by fecal matter. In order to recover the stent before it was excreted by the animal, the animal was euthanized and eventually the stent was located in the colon, covered in (and full of) fecal matter, as shown in Fig. 4.7 and Fig. 4.8.

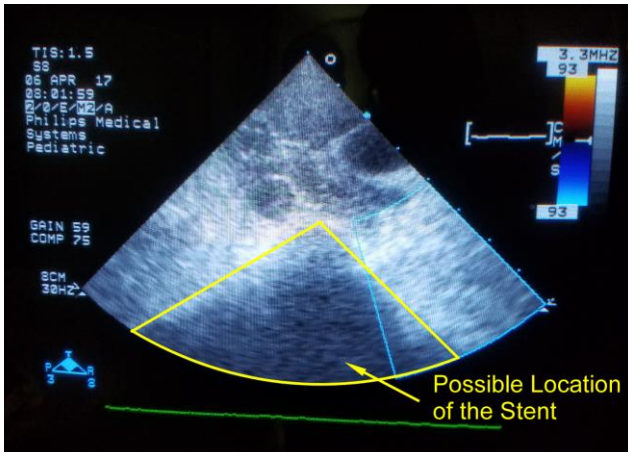

Fig. 4.4: Transabdominal ultrasound image using the equipment from Phillips Medical Systems with a 3.3 MHz linear probe. The dark triangular-shaped “blob” at the bottom of the ultrasound image might be the shadow due to the presence of the stent but the actual position of the stent could not be observed with this technique.

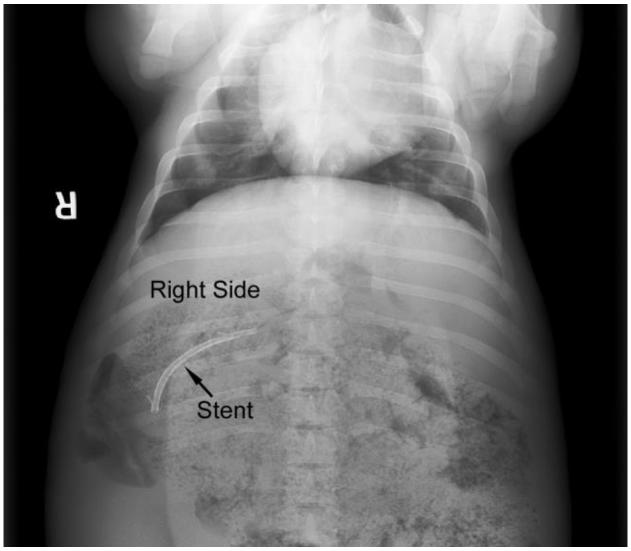

Fig. 4.5: Ventral-dorsal radiograph picture (Day 7). The orientation of the stent has changed greatly over the week.

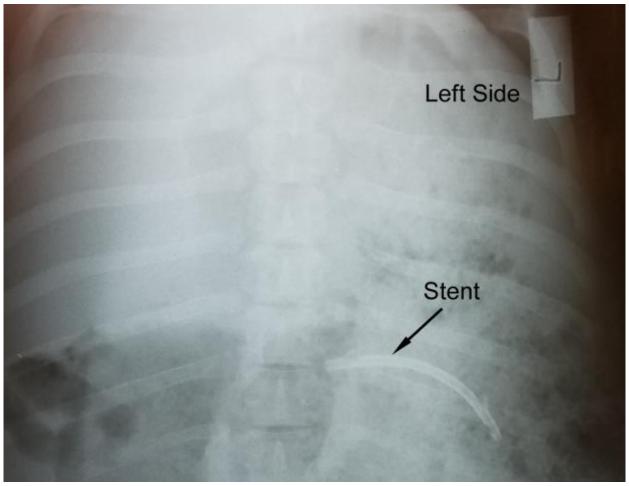

Fig. 4.6: Ventral-dorsal radiograph picture (Day 14). The position and orientation of the stent has again changed greatly over the week.

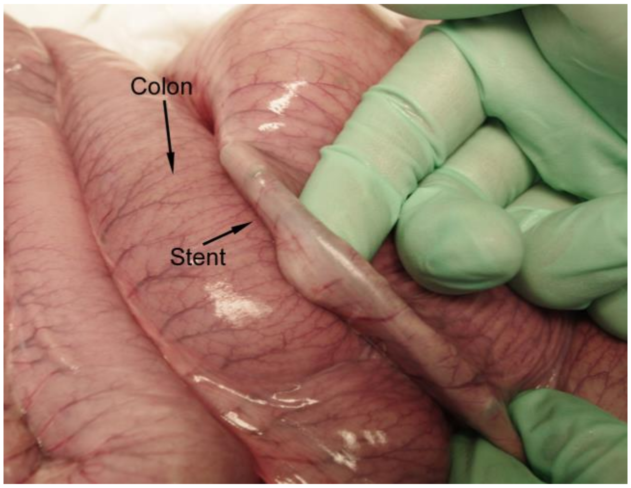

Fig. 4.7: The biliary stent was found in the colon of the animal.

Fig. 4.8: The excised stent was blackened and full of fecal matter.

The retrieved stent was flushed by hot water and soap to clean, but signal could still not be measured. When the stent was sliced and examined under the microscope, a crack at the middle of the package was observed, as shown in Fig. 4.9. Again, no signal was detected after slicing the stent. However, after removing the middle tethers and bending the stent for several times, a weak signal was measured. After the package was completely removed from the stent and cleaned, it was observed to have a convex curvature while the sensor and the magnets were still in the package, as shown in Fig. 4.10 and Fig. 4.11. In this case, a signal very near the original level (prior to implantation) was detected. Finally, the sensor was removed from the package and cleaned. The sensor was straight, no mechanical deformation was observed and the original signal (prior to packaging, with the sensor biased by DC electromagnetic coils) was measured, as shown in Fig. 4.12.

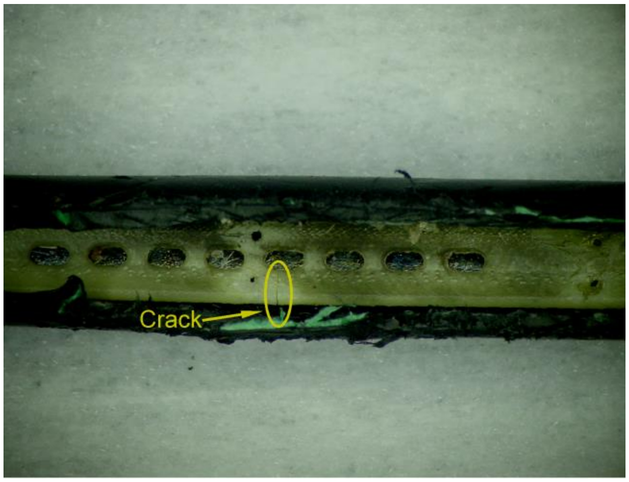

Fig. 4.9: The stent was sliced to examine under the microscope. A small crack was observed near the middle of the package.

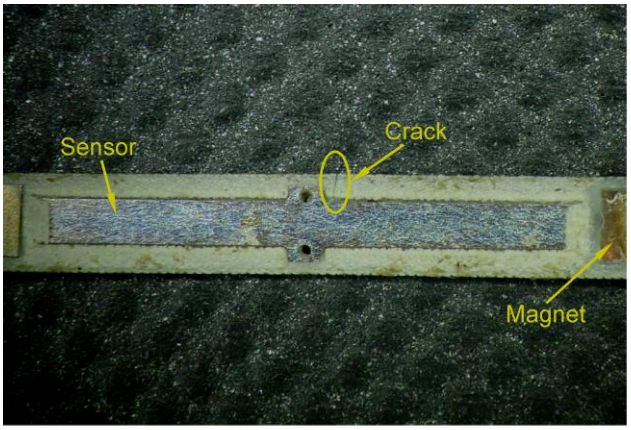

Fig. 4.10: The backside of the package under the microscope. The sensor and the magnets were still in the package.

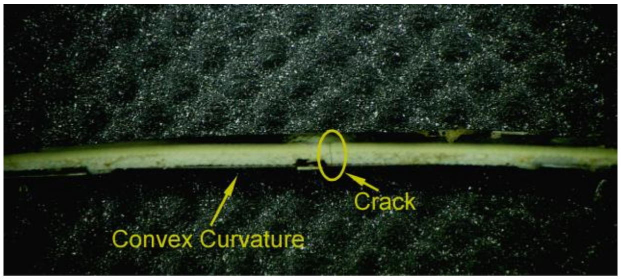

Fig. 4.11: The convex curvature of the package was observed under the microscope.

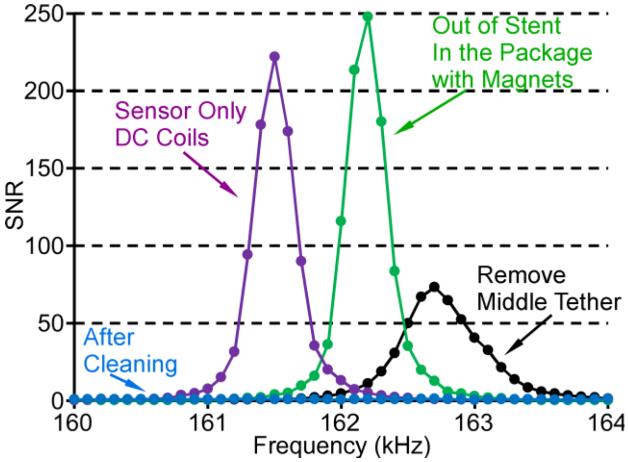

Fig. 4.12: Signal response of the sensor in each investigation stage.

The test results showed that the package could protect the magnetoelastic sensor from being damaged by the introducer and during the implantation. This also showed that the aluminum oxide coating protected the sensor and magnets from visible and performance degrading corrosion over the course of two weeks. However, the curvature of the package in the anatomical structure of the bile duct along with anchor loss through the middle tethers could have potentially prevented the sensor from vibrating normally and from providing a response measurable outside the animal.

4.5. *In situ* Evaluation of Type F Package

A resonator and magnets in a Type F package, integrated with an 11.5 Fr x 7 cm Cotton-Leung biliary stent (Cook Group, IN, USA), was also tested in an *in situ* experiment in the bile duct of a 22 kg female domestic swine carcass. The cross-section of the swine abdomen was ellipsoid, with a long diameter of 23 cm and a short diameter of 17.6 cm, when the swine was laid supine. Fig. 4.13 (a) shows the schematic of the experimental setup – the transmit coils (red) and receive coil (blue) wrapped around a swine. Fig. 4.13 (b) is a photograph of the coils in position around a swine carcass, along with a schematic showing the ellipsoid cross-section of the abdomen. The swine carcass was incised and an instrumented stent was inserted manually into the bile duct. Bile solution, harvested from the gallbladder of the carcass, was injected into the bile duct and stent. Internal organs were repositioned, and the incision temporarily closed with metal clamps.

The signal from this sensor measured *in situ* in the bile duct of a swine carcass is shown in Fig. 4.13 (c). The benchtop experimental result of a typical sensor encapsulated by the Type F package has a quality factor of 615, SNR of 103, and resonant frequency of 162 kHz in air, as also shown in Fig. 4.13 (c). The *in situ* response demonstrated a reduction in quality factor to 397, SNR to 76, and resonant frequency to 159 kHz. Both of these shifts were due to the immersion of the encapsulated sensor in bile. The wireless range for both benchtop and *in situ* measurements was ~10 cm.

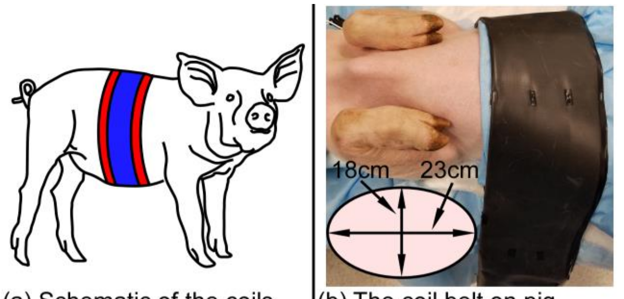

(a) Schematic of the coils (b) The coil belt on pig

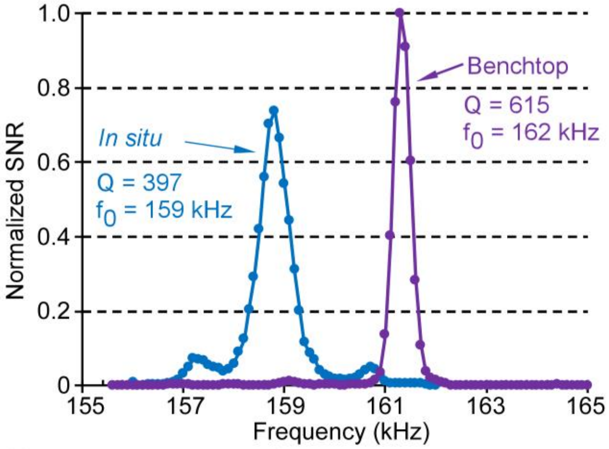

(c) Frequency response of a typical sensor in *in situ* test

Fig. 4.13: (a) Schematic of the transmit coils and receive coil wrapping around the swine as a "belt". (b) The coil belt around a swine carcass and measurements of the ellipsoid cross-section of the abdomen. (c) Frequency responses of a magnetoelastic sensor in a Type F package measured during a benchtop experiment (in air) and measured *in situ* in the bile duct of a swine carcass (immersed in a mixture of bile and other biological fluids).

4.6. *In Vivo* Evaluation of the Type S Package

The animal test initiated on Day 1 used a 10 Fr plastic Cotton-Leung biliary stent (Cook Group, IN, USA) integrated with the resonator, magnetic cuff, and the Type S package described in Chapter 3. The stent was implanted in the bile duct of a 27.7 kg female domestic swine by using a similar endoscopic procedure described previously. In this case, a key difference was that the elevator of the endoscope was lowered when pushing the stent into the bile duct, in order to better allow the stiff package to traverse the endoscopic channel. However, this difference did not impede the doctor to implant the stent during the surgery. The radiograph of the endoscope orientation upon fluoroscopic confirmation of the bile duct anatomy is shown in Fig. 4.14. The radiograph of the stent after the implantation is shown in Fig. 4.15. The “bright” component near the distal end of the stent was the magnetic cuff, which appeared to be straight according to the radiograph image. The approximate location of the package is also marked in the figure. Due to the location of the package in the distal end of the stent, and the anatomy of the bile duct for this specimen, the longitudinal direction of the package and the sensor was almost perpendicular to the long axis of the swine. The belt coil configuration loses significant sensitivity with this relative orientation of the sensor.

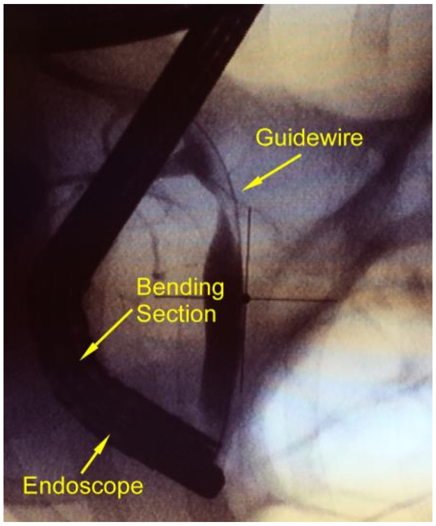

Fig. 4.14: Radiograph of the endoscope and guidewire before the implantation of the stent. The guidewire is in the bile duct. The approximate radius of curvature of the bending section is 2.02 cm.

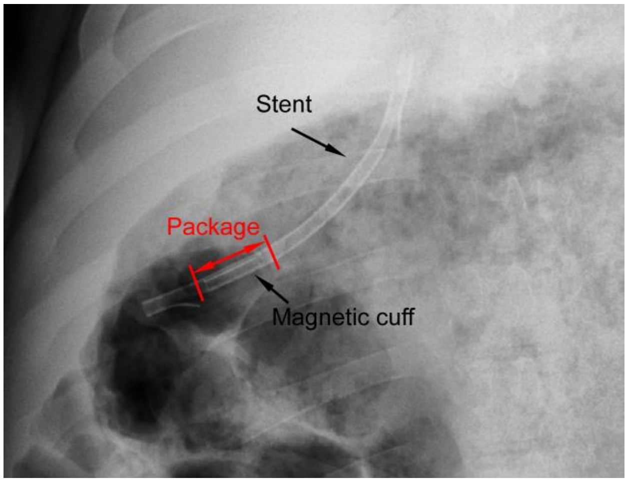

Fig. 4.15: The right ventral radiograph of the stent after implantation. The magnetic cuff appears to be straight after placement based on the radiograph. The package is located near the distal end of the stent and its direction is almost perpendicular to the long axis of the swine.

The swine was found to be presenting with symptoms of abdominal pain one day after the implantation (Day 2). Analgesia was administered, but the symptoms did not abate, and the animal expired the same day. The necropsy procedure was performed on the next day. No obvious perforation or bleeding was found during the process, although the presence of expansive peritoneal fibrosis indicated the onset of serositis.

The stent was found in the bile duct and it had migrated distally from the biliary orifice by approximately 1.5 cm, as shown in Fig. 4.16. The distal end of the stent was fully occluded. The inset of Fig. 4.16 shows the full retrieved stent. The stent near the location of the package was permanently deformed in a curved shape. No signal was measured from the stent.

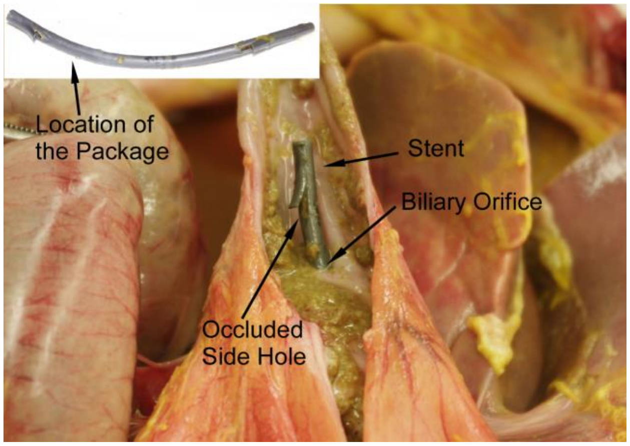

Fig. 4.16: The instrumented biliary stent was found in the bile duct. It had migrated from the biliary orifice by approximately 1.5 cm. The distal end of the stent is fully occluded with partially digested food. The inset shows the full retrieved stent. The stent near the location of the package is curved.

The stent and packaged sensor was examined further after explantation. No signal was measured after the stent was further cleaned and straightened. Therefore, the stent was sliced open, completely cleaned, and observed under the microscope. The package was found to have a curvature along the width axis of the package, as shown in Fig. 4.17 (a). The magnetic cuff was also found to have a curvature in the same direction and the bonded sensors were delaminated after further cleaning, as shown in Fig. 4.17 (b) and (c). The bending curvature was formed possibly when passing the stent through the bending section of the endoscope (Fig. 4.14), which has a minimum radius of curvature of 2.02 cm, and the plastic deformation of the package and the magnet added additional stress along the width of the bonded sensor and caused it to delaminate.

(a) Type S Package removed from the stent

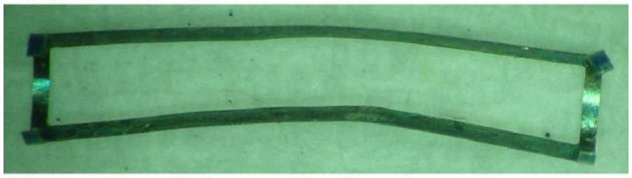

(b) Magnetic cuff disassembled from the package

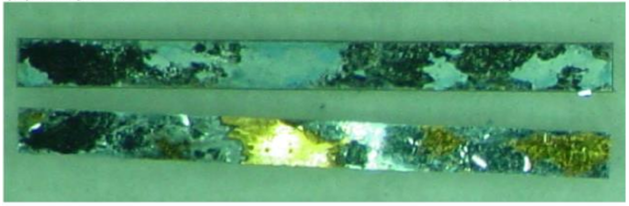

(c) Bonded sensor is delaminated after cleaning

Fig. 4.17: (a) The Type S package has a bending curvature along the width axis of the package. (b) The disassembled magnetic cuff has the same bending curvature. (c) The bonded sensor was found to be delaminated after taking out of the package and cleaning.

4.7. Conclusion

The magnetoelastic resonators were encapsulated in the two types of 3D printed packages (Type F and Type S) and then assembled in commercial plastic biliary stents for animal implantation. The Type F package could protect the resonator from being damaged from the introducer and was elastic and flexible enough for passing through the endoscopic channel (even with the elevator raised) and into the bile duct. However, the curvature of the bile duct kept the Type F package and the sensor inside in a curved state, and no signal was detected when the sensor was in the bile duct. After retrieving the stent showed that the curved package with the middle wires was the main reason of the attenuation of the sensor signal.

The Type S package, on the other hand, was designed to be short and stiff. The *in vivo* test demonstrated that it could also prevent damage from the introducer. Although benchtop experiments showed that the package was able to pass through the endoscope (with the elevator lowered), the endoscopic delivery during the *in vivo* test resulted in plastic deformation of the package. It was highly possible that the package was plastically deformed when it passed through the tight bend of the endoscope shown in Fig. 4.14.

Overall, the packages are adequate for protecting the encapsulated sensors from being damaged by the introducer but are still inadequate for maintaining a straight sensor after implantation or for being delivered smoothly. Additionally, the interrogation coils oriented around the abdomen of the swine are not sensitive to the magnetoelastic sensor that is encapsulated in the Type S package – due to the mostly radial orientation of the portion of the stent containing the resonator after implantation. Therefore, potential improvements should include the miniaturization of the sensor, allowing a shorter package less impactful on the overall flexibility of the stent. Customized coil geometries that can accommodate non-axial sensor orientations may also be necessary. Another important discovery of these animal tests is the insufficiency of using ultrasound imaging to estimate the position of the bile duct and the biliary stent, and certainly to visualize within the stent. As such, radiographic imaging is necessary to confirm the position of the biliary stent.

Chapter 5: Miniaturized Mass-Loaded Self-Biased Magnetoelastic Sensor

Based on the experience mentioned in Chapter 3 and 4, reducing the package size can reduce the impact on the stent and increase the overall flexibility of the stent. One method to allow reduction of the size of the package is to miniaturize the resonator itself. In this vein, this chapter proposes an improved resonator design, specifically targeting miniaturization while maintaining a low resonant frequency. Miniaturization is desirable for a medical implant in general due to the advantages of smaller form factor, lower profile and less disruption of normal biological functions. Specifically, in the application of the sensing of biliary sludge accumulation, the miniaturization of the resonator can decrease the sensitivity of the resonator to the curvature of the bile duct/biliary stent, and reduce the length of the stent that must be kept straight after delivery. This results in a reduced impact to the overall flexibility of the stent. The low resonant frequency has the benefits of lower attenuation as the magnetic signals pass through conductive materials (human tissue, for example), less transmit coil impedance and thus the ability to deliver more input current and a larger input magnetic field, and a larger time constant (for a given quality factor) which aids in capturing more energy during the ringdown receive period.

First, scaling effects for simple ribbon resonators are examined with finite element analysis and experimentally. This study indicates that miniaturizing by simply reducing the sensor length (and thus increasing the resonant frequency) has substantial impact on the size of the received signal. As such, a new concept for miniaturizing the sensor while maintaining the resonant frequency is presented, followed by analytical and numerical design of the new concept. The fabrication and experimental performance of the new concept is then demonstrated.

5.1. Scaling of Ribbon Sensors

Ribbon-shaped magnetoelastic sensors with various lengths were simulated in COMSOL. The width and thickness of the sensors were fixed to be 1 mm and 60 μm, respectively, while the lengths of the sensors were 12.5 mm, 9.375 mm, and 6.25 mm. The quality factors of all the sensors were set to be 600 by setting the equivalent mass loading $\alpha_m = \omega_r/Q$ in the Rayleigh damping model, where ω_r is the resonant frequency and Q is the quality factor [Pep15]. The simulated coil was 5 mm in radius and 30 mm in length, and the surface current density was 22.29 A/m (directed azimuthally around the coil) to generate an input magnetic flux density of 0.28 G along the longitudinal axis of the coil. The signal amplitude was calculated with Faraday's law of induction, by first evaluating the volume integration of the rate of change of the magnetic flux density in the axial direction of the coil and sensor at resonance, then subtracting the value calculated in the same manner without the presence of a sensor. This process, in effect, cancelled the large transmitted signal from manifesting in the response signal.

The calculated resonant frequencies, tip displacements, and signal amplitudes are listed in

Table 5.1. The simulation results show that the resonant frequency of the sensor is inversely proportional to the sensor length, which matches the classical beam theory for the longitudinal vibration mode. The signal amplitude of the sensor reduces proportionally with the decreasing length (reducing the sensor length by half reduces the signal amplitude by 62%).

Table 5.1: COMSOL simulation result of the magnetoelastic ribbon sensors of different lengths with the same width (1 mm), same thickness (60 μm), and similar quality factor (~600).

Sensor Length (mm)	Resonant Frequency (kHz)	Tip Displacement (nm)	Signal Amplitude ($x10^{-4}$ Vm/turn)
12.5	165.75	850	1.95
9.375	221.95	425	1.23
6.25	334.40	202	0.74

The fabricated double-layer magnetoelastic sensors with the same dimensions as those modeled (two samples for each case) were also tested experimentally by using the same interrogation system described in section 3.4.2 except that a coil set of 30 mm in diameter and 10 mm in length (10 turns in each of the transmit and receive coils) was used instead of the larger coil set. The LNA was set to an amplification factor of 20 μA/V, and no bandpass filter was applied on the LNA. The DC magnetic field generated by the Helmholtz coils were tuned to the optimal magnetic bias for the highest SNR. Due to the different resonant frequencies of each sensor length, the impedance of the transmit coil varied for each length. Therefore, the current through the transmit coil was monitored by a current meter and kept the same for each by changing the input voltage. By normalizing the input peak-to-peak current to be 43 mA in this case, the induced magnetic flux density was kept the same (approximated as 54 μT in air). The DC resistance of the receive coil was measured to be 2 Ω and the inductance was calculated to be 9 μH by measuring the AC impedance. Therefore, the impedance of the receiving system was mainly dependent on resistance (including the resistance of the logic switch, protection circuit, and LNA, which contributed a total of approximately 350 Ω). Hence, the sensitivity of the receiving system was proportional to the frequency: $\partial I_{in}/\partial B \propto \omega/R$, or $\partial E_s/\partial B^2 \propto \omega$. The normalized values are also shown in Table 5.2.

The averaged test results from two samples of each sensor length are shown in Table 5.2. From the benchtop experiment results, the signal energy of 6.25 mm long sensor was only 6.4% of that of the 12.5 mm long sensor.

Table 5.2: Benchtop experiment results of the fabricated double-layer magnetoelastic ribbon sensors of different lengths with the same width (1 mm) and thickness (60 μm).

Sensor Length (mm)	Signal Energy (V^2)	Normalized Energy (%)	SNR ($x10^5$)	Resonant Frequency (kHz)	Quality Factor
12.5	0.717	100%	28.4	159.72	483.5
9.375	0.118	12%	2.9	214.35	431.4
6.25	0.046	3.2%	0.9	321.40	555.4

The normalized SNR and resonant frequency of the above three sensor types are also shown in Fig. 5.1. In addition, single-layer magnetoelastic sensors (28 μm thick) with two different widths (0.5 mm and 1 mm) were also fabricated and tested to plot a figure of a more general sensor scaling effect. In Fig. 5.1, circle, square, and triangle data points represent 12.5 mm, 9.375 mm, and 6.25 mm long sensors, respectively. Blue, red, green data points represent cross-section dimensions of 1 mm x 60 µm, 1 mm x 28 µm, and 0.5 mm x 28 µm, respectively. From the plot, the resonant frequency is inversely proportional to the sensor length and is not strongly related to the width or thickness, as expected. More importantly, the sensor signal tends to decrease rapidly when any sensor dimension is reduced. In all cases, the quality factors are around 250 to 700. Note that the optimal DC bias field was approximately 10 Oe, 10 Oe, and 23 Oe for the 12.5 mm, 9.375 mm, and 6.25 mm long sensors, respectively.

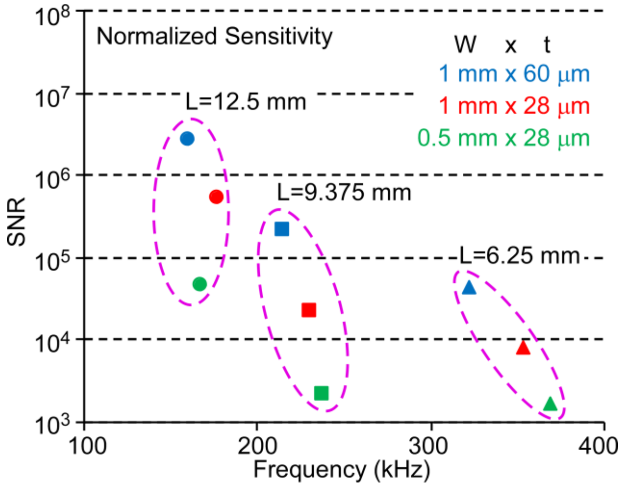

Fig. 5.1: Plot of the sensor scaling effect. Circle, square, and triangle data points represent 12.5 mm, 9.375 mm, and 6.25 mm long sensors, respectively. Blue, red, and green data points represent cross section dimension of 1 mm x 60 µm, 1 mm x 28 µm, and 0.5 mm x 28 µm, respectively. The sensitivity of the test circuit is normalized.

The presented simulation and experimental results of Tables 5.1 and 5.2 differ significantly, but for a reason that is related to the practical concerns of the experimental measurements. This reason is mainly related to the timing of the receiving period along with the signal processing used in LabVIEW. In the signal processing, the data before the time delay Δt is excluded due to the feedthrough from the transmit coil and the voltage spike when toggling on the amplification of the LNA. Squaring of the signal, followed by quadrature mixing and integration of the signal over the ringdown period (until the noise level A_n^2 is reached), also leads to major differences between the simulation results – which do not incorporate these effects – and the experimental results.

The effects on the captured response for sensors of various resonant frequencies due to the experimental measurement approach are further illustrated in Fig. 5.2. A shorter sensor with a smaller initial amplitude also has a shorter time constant if the quality factor is a constant, as shown in Fig. 5.2. Therefore, the shorter sensor loses a larger percentage of the signal/energy than the longer sensor due to the initial time delay and measurement noise level.

The integrated response of a sensor can be calculated by equation 5.1.1. For example, if the time delay $\Delta t = 240\ \mu\text{s}$, time constants $\tau_1 = 2\tau_2 = 1.19\ \text{ms}$, turns ratio is 1000, initial amplitudes $A_1 = 2.14 \times 10^{-4}\ \text{Vm/turn}$, $A_2 = 5.5 \times 10^{-5}\ \text{Vm/turn}$ (subscript 1 denotes a 12.5 mm long sensor, and subscript 2 denotes a 6.25 mm long sensor) and noise amplitude $A_n = 0$, then the energy ratio $E_1/E_2 = 45.32$. In these calculations the noise level is assumed to be 0 but its effect on the total received energy can become significant as the noise voltage approaches some significant portion of the initial voltage. The FEA results and the experimental results are compared in Table 5.3. The raw and adjusted energies of the FEA and experimental results are the relative values of the 12.5 mm long sensor in all cases. The effect of the time delay as described in Eq. (5.1.1) was considered in the reported "FEA adjusted energy".

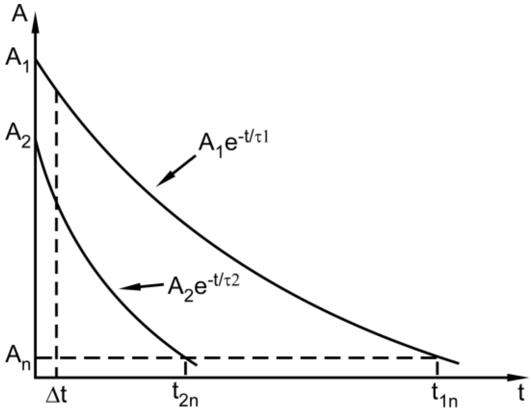

Fig. 5.2: Schematic of the ring down profiles of two magnetoelastic ribbon sensors with different lengths. The longer sensor has larger initial amplitude and decay time. Signal data before Δt and less than A_n are not measurable in the experiment.

$$E = \int_{\Delta t}^{t_n} \left(Ae^{-\frac{t}{\tau}}\right)^2 dt = \frac{1}{2}\tau\left(A^2 e^{-\frac{2\Delta t}{\tau}} - A_n^2\right) \tag{5.1.1}$$

Table 5.3: The resonant frequencies, quality factors, time constants, and relative signal energies of both FEA and experimental results are compared.

Sensor Length (mm)	12.5	9.375	6.25
FEA Resonant Frequency (kHz)	165.75	221.95	334.40
FEA Quality Factor	554	551	548
FEA Time Constant (ms)	1.15	0.86	0.57
FEA Raw Energy (%)	100%	30%	7.1%
FEA Adjusted Energy (%)	100%	17%	2.6%
Experimental Resonant Frequency (kHz)	159.72	214.35	321.40
Experimental Quality Factor	484	431	555
Experimental Time Constant (ms)	0.96	0.64	0.54
Experimental Measured Energy (%)	100%	12%	3.2%

5.2. Mass-Loaded Self-Biased Resonator Design

5.2.1. Concept

There are multiple methods to reduce the resonant frequency of a resonator. The most straightforward way is by simply increasing the length of the resonator, but this will also increase the size of the resonator. Another method is to reduce the stiffness of the resonator. This can be done, for instance, by adding perforations to the structure, as examined in prior work on magnetoelastic sensors [Gre09c]. This approach typically requires removing magnetoelastic material and introduces local areas of in-plane bending, both which can have a negative effect on the signal amplitude. Alternatively, the effective mass can be increased to lower the resonant frequency. This can be done by attaching mass strategically, which is a method examined in this work.

The concept for this approach has two magnets attached at the two ends of the magnetoelastic ribbon sensor, serving as mass loads (Fig. 5.3). The active portion of the sensor is only half of the length compared to the previous design but still maintains a similar resonant frequency. The magnets can also provide a DC magnetic bias which is required for a large amplitude response from the sensor.

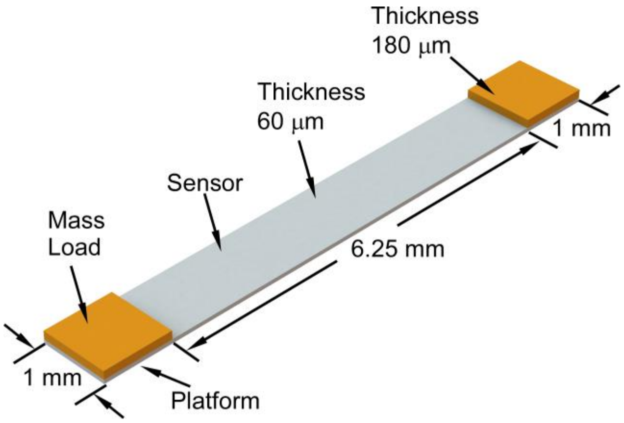

Fig. 5.3: Schematic of the mass-loaded sensor. The sensor is 6 mm long, 1 mm wide, and 60 μm thick. The mass loads have the geometry of 1 mm x 1 mm x 180 μm while that of the platforms underneath the mass loadings is 1 mm x 1 mm x 60 μm.

5.2.2. Analysis

The fundamental frequency ω_0 of longitudinal vibrations for a free-free beam with length L_0, Young's modulus E, and density of ρ_s is:

$$\omega_0 = \frac{\pi}{L_0}\sqrt{\frac{E}{\rho_s}}\ (rad/s) \tag{5.2.2.1}$$

while for a mass-loaded/mass-loaded beam with length L_1, cross-sectional area S and mass M (Fig. 5.4), the fundamental frequency ω_1 (see Appendix A for full derivation) is

$$\omega_1 L_1\sqrt{\frac{\rho_s}{E}} \cdot \tan\left(\frac{\omega_1 L_1}{2}\sqrt{\frac{\rho_s}{E}}\right) = \frac{S\rho_s L_1}{M}\ . \tag{5.2.2.2}$$

Let $L_1 = \frac{1}{2}L_0$. For the resonant frequency of the unloaded and loaded resonator to be equal, $\omega_1 = \omega_0$, and

$$M = \frac{2}{\pi}S\rho L_1 \tag{5.2.2.3}$$

This means with the proper mass loadings ($\frac{2}{\pi}$ times the original beam mass) at both ends, the beam can vibrate at the same frequency of the free-free structure but while only occupying half of the length.

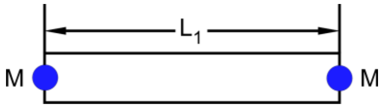

Fig. 5.4: Structure of a mass-loaded/mass-loaded beam. The beam length is L1 and has two point-mass M at the two ends.

Based on the analytical model, the structure of the mass-loaded sensor is established, as shown in Fig. 5.4. The sensor between the mass loads is 6.25 mm long, 1 mm wide, and 60 μm thick. The mass loads are 1 mm x 1 mm x 180 μm while the platforms underneath the mass loadings are 1 mm x 1 mm x 60 μm (i.e. the total thickness at the mass loads is 240 μm).

5.2.3. Finite Element Analysis - Magnetomechanical

The fully coupled magnetomechanical model was simulated in COMSOL [Pep15]. The mass loads were simulated as iron blocks and have the same mass density as the sensor (Metglas 2826MB). The simulated coil was 5 mm in diameter and 30 mm in length, and its surface current density was 22.29 A/m (directed in the azimuthal direction of the coil) to provide a 0.28 G AC magnetic flux density.

The simulation result, as shown in Fig. 5.5, indicates that the vibration mode of the sensors is at the resonant frequencies of 183 kHz and 167 kHz, with 120 μm and 180 μm mass thicknesses, respectively. Because the mass load having a center of mass above the neutral axis of the sensor, the sensor has a small amount of out-of-plane displacement even when vibrating in its fundamental longitudinal mode. The maximum displacement amplitude of the sensors at the tips along the longitudinal sensor axis are 317 nm and 210 nm, respectively. The simulated signal amplitudes of the sensors are 1.37 x 10^{-4} Vm/turn and 1.28 x 10^{-4} Vm/turn, respectively, which are around 70% of that of the 12.5 mm long ribbon sensor (49% of the signal energy of the 12.5 mm long ribbon sensor).

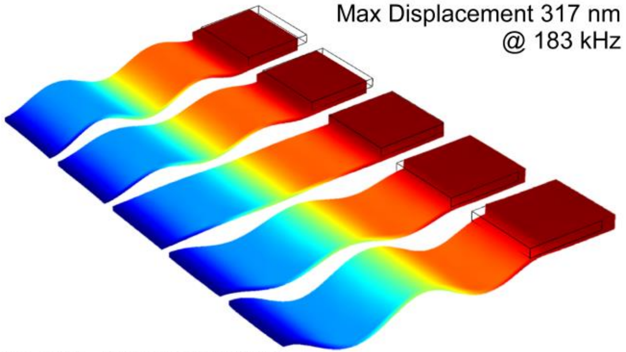

(a) 120 μm mass thickness

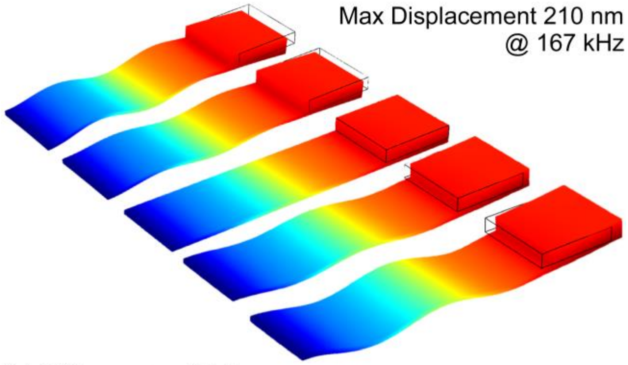

(b) 180 μm mass thickness

Fig. 5.5: COMSOL simulation result of the mass-loaded sensors with 120 μm and 180 μm mass thicknesses. The resonant frequencies are 183 kHz and 167 kHz, and the maximum displacements of the sensors at the tips along the longitudinal sensor axis are 317 nm and 210 nm, respectively.

5.2.4. Finite Element Analysis - Magnetic DC Bias

The mass loads in the sensor are intended to be permanent magnets to provide a DC magnetic field for biasing the sensor. To estimate the approximate DC magnetic flux density that could be generated in the resonator for such an architecture, finite element analysis in COMSOL was utilized. In the COMSOL simulations, the magnets have the thickness of 120 μm or 180 μm and are set to have a residual flux density of 0.9356 T (along the longitudinal axis of the resonator) and a relative permeability of 23. These are approximate values of Arnokrome 5 material, as will be used in the construction of the device. The non-linear magnetization saturation behavior of the magnetoelastic material was considered in the model by setting the sensor material B-H curve to have a saturation induction of 0.88 T at 14 A/m (50000 DC relative permeability). Modeling this behavior allows the model to avoid unrealistic shunting of the magnetic field through the highly permeable magnetoelastic material directly beneath the magnetic mass loads. The simulated magnetic flux density was found to be uniform in the sensor with values of 0.4 T and 0.65 T, for the 120 μm thick and 180 μm thick magnets, respectively, as shown in Fig. 5.6. Fig. 5.7 shows the simulated magnetic flux density magnitude and direction in the sensor and magnet. In comparison, the magnetic biasing structures described in Chapter 4 (magnetic strips and magnetic cuffs) were estimated to result in a magnetic flux density in the sensor of 0.4 T and 0.36 T, respectively, using this same analysis approach. This indicates that the magnet mass loads should provide sufficient DC bias to allow a significantly large sensor response.

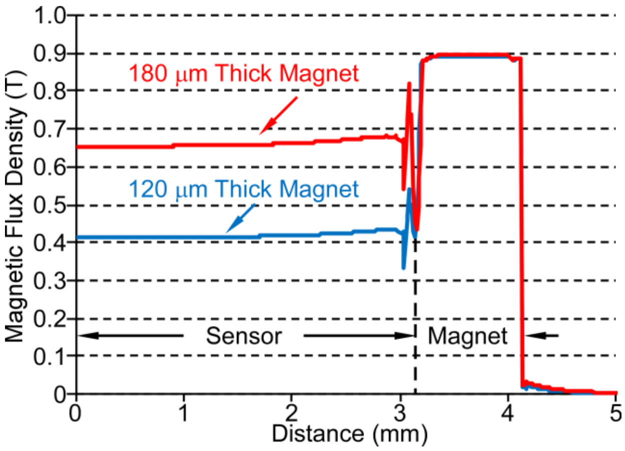

Fig. 5.6: COMSOL simulation result of the magnetic flux density in the sensor. The 0.4 T and 0.65 T flux densities provided by the 120 μm and 180 μm thick magnets, respectively, are proper biasing values for the magnetoelastic sensor.

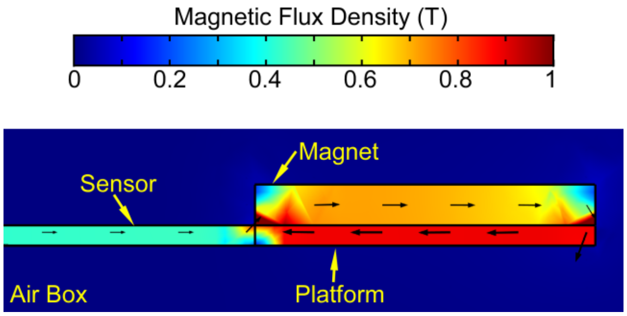

Fig. 5.7: COMSOL simulation result of the magnetic flux density in the sensor with the magnet thickness of 120 μm.

5.3. Sensor Fabrication and Signal Test

The materials of the sensor and the mass loads are Metglas 2826MB and Arnokrome 5, respectively. The two Metglas sheets and two Arnokrome sheets were bonded first, using the same Au-In eutectic bonding process and layer thicknesses described in section 3.3.2. After that, one surface of the bonded Metglas layers was electroplated by 6 µm gold. For the Arnokrome layers, a window feature was machined first utilizing EDM, and then one side of the Arnokrome was electroplated by 6 µm indium. The two layers were bonded together with the same AuIn eutectic bonding process. Finally, the sensors were EDMed from the bonded layers, as shown in Fig. 5.8. A typical sensor is shown in Fig. 5.9 and the inset shows a micrograph of the side view of the end of the sensor and the mass load. The total thickness of the bonded sensor portion was 68 µm while that of the bonded magnets and Metglas platform was 218 µm.

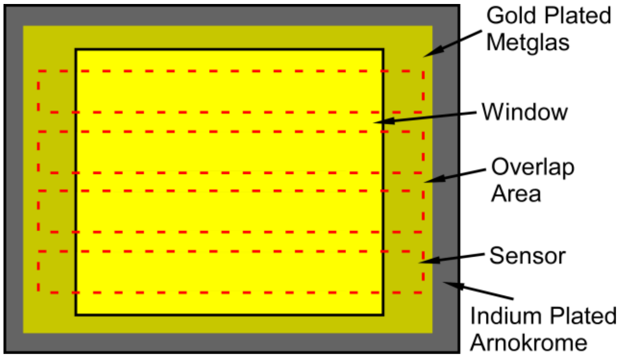

Fig. 5.8: Top view of the bonded Metglas and Arnokrome. The yellow component represents the bonded Metglas layers with one surface plated by gold. The grey component with the window opening represents the bonded Arnokrome layers with one surface plated by indium. The two materials were bonded together (the dark yellow area is the overlap area) and the sensors were EDMed along the red dashed lines.

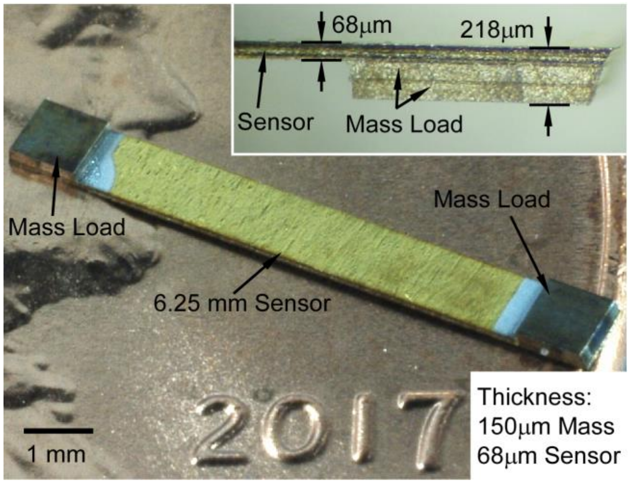

Fig. 5.9: A typical mass loaded sensor and the enlarged sideview of the sensor at the mass load.

Two mass-loaded sensors were fabricated and first tested in Helmholtz coils to find the largest signal at the optimal bias point. The average resonant frequency, signal energy, SNR, and the quality factor are 172.03 kHz, 0.007 V^2, 18280, and 296, respectively, when the biasing field was 10 Oe (provided by Helmholtz coils). The magnets were then magnetized using an impulse magnetizer (10 kG peak magnetic flux density). The self-biased sensors were tested in the 30 mm diameter small coil set. Bandpass filtering was not engaged on the LNA. The peak input current during the transmit period was set to 43 mA. The average resonant frequency, signal energy, SNR, and the quality factor are 173.6 kHz, 0.006 V^2, 13888, and 385, respectively. Fig. 5.10 shows the frequency response of a typical sensor that is biased by Helmholtz coils and by magnets, respectively. Therefore, the self-biased magnets can provide a near-optimal DC magnetic bias for the sensor.

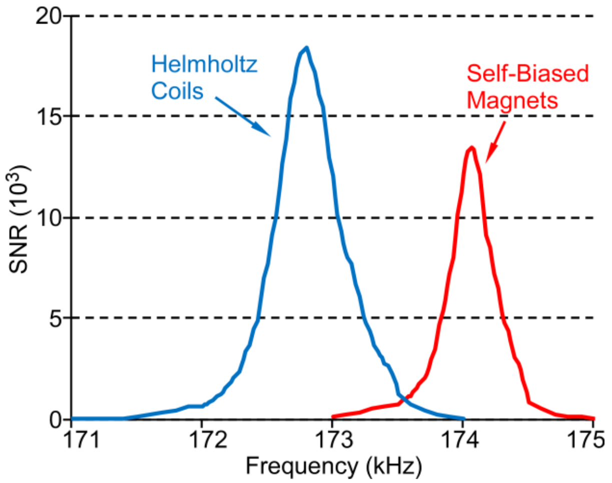

Fig. 5.10: Experimentally measured frequency responses of a typical mass-loaded sensor by Helmholtz coils and by integrated magnets. In the red curve, the magnets are magnetized to provide the DC magnetic bias for the sensor.

Comparing this signal test result with the sensor scaling effect plot in Fig. 5.1, the mass-loaded sensor had a similar level of SNR to that of the 6.25 mm long, 1 mm wide, and 60 µm thick ribbon sensor but its resonant frequency was similar to that of a 12.5 mm long ribbon sensor and still maintained a fairly high quality factor. However, although the frequency is about the same as a 12.5 mm long ribbon sensor – as expected from FEA simulations – the measured signal energy is only 12% of a typical 12.5 mm long ribbon sensor, instead of the 49% expected from the FEA simulations. This is most likely due to fabrication process shortcomings, including a weak or non-uniform bond between the Metglas layers.

5.4. Conclusions

The scaling effect of the magnetoelastic sensor with the simple ribbon geometry was analyzed by numerical modeling, FEA simulations, and testing results. The analytical equations indicated that the resonant frequency of the sensor is inversely proportional to the sensor length and did not depend on the width or thickness, which was also demonstrated by simulation and experimental results. As sensor length is varied, the trends indicated for signal amplitude by the bare simulation results and the experimental results were similar but differed in magnitude. Once the practical effects of time delay in the signal processing procedure and the environmental noise level were applied to the simulated results, the magnitude of the trends with sensor length variation matched more closely. This scaling study indicated that removing sensor material – from the length, width, or thickness – was likely to have significant effects on measurable signal strength.

The animal tests in Chapter 4 indicated that a miniaturized sensor, with accordant reduced impact on stent flexibility and elastic recovery, would be beneficial for this application. In order to reduce the total size of the sensor but still maintain a low resonant frequency (less attenuation when the magnetic signal passes through conductive layers), a mass-loaded sensor was conceived, designed, simulated, fabricated, and tested. The total length of the sensor was 8.25 mm while the largest thickness was 218 μm. The resonant frequency of the sensor was 173.6 kHz. The magnets at the two ends of the resonator serve as mass loads – keeping the resonant frequency low – while also providing a DC magnetic bias for the sensor. Compared to the geometries and locations of the magnets used in the Type F and Type S packages, the geometry of this new self-biased sensor could reduce the total length of the package by up to 60%. Therefore, the impact of the package on the stent can be reduced and the overall flexibility of the instrumented stent should be closer to that of a standard stent.

Chapter 6: Conclusions and Future Work

This chapter summarizes and draws conclusions from the efforts thus far to design the polymeric packaging of miniaturized magnetoelastic resonators for environmental and biomedical sensing applications. Major contributions of each research effort in the context of the broader field of knowledge are summarized. Future work to further improve the designs of the packaging for the miniaturized magnetoelastic resonators used in both applications is proposed.

6.1. Summary of this Work

The first three-dimensional polymeric packaging of the magnetoelastic resonators is for tagging applications in small tubes and piping systems which may have high temperature (≥ 150°C), high pressure (≥ 10.1 MPa), and highly corrosive fluids. This work represents the first reported use of the material of the package, liquid crystal polymer (LCP), in encapsulation of magnetoelastic resonators for tagging applications. The final size of the fabricated package is only 7.7 mm^3 but can provide a large shear failure force of 61.1 N and can endure pressure up to 2000 psi (≈13.8 MPa). The features in the package allow the resonator suspension to perform its function, resulting in less friction between the package and active portion of the resonator and thus maintaining a larger signal. This work shows that the LCP is a promising thermoformable packaging material for miniaturized magnetoelastic resonators due to its excellent electrical, mechanical, thermal, and chemical properties. In addition, the costs of processing LCP with thermoforming are potentially lower than those for other materials and for microinjection molding.

The second context for magnetoelastic encapsulation studied in this work is the polymeric packaging designed for protecting the biomedical implantable magnetoelastic resonators in commercial biliary stents. In this case, the resonators are not used for tagging, but to sense the accumulated biliary sludge in the stents. The primary function of the package is to prevent the resonators from being damaged by the introducer. However, the package must also be biocompatible and chemically inert at body temperature, be able to pass through the complex delivery path and within the limited size of the stent, and allow fluidic connection between the resonator and the interior contents of the stent. These constraints must all be met without impeding the ability of the doctor to endoscopically implant the stent. The additional package should still maintain a large open flow path of the stent. In this work, these functional goals are achieved by designing millimeter-scale packages with features such as a housing cavity, perforations, tapered and smooth edges; these features are realized by utilizing a 3D printing process. The effect of package flexibility on the ability to deliver the instrumented stent while protecting the resonator is evaluated.

Two types of packages (Type F and Type S) are designed, fabricated, and evaluated. The key advantage of the Type F package is the flexibility of the package during the delivery process while that of the Type S package is to maintain a strong signal even when the stent is in a curved bile duct. The material of the packages is M3 crystal and the packages are fabricated by 3D printing technology. The length, width, and maximum thickness of the Type F package are 26.4 mm, 2.3 mm and 0.53 mm, respectively. For the Type S package with an outer diameter of 2.54 mm, the length and maximum thickness are 15 mm and 0.74 mm, respectively. The major contributions of the work are that the designs of the packages provided potential solutions for two extreme mechanical conditions that may occur in the endoscopic implantations and the designs of the miniaturized sensors and integrated magnets reduce the total size of the device as well as provide a more stable signal response.

The two types of packages mentioned above were both tested *in vivo*. Although no signal was detected in either case, a lot of efforts and observations are worth to report. The Type F package can protect the resonator from being damaged by the introducer and was elastic and flexible enough for passing through the endoscopic channel (even with the elevator raised) and into the bile duct. However, if the bile duct is curved, it will keep the Type F package and the sensor inside in a curved state and no signal can be detected. The Type S package can also prevent damage from the introducer but it is still too long to pass through the endoscope channel with being deformed. Another important conclusion from these animal tests is the insufficiency of using ultrasound imaging to estimate the position of the bile duct and the biliary stent, and certainly to visualize within the stent. As such, radiographic imaging is necessary to confirm the position of the biliary stent.

Finally, a design of the miniaturization of the magnetoelastic with self-biased magnets is introduced. The design reduces the sensor length but still maintain a low resonant frequency.

The total length of the sensor was 8.25 mm while the largest thickness was 218 μm. The resonant frequency of the sensor was 173.6 kHz. The magnets at the two ends of the resonator serve as mass loads – keeping the resonant frequency low – while also providing a DC magnetic bias for the sensor. Compared to the geometries and locations of the magnets used in the Type F and Type S packages, the geometry of this new self-biased sensor could reduce the total length of the package by up to 60%.

6.2. General Contributions to the Field of Knowledge

The general techniques mentioned above will potentially be applicable in other situations as well. For example, the package fabrication processes – such as the thermoforming of miniature LCP packages and 3D printing of polymeric packages – have the advantages of using materials with high ductility and machinability, and can be used to quickly iterate designs at a low cost. This makes them appropriate for many packaging applications that require electromagnetic transparency, high feature resolution, and good mechanical and chemical properties. Similarly, the multi-component assembly processes and assembly of polymeric packages to tubular structures can be extended to other stent projects. In addition, the Au-In eutectic bonding of multiple magnetoelastic layers and other materials can be combined with other micro-fabrication processes to achieve complex structures, stronger signal, and useful functionality. In relation to design methodologies, integrating DC bias magnets with magnetoelastic devices provides an approach to reduce the total size of each sensor node and make the resonators self-contained wireless devices. Finally, the approach for designing mass-loaded resonators to preserve low resonant frequencies as the resonator footprint is miniaturized expands the possibility for using magnetoelastic resonators in applications that are critically concerned with device size and high-frequency signal attenuation.

6.3. Future Work

6.3.1. Thermoformed Liquid Crystal Polymer Packages for Environmental Tagging System

Integration of a DC magnetic bias for a self-contained sensor node, scaling the process to allow batch fabrication, and developing and testing the antenna system for long-range interrogation are three possible thrusts for future work in this application. As noted in Chapter 2, the testing of the magnetoelastic tags which are packaged by LCP needed an external DC magnetic bias (provided by the Helmholtz coils in this case), and used a small transmit and receive coil set to trigger and sense the tags. This set-up is sufficient to prove the excellent material property of the package but the packaged resonators are not ready to be used in practical tagging applications. A complete sensor node for the magnetoelastic resonator requires a proper DC magnetic bias, which can be provided by integrating permanent magnets in the package (or as part of the resonator). The size of the magnets should be small compared to that of the package so that they can be inserted and sealed inside the package without major changes to the package volume. In the future, the molds that used to form LCP packages can be machined by batch-mode μEDM, resulting in a thermoforming process that, with some adjustments, can produce packages in batches. Another challenge for utilizing the packaged tags is the long-range interrogation system. The antenna system must be capable of transmitting with high power and receiving with high sensitivity in order to sense the tags over a long distance [Gia14].

6.3.2. 3D-Printed Packages for Plastic Biliary Stent Wireless Monitoring System

Chapter 3 described two types of 3D printed packages that were designed, fabricated, and tested. Although the benchtop test results proved the functionality of both packages regarded to the potential issues that might occur in and after the implantation procedure, the animal test results, which were described in Chapter 4, showed the limits of both designs. For the Type F package, the middle wires and the curved package due to the curved stent added additional stress on the sensor and thus reduced the sensor signal to be too small to detect. The Type S package was still longer, stiffer, and less elastic than desired.

Redesign of the package is desirable. Ideally, a shorter package (and shorter resonator) could be implemented, as this would reduce the overall impact of the package on the stent flexibility. Additionally, the package material should be elastic enough to let the stent pass through the tortuous endoscope channel and recover its initial shape. Furthermore, the package must provide enough stiffness so that the resonator is minimally curved by the natural anatomy of the bile duct.

Meeting all of these constraints may require the usage of multiple materials to form a hybrid package. For example, the mass-loaded self-biased resonator described in Chapter 5 could be used with a shorter version of the Type F package (with separate magnetic strips and the middle tether locations removed). An additional chrome-nickel Elgiloy foil layer (which has a high yield strain) for reinforcement could allow this design to meet all the constraints of elasticity, reduced length, and rigidity.

6.3.3. Magnetoelastic Resonator Miniaturization

In order to reduce the overall length of the package, the size of the sensor and the position of the magnets designed for the Type F package should be revised. Chapter 5 describes a new sensor structure that can significantly reduce the total length of the system but still maintain a low cross-section. The design should have some additional benefits. According to the analytical calculation and the simulation result, the quality factor of the sensor should increase because of the additional mass and the sensor energy should be much larger than that of the 6.25 mm long ribbon sensor (around 49% of the 12.5 mm long ribbon sensor, according to COMSOL simulation results). However, the quality factor of the mass-loaded sensor was similar to that of the ribbon sensor, and the measured signal energy was only 12% compared to that of the 12.5 mm long ribbon sensor. Therefore, these extra advantages were not reflected in the experimental evaluation of the prototype mass-loaded self-biased resonators. One possible reason is that in the analytical calculation, the mass loads are assumed to be point masses whereas in reality the mass loads occupy a large area. Another possible reason is that the bonding layer adds additional internal stress or damping and thus reduces the vibration amplitude of the sensor. More precise modeling and an improved bonding technique may unlock the potentially larger signal amplitude of this type of sensor architecture.

6.3.4. Au-In Eutectic Bonding Technique

The lamination of Metglas foil to Metglas foil by using the Au-In eutectic bonding technique is reported for the first time in this thesis, as described in detail in Appendix B. However, in the animal test that is recorded in Chapter 4, the two Metglas layers became delaminated due to the external force. This indicates that the bonding strength was not as high as expected. Also, as described in Appendix C, the bonded layer of the sensor became delaminated during the μEDM thinning process. Therefore, the fabrication process needs to be reviewed and refined. Some additional processes, such as oxygen plasma cleaning, may be required to enhance the adhesion between the deposited layers and the Metglas foil.

APPENDICES

Appendix A: Analytical Modeling of Mass-Loaded Sensor

Assume the longitudinal vibration of a thin uniform beam which has cross-sectional area *S*, material density ρ, and modulus *E* under an axial force *P*, as shown in Fig. A.1 (a),

$$\frac{\partial P}{\partial x} dx = \rho S dx \frac{\partial^2 u}{\partial t^2} \qquad \text{(A.1.1)}$$

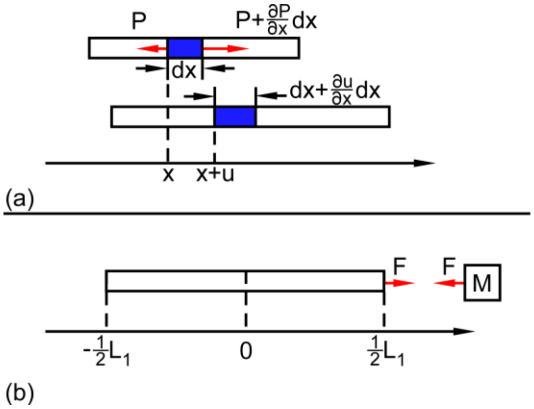

Fig. A.1: (a) Schematic of a longitudinal beam vibration. (b) Schematic of a mass loaded (M)/ mass loaded (M) beam.

The strain

$$\frac{\partial u}{\partial x} = \frac{P}{SE} \qquad \text{(A.1.2)}$$

so

$$\frac{\partial P}{\partial x} = SE\frac{\partial^2 u}{\partial x^2} \tag{A.1.3}$$

Thus, the wave equation is

$$\frac{\partial^2 u}{\partial t^2} = \frac{E}{\rho}\frac{\partial^2 u}{\partial x^2} \tag{A.1.4}$$

or

$$\frac{\partial^2 u}{\partial t^2} = \frac{1}{c^2}\frac{\partial^2 u}{\partial x^2} \tag{A.1.5}$$

where $c = \sqrt{}(E/\,\rho)$.

Assume $u(x,t) = F(x)G(t)$,

Hence

$$\frac{\partial^2 F(x)}{\partial x^2}G(t) = \frac{1}{c^2}\frac{\partial^2 G(t)}{\partial t^2}F(x)$$

$$\frac{1}{F(x)}\frac{\partial^2 F(x)}{\partial x^2} = \frac{1}{c^2}\frac{1}{G(t)}\frac{\partial^2 G(t)}{\partial t^2} \tag{A.1.6}$$

The LHS is a function of x only while the RHS is a function of t only and each side must be a constant, which is $-(\omega/c)^2$ in this case for easy calculation.

Then,

$$\frac{d^2 F(x)}{dx^2} + \left(\frac{\omega}{c}\right)^2 F(x) = 0 \tag{A.1.7}$$

and

$$\frac{d^2 G(t)}{dt^2} + \omega^2 G(t) = 0 \tag{A.1.8}$$

Therefore,

$$F(x) = A\sin\left(\frac{\omega}{c}\right)x + B\cos\left(\frac{\omega}{c}\right)x \quad \text{(A.1.9)}$$

$$G(t) = C\sin\omega t + D\cos\omega t \quad \text{(A.1.10)}$$

The complete solution to the wave equation is

$$u = (A\sin\left(\frac{\omega}{c}\right)x + B\cos\left(\frac{\omega}{c}\right)x)(C\sin\omega t + D\cos\omega t) \quad \text{(A.1.11)}$$

For a free-free beam, the strain $\partial u/\partial x = 0$ at $x = 0$ and $x = L_0$.

Therefore, ω can be calculated from A.1.11:

$$\omega_0 = \frac{\pi}{L_0}\sqrt{\frac{E}{\rho}}\ (rad/s) \quad \text{(A.2)}$$

For a point-mass-load (M)/point-mass-load (M) beam, as shown in Fig. A.1 (b),

$u = 0$ at $x = 0$ and $F = SE(\partial u/\partial x) = -M(\partial^2 u/\partial t^2)$ at $x = \pm\frac{1}{2}L_1$.

$$u = (A\sin\left(\frac{\omega}{c}\right)x + B\cos\left(\frac{\omega}{c}\right)x)(C\sin\omega t + D\cos\omega t) \quad \text{(A.3.1)}$$

At $x = 0$,

$$u = \left(A\sin\left(\frac{\omega}{c}\right)x + B\cos\left(\frac{\omega}{c}\right)x\right)(C\sin\omega t + D\cos\omega t) = 0 \quad \text{(A.3.2)}$$

So $B = 0$

A.3.1 becomes

$$u = (A\sin\left(\frac{\omega}{c}\right)x)(C\sin\omega t + D\cos\omega t) \tag{A.3.3}$$

At $x = \frac{1}{2}L_1$

$$F = SEA\frac{\omega}{c}\cos\left(\frac{\omega}{c}\right)\frac{1}{2}L_1 = MA\omega^2\sin\left(\frac{\omega}{c}\right)\frac{1}{2}L_1 \tag{A.3.4}$$

Thus,

$$\tan\left(\frac{\omega L_1}{2c}\right) = \frac{SE}{M\omega c}$$

$$\frac{\omega c}{E}\cdot\tan\left(\frac{\omega L_1}{2c}\right) = \frac{S}{M}$$

$$\omega L_1\sqrt{\frac{\rho}{E}}\cdot\tan\left(\frac{\omega L_1}{2}\sqrt{\frac{\rho}{E}}\right) = \frac{S\rho L_1}{M} \tag{A.3.5}$$

Appendix B: Au-In Eutectic Bonding

In this section, the gold-indium (Au-In) eutectic bonding process of the magnetoelastic foils are presented. The magnetoelastic material used in this work was the 28 μm thick iron-rich amorphous ferromagnetic alloy Metglas^{TM} 2826MB foil. Two pieces of the foil were bonded together by using the eutectic bonding process [Bha16, Akt13, Tan14b] in order to gain larger vibration amplitude and thus larger signal. Au-In eutectic bonding process involves the deposition of multiple layers of Au and In on the component metal surfaces. A low temperature bonding process is carried out between the two components up to 200°C. Above 157°C the indium layer melts and dissolves the gold layers to form a mixture of liquid and solid. The solid-liquid inter-diffusion process continues until the mixture solidifies to form the Au-In bond. This technique has established high bond strengths and is a relatively low temperature process having a high bond re-melting temperature (450°C).

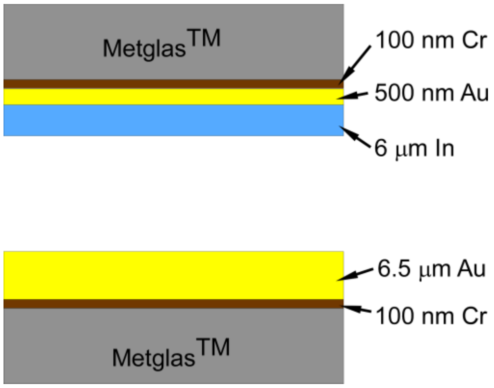

Fig. B. 1: Au-In eutectic bonding process of Metglas 2826MB foils.

The Metglas foils were first cleaned by the oxygen plasma and then used evaporation technique to deposit a 0.6 μm thick Cr/Au (100/500 nm) adhesion layer. After that, the two foils were electroplated 6 μm thick gold layer and In layer, respectively, as shown in Fig. B.1. The eutectic bonding process was performed in a vacuum oven at a temperature of 200°C for one hour with an applied pressure of 1.3 MPa. The bonding pressure was applied by using custom designed, spring-loaded C-clamps. Two 3” x 1” glass slides were used to uniformly distribute pressure along the area of the bonding materials (25 mm x 15 mm). A heating ramp rate of 5.87°C min^{-1} and a cooling rate of 0.37°C min^{-1} ensured adequate inter-diffusion and solidification of the mixture to form the Au–In bond.

Appendix C: Fabrication Result of Mass-Loaded Sensor with Thinned Down Couplers

C.1. Fabrication Process

The Metglas-Metglas bonded foil was sputtered Cr/Au (1 kA/5 kA) seed layer and then deposited 6 μm Au layer. The Arnokrome-Arnokrome bonded foil was also sputtered Cr/Au (1 kA/5 kA) seed layer and then deposited 6 μm In layer. The two foils were then bonded together in the oven.

C.2. Sensor with 0.75 mm x 0.5 mm x 30 μm Coupler

The bonded foil were then EDMed to fabricate the mass loaded sensor. The coupler was 0.75 mm long and 0.5 mm wide and thinned down to be 28 μm. Two samples were machined on the foil. However, during the releasing process, one mass load on the sample 1 and both mass loads on the sample 2 were delaminated. Two were conserved but one was missing. Only one part was still bonded firmly, as shown in Fig. C.1.

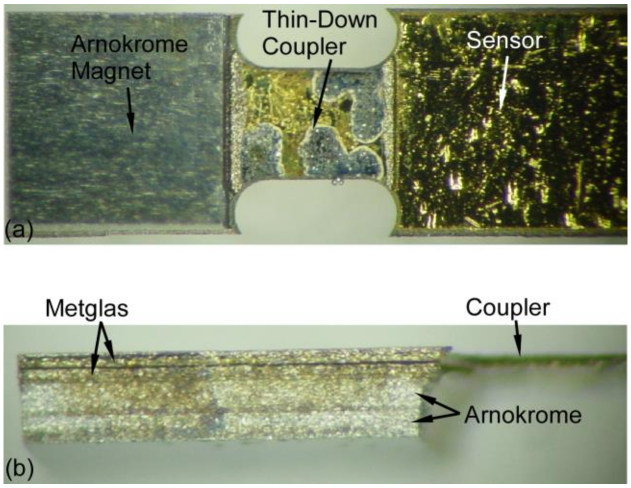

Fig. C.1: (a) Mass loading on the sensor sample 1. (b) Sideview of the two-layer Metglas bonded with the two-layer Arnokrome.

After inspecting under the microscope, the failure layer was found between Metglas and Metglas, as shown in Fig. C.2 and C.3. From Fig. C.2, some indium and gold spots were found not mixed while the other mixed part (silver) did not provide a strong bond. The mixed part close to the edge of the coupler has some cracks due to the EDM thinning process. From Fig. C.3, the Arnokrome-Arnokrom layer and the Arnokrome-Metglas layer were firmly bonded. Only one Metglas layer was found on the sensor part.

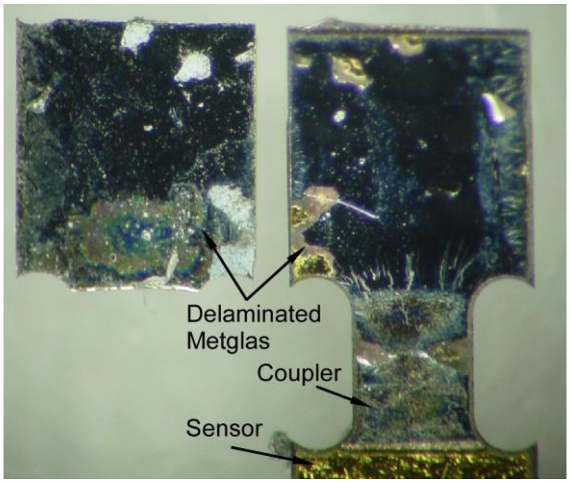

Fig. C.2: Metglas-Metglas bonding layer was delaminated during the EDM process.

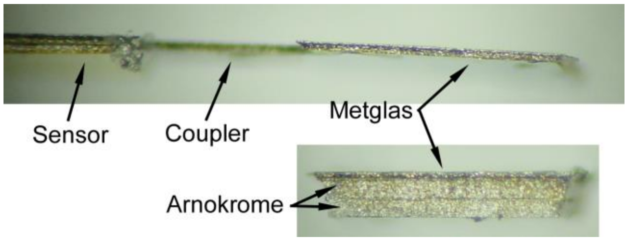

Fig. C.3: Sideview of the sensor and the mass loading.

For sample 2, both mass loads were delaminated during the releasing process, one mass load was saving while the other one was missing, as shown in Fig. C.4. The delaminated layer was also found at the Metglas-Metglas bonding layer. Later, the bonded sensor layer (in the middle) was also delaminated.

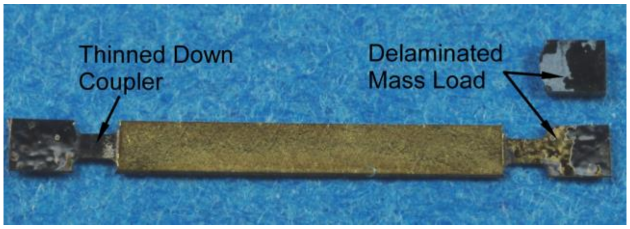

Fig. C.4: Figure of the sensor sample 2.

REFERENCES

[Akt13] E. Aktakka, R. Peterson, and K. Najafi, “Wafer-Level Integration of High-Quality Bulk Piezoelectric Ceramics on Silicon”, *IEEE Transactions on Electron Devices*, vol. 60, no. 6, pp. 2022-2030, Jun. 2013.

[An14] S. An, N. Gupta and Y. Gianchandani, “Vacuum Sealing Using Atomic Layer Deposition of Al2O3 at 250°C,” Journal of Vacuum Science and Technology A: Vacuum, Surfaces and Films, vol. 32, no. 1, Jan. 2014.

[Arn11] Arnold Magnetic Technologies, “Arnokrome 5 Specification”, datasheet, Rev. 2/24/11.

[Awa10a] F. Awaja, S. Zhang, N. James, and D. McKenzie, “Plasma Activation and Self Bonding of PEEK for the Use in the Encapsulation of Medical Implants,” *Plasma Processes and Polymers,* vol. 7, no. 9-10, pp. 866-875, Oct. 2010.

[Awa10b] F. Awaja, S. Zhang, N. James, and D. R. McKenzie, “Enhanced Autohesive Bonding of Polyetheretherketone (PEEK) for Biomedical Applications Using a Methane/Oxygen Plasma Treatment,” *Plasma Processes and Polymers,* vol. 7, no. 12, pp. 1010-1021, Dec. 2010.

[Bao87] X. Bao, W. Burkhard, V. Varadan, and V. Varadan, “SAW temperature sensor and remote reading system”, *IEEE Ultrasonics Symposium*, 1987.

[Bha16] N. Bhattacharjee, A. Urrios, S. Kanga and A. Folch, “The upcoming 3D-printing revolution in microfluidics”, *Lab on a Chip*, vol. 16, pp. 1720-1742, 2016.

[Chi10] T. Chin, P. Zheng, I. Oppenheim, and D. Greve, “Surface Acoustic Wave Devices for Wireless Strain Measurement”, *Proc. SPIE 7647, Sensors and Smart Structures Technologies for Civil, Mechanical, and Aerospace Systems*, vol. 7647, no. 43, 2010.

[Com96] J. Comyn, L. Mascia, G. Xiao, and B. Parker, “Plasma-treatment of polyetheretherketone (PEEK) for adhesive bonding,” *International Journal of Adhesion and Adhesives,* vol. 16, no. 2, pp. 97-104, May 1996.

[Dok99] M. Dokmeci and K. Najafi, “A High-Sensitivity Polyimide Humidity Sensor for Monitoring Hermetic Micropackages,” *Micro Electro Mechanical Systems*, EMS'99, pp. 279-284, Jan. 1999.

[Don07] G. Donelli, E. Guaglianone, R. Di Rosa, F. Fiocca, and A. Basoli, “Plastic Biliary Stent Occlusion: Factors Involved and Possible Preventive Approaches”, *Clinical Medicine & Research*, vol. 5, no. 1, pp. 53-60, Mar. 2007.

[Don10] G. Donelli, E. Guaglianone, R. Rosa, F. Fiocca, and A. Basoli, “Plastic Biliary Stent Occlusion: Factors Involved and Possible Preventive Approaches”, *Clinical Medicine & Research*, vol. 5, no. 1, pp. 53-60, 2007.

[Eng00] G. Engdahl, “Handbook of Giant Magnetostrictive Materials”, *Academic Press*, pp. 1-19, 2000.

[Fai00] D. Faigel, “Preventing biliary stent occlusion”, *American Society for Gastrointestinal Endoscopy*, vol. 51, no. 1, 2000.

[Gha13] M. Ghaed, G. Chen, R. Haque, M. Wieckowski, Y. Kim, G. Kim, Y. Lee, I. Lee, D. Fick, D. Kim, M. Seok, K. Wise, D. Blaauw, and D. Sylvester, “Circuits for a Cubic-Millimeter Energy-Autonomous Wireless Intraocular Pressure Monitor”, *IEEE Transactions on Circuits and Systems*, vol. 60, no. 12, pp. 3152-3162, Dec. 2013.

[Gia14] Y.B. Gianchandani, S.R. Green, K. Sarabandi, M. Kanj, H. Schmidt, J. Tang, J. Wu, “Interrogating Subterranean Hydraulic Fractures using Magnetoelastic Resonators,” US patent 61931934.

[Gia15] Y. Gianchandani, S. Green, K. Sarabandi, M. Kanj, H. Schmidt, J. Tang, and J. Wu, “Interrogating subterranean hydraulic fractures using magnetoelastic resonators”, US patent, WO 2015112996 A1, Jul. 2015.

[Gre07] S. Green, M. Richardson, F. Shariff, and Y. Gianchandani, “Photochemically patterned biliary stents with integrated permanent magnets and deformable assembly features for wireless magnetoelastic tissue growth sensing”, *TRANSDUCERS 2007: Solid-State Sensors, Actuators and Microsystems Conference*, 2007.

[Gre09a] S. Green, “Wireless Magnetoelastic Monitoring of Biliary Stents”, Doctoral dissertation, University of Michigan, 2009.

[Gre09b] S. Green and Y. Gianchandani, "Wireless magnetoelastic monitoring of biliary stents", *Journal of Microelectromechanical Systems*, vol. 18, no. 1, pp. 64-78, Feb. 2009.

[Gre09c] S. Green and Y. Gianchandani, "A Batch-Patterned Self-Expanding Biliary Stent with Conformal Magnetic PDMS Layer and Topologically-Matched Wireless Magnetoelastic Sensor", *2009 IEEE 22nd International Conference on Micro Electro Mechanical Systems*, DOI: 10.1109/MEMSYS.2009.4805356, Mar. 2009.

[Gre13] S. Green, R. Kwon, G. Elta, and Y. Gianchandani, "*In vivo* and *in situ* evaluation of a wireless magnetoelastic sensor array for plastic biliary stent monitoring", *Biomedical Microdevices*, vol. 15, no. 3, pp. 509-517, Jun. 2013.

[Gri02] C. Grimes, C. Mungle, K. Zeng, M. Jain, W. Dreschel, M. Paulose, and K. Ong, "Wireless Magnetoelastic Resonance Sensors: A Critical Review", *Sensors*, vol. 2, pp. 294-313, 2002.

[Gri11] C. Grimes, S. Roy, S. Rani, and Q. Cai, "Theory, Instrumentation and Applications of Magnetoelastic Resonance Sensors: A Review", *Sensors*, vol. 11, pp. 2809-2844, 2011.

[Hal12] L. Hallmann, A. Mehl, N. Sereno, and C. Hämmerle, "The improvement of adhesive properties of PEEK through different pre-treatments," *Applied Surface Science,* vol. 258, no. 18, pp. 7213–7218, Jul. 2012.

[Hua16] Q. Huang, L. Dong, and L. Wang, "LC Passive Wireless Sensors Toward a Wireless Sensing Platform: Status, Prospects, and Challenges", Journal of Microelectromechanical Systems, vol. 25, no. 5, pp. 822-841, Oct. 2016.

[IEE91] Institute of Electrical and Electronics Engineers, "IEEE Standard on Magnetostrictive Materials: Piezomagnetic Nomenclature," 1991.

[Iqb14] H. Iqbal, S. Bhowmik, and R. Benedictus, "Process optimization of solvent based polybenzimidazole adhesive for aerospace applications," *International Journal of Adhesion and Adhesives,* vol. 48, pp. 188-193, Jan. 2014.

[Jay98] K. Jayaraj and B. Farrell, "Liquid Crystal Polymers and their role in Electronic Packaging," *Advancing Microelectronics*, vol. 25, no. 4, pp.15-18, Jul. 1998.

[Joy07] J. Joy, J. Kroh, M. Ellis, M. Allen, and W. Pyle, "Communicating with implanted wireless sensor", U.S. Patent 7245117 B1, Jul. 2007.

[Jud07] J. Judah and P. Draganov, “Endoscopic therapy of benign biliary strictures”, *World J Gastroenterol*, vol. 13, no. 26, pp. 3531-3539, Jul. 2007.

[Kad92] S. Kadakia, E. Starnes, “Comparison of 10 french gauge stent with 11.5 french gauge stent in patients with biliary tract diseases”, *Gastrointest Endosc.*, vol. 38, pp. 454-459, 1992.

[Kwo16] C. Kwon, M. Gromski, S. Sherman, J. Easler, I. Hajj, J. Watkins, E. Fogel, L. McHenry, and G. Lehman, “Time Sequence Evaluation of Biliary Stent Occlusion by Dissection Analysis of Retrieved Stents”, *Digestive Diseases and Sciences*, vol. 61, pp. 2426–2435, May. 2016.

[Lib96] E. Libby and J. Leung, “Prevention of Biliary Stent Clogging: A Clinical Review”, *Am. J. Gastroenterol*, vol. 91, no. 7, pp. 1301-1307, Jul. 1996.

[Mon88] S. Montean, RF reactivatable marker for electronic article surveillance system US Patent Specification 4745401, 1988.

[Mon90] S. Montean and Blaine, Multi-directionally responsive dual-status, magnetic article surveillance marker having continuous keeper US Patent Specification 4967185, 1990.

[Pep14] V. Pepakayala, S. Green, and Y. Gianchandani, “Passive Wireless Strain Sensors Using Microfabricated Magnetoelastic Beam Elements”, *JMEMS*, 2014.

[Pep15] V. Pepakayala, “Micromachined Magnetoelastic Sensors and Actuators for Biomedical Devices and Other Applications”, Doctoral dissertation, University of Michigan, 2015.

[Pio92] C. Piotrowski, C. Bruzzone, and J. Mcallister, Multi-layer thin-film EAS marker US Patent Specification 5083112, 1992.

[Pro17a] “ProJet 3500 SD & HD”, datasheet, http://www.3dsystems.com/sites/www.3dsystems.com/ files/projet 3500 plastic usen.pdf, 2017.

[Pro17b] ProJet 3500 HD Max 3D Systems, http://www.aniwaa.com/product/3d-printers/3d-systems-projet-3500-hd-max/, 2017

[Qu15] J. Qu, J. Tang, Y. Gianchandani, K. Oldham, and S. Green, “Dynamic modeling of a bidirectional magnetoelastic rotary micro-motor”, *Sensors and Actuators A: Physical*, vol. 223, pp. 49-60, 2015.

[Rai03] I. Raijiman, “Biliary and pancreatic stents”, *Gastrointest Endoscopy Clinics of North*

America, vol. 13, pp. 561-592, 2003.

[Ric10] M. Richardson and Y. Gianchandani, “Wireless Monitoring of Workpiece Material Transitions and Debris Accumulation in Micro-Electro-Discharge Machining,” *J. Microelectromech. Syst*, vol. 19, no. 1, pp. 48-54, Feb. 2010.

[Shi16] Y. Shi, M. Choi, Z. Li, G. Kim, Z. Foo, H. Kim, D. Wentzloff, and D. Blaauw, “A 10mm^3 Syringe-Implantable Near-Field Radio System on Glass Substrate”. *2016 IEEE International Solid-State Circuits Conference*, Feb. 2016.

[Soc16] R. Sochol, E. Sweet, C. Glick, S. Venkatesh, A. Avetisyan, K. Ekman, A. Raulinaitis, A. Tsai, A. Wienkers, K. Korner, K. Hanson, A. Long, B. Hightower, G. Slatton, D. Burnett, T. Massey, K. Iwai, L. Lee, K. Pisterbi and L. Lin, “3D printed microfl uidic circuitry via multijet-based additive manufacturing”, *Lab on a Chip*, vol. 16, pp. 668-678, 2016.

[Sty14] Stycast2850FT datasheet, Henkel Loctite, Jan. 2014.

[Tak02] K. Takahata and Y. Gianchandani, “Batch Mode Micro-Electro-Discharge Machining,” *J. Microelectromech. Syst*, vol. 11, no. 2, pp. 102-110, Apr. 2002.

[Tak03] K. Takahata, A. DeHennis, K. Wise, and Y. Gianchandani, “Stentenna: a micromachined antenna stent from wireless monitoring of implantable microsensors”, *25th Annual lntemational Conference of the IEEE EMBS*, Cancun, Mexico, Sep. 2003.

[Tak06] K. Takahata, Y. Gianchandani, and K. Wise, “Micromachined Antenna Stents and Cuffs for Monitoring Intraluminal Pressure and Flow”, *JMEMS*, vol. 15, no. 5, pp. 1289-1298, Oct. 2006.

[Tan13] J. Tang, S. Green, and Y. Gianchandani, “Miniature Wireless Magnetoelastic Resonant Motor With Frequency Selectable Bidirectional Rotation” Journal of Microelectromechanical Systems, vol. 22, no. 3, pp. 730-738, Jun. 2013.

[Tan14a] J. Tang, S. Green, and Y. B. Gianchandani, “Scalable, High-Performance Magnetoelastic Tags Using Frame-Suspended Hexagonal Resonators,” *Journal of Micromechanics and Microengineering*, vol. 24, paper 065006, Mar. 2014.

[Tan14b]J. Tang, “Wireless Tagging and Actuation with Shaped Magnetoelastic Transducers”, Doctoral dissertation, University of Michigan, 2014.

[Ten04] M. Tentzeris, J. Laskar, J. Papapolymerou, S. Pinel, V. Palazzari, R. Li, G. DeJean, N. Papageorgiou, D. Thompson, R. Bairavasubramanian, S. Sarkar, and J. Lee, "3-D-Integrated RF and Millimeter-Wave Functions and Modules Using Liquid Crystal Polymer (LCP) System-on-Package Technology," *Transactions on Advanced Packaging*, vol. 27, no. 2, pp. 332-340, May 2004.

[Tho14] D. Thompson, O. Tantot, H. Jallageas, G. Ponchak, M. Tentzeris, and J. Papapolymerou, "Characterization of Liquid Crystal Polymer (LCP) Material and Transmission Lines on LCP Substrates from 30-110 GHz," *IEEE Transactions on Microwave Theory and Techniques,* vol. 52, no. 4, pp. 1343-1352, Apr. 2014.

[Tse06] F. Tse, J. Barkun, J. Romagnuolo, G. Friedman, J. Bornstein, and A. Barkun, "Nonoperative imaging techniques in suspected biliary tract obstruction", *HPB (Oxford)*, vol. 8, no. 6, pp. 409-425, 2006.

[Vec01] Vectra and Vectran liquid crystal polymer, Ticona, 2001.

[Vec11] VECTRA-E150i datasheet, Celanese, Nov. 2011.

[Vis13] A. Viswanath, S. Green, J. Kosel, and Y. Gianchandani, "Metglas–Elgiloy bi-layer, stent cell resonators for wireless monitoring of viscosity and mass loading", Journal of Micromechanics and Microengineering, vol. 23(2), no. 025010, Feb. 2013.

[Vis14] A. Viswanath, "Precision and Scalability in Ultrasonic Machining for Microscale Features", Doctoral dissertation, University of Michigan, 2014.

[Wag13] M. Wagh, M. Bellis, E. Fogel, J. Frakes, J. Johanson, T. Qaseem, D. Howell, G. Lehman, and S. Sherman, "Multicenter randomized trial of 10-french versus 11.5-french plastic stents for malignant biliary obstruction", Diagnostic and Therapeutic Endoscopy, vol. 2013, pp. 891-915, 2013.

[Wah16] S. Waheed, J. Cabot, N. Macdonald, T. Lewis, R. Guijt, B. Paullab and M. Breadmore, "3D printed microfluidic devices: enablers and barriers", *Lab on a Chip*, vol. 16, pp. 1993 – 2013, 2016.

[Wan01] X. Wang, L.-H. Lu, and C. Liu, "Micromachining Techniques for Liquid Crystal Polymer," *the 14th IEEE International Conference on Micro Electro Mechanical Systems*, Interlaken, Swissland, 2001.

[Wan03] X. Wang, J. Engel, and C. Liu, “Liquid Crystal Polymer (LCP) for MEMS: Processes and Applications,” *J. Micromech. Microeng.*, vol. 13, no. 5, pp. 628–633, Sep. 2003.

[Wei05] R. Weinstein, “RFID: A Technical Overview and Its Application to the Enterprise”, *IEEE Computer Society, IT Pro*, vol. 7, no. 3, pp. 27-33, May. 2005.

[Yu14] L. Yu, B. Kim, and E. Meng, “Chronically Implanted Pressure Sensors: Challenges and State of the Field”, *Sensors*, vol. 14, pp. 20620-20644, 2014.

[Zou02] G. Zou, H. Grönqvist, P. Starski, and J. Liu, “High-frequency characteristics of liquid crystal polymer for system in a package application,” *the 8th International Symposium on Advanced Packaging Materials,* Stone Mountain, GA, US, 2002.